INVESTIGATION OF SINE-WAVE INPUTS FOR AN FDM EIT SYSTEM

PREPARED BY: A. Giannopoulos, post-graduate student
in the Department of Electrical Engineering
at the University of Cape Town

PREPARED FOR: The Department of Electrical Engineering
at the University of Cape Town

March 2003

Thesis submitted in fulfilment of the requirements
of the degree of Masters (MSc) in Electrical Engineering
at the University of Cape Town

ACKNOWLEDGMENTS

I would like to express my gratitude and appreciation to all of those who have contributed, either directly or indirectly to this thesis project.

Thanks to Prof. J. Tapson and Mr. G. Teague.

Special thanks to my family and friends for their continuous support.

TERMS OF REFERENCE

This thesis project report describes the research done by the author under the supervision of Prof. J. Tapson. The area of research is an investigation of sine-wave drive for a frequency division multiplexing (FDM) electrical impedance tomography (EIT) system. This thesis was commissioned by Prof. J. Tapson, on the 1st of November 2001.

The goals were as follows:

1. Investigate the research done on this project by previous researchers.
2. Investigate the current applications in which capacitance, resistance and impedance tomography are used in research level and in industry.
3. Design and develop a working 8-electrode impedance tomography system. Also, make provisions for a possible upgrade of the 8-electrode system to a 16-electrode (16 capacitance and 16 resistance electrodes) system employing FDM and using sine-wave excitation.
4. Verify and compare the performance of the 8-electode impedance tomography system to the previous research done by Teague [53], for static configurations of multi-phase air-gravel-seawater mixtures.
5. Evaluate the ability of the system to differentiate between air and gravel mass in static situations.
6. Draw conclusions regarding the performance, effectiveness and limitations of the system.
7. Make recommendations for future project developments.
8. Submit the thesis by the 28th of March 2003.

SYNOPSIS

This research thesis describes the development of a frequency division multiplexed (FDM) impedance tomography system employing sine-wave excitation. It investigates the use of an 8-electrode (8 capacitance plates and 8 resistance probes) impedance tomography system, for multi-phase (air-gravel-seawater) cross-sectional image reconstruction, as well as calculating the individual volume fraction predictions of the air, gravel and seawater that are placed in the measurement volume of the vessel (rig) under investigation. This project acts as a stepping stone for the development of a multi-phase flow-meter for the on-line monitoring of an airlift used in an offshore mining application.

The main objective of this project was to determine whether or not a frequency division multiplexed (FDM) impedance tomography system using sine-wave excitation could provide an improved system, capable of obtaining more accurate results than the 8-electrode impedance tomography system designed by Teague [53] that used FDM with square-wave excitation. The outcomes of the research were evaluated with the use of a software program employing a multi-layer perceptron neural network using various neural network structures and training configurations. The final objective was to examine the results collected over the period of testing (static tests were the only tests performed by the author) and compare them to the ones obtained by the impedance tomography system using square-wave excitation, whenever information was available.

The project starts by introducing the reader to a summary of information relevant to the different time division multiplexing (TDM) techniques that have been used by various tomography systems, as well as to the concept of frequency division multiplexing (FDM) employed in this system. An introduction to the architecture of the multi-layer perceptron, used by the software program employed by the author follows. The project then continues by taking the reader through an in depth analysis of each module used in the development of the FDM impedance tomography system employing sine-wave excitation. After that the author describes to the reader how the training and testing datasets were obtained under static tests, and how the system under investigation responded to the disturbance of its

electric field, caused by the insertion of the different size and material tubes and bubbles simulating air and gravel in the contained of the vessel (seawater). Finally, the performance and results of the different tests that were conducted on the final design were analysed by using the multi-layer perceptron neural network to predict the individual volume fractions of air-gravel-water mixtures with or without performing cross-sectional image reconstruction of the vessel.

This research is based on design parameters that were used by previous researchers working on this project over the years. Some of these parameters were not optimally designed at the time. Although the author acknowledges the existence of such errors and recommendations are presented to the reader throughout the thesis, concentrating on improving the system rather than redesigning it was of utmost importance. As a result, the performance, accuracy and stability of the FDM impedance tomography system were altered by the presence of these errors. Such errors were introduced by the frequency generation modules of the system, as well as the two-electrode method employed by the EIT system to collect the resistance readings.

Even with the above-mentioned weaknesses of the system, the readings were repeatable. Results showed that the multi-layer perceptron neural network was able to generalize for previously unseen combinations of the three phases, as well as for previously unseen air-bubbles. In general the FDM impedance tomography system employing sine-wave excitation outperformed the system employing different frequency square-waves, for both threshold error and volume fraction prediction errors and with and with out image reconstruction. Also, better sum-of-volume-fraction prediction results were obtained when image reconstruction was not performed.

As a result of this project the following recommendations were made. A new data collection protocol using frequency division multiplexing (FDM) and preferably employing a four-electrode adjacent pair measurement technique should be examined theoretically and practically. A new method of generating the sine-wave frequencies injected into the measurement volume should also be investigated. Finally, since

provisions were made by the author so that the sensing electronics and data acquisition system could be used for a system using more that 8-electrodes, a EIT system using frequency division multiplexing, injecting sine-waves in the rig and featuring a higher number of sensing electrodes should be used for future developments. Following that, dynamic flow situations, on-line real-time data capture, as well as individual component velocities could be addressed in future development of the project.

TABLE OF CONTENTS

LIST OF ILLUSTRATIONS

Page

FIGURES

TABLES

CHAPTER 1

1. INTRODUCTION

Electrical impedance (capacitance and resistance) tomography is used in industrial applications to perform detailed monitoring of processes and therefore allow more complex control of process equipment [6]. An advantage of this approach is that the system is non-intrusive and therefore does not affect the mixture or the flow being monitored in the vessel. Also by implementing neural networks for obtaining cross-sectional image reconstructions and volume fraction predictions, no flow pre-processing is required and the measurements are flow regime independent [53].

In general, the measuring principle used in electrical capacitance tomography is that the capacitance measured between two electrodes is a function of the permittivity of the component or components in the measurement volume, as well as of the distribution of these components. By mounting an array of electrodes peripherally and equidistantly around the measurement volume, it is possible to obtain sets of linearly independent measurements of this capacitance by making use of permutations of combinations. In the recent years, many areas of research for the application of capacitance tomography have come to light. Much of this research has been devoted to the imaging of non-conductive phases in vessels or pipelines [6, 7, 32].

The measurement principle used in electrical resistance tomography is based on the fact that the resistance measured between two electrodes is a function of the resistivity of the components across the plane of interest, as well as their distribution. By employing an array of equally spaced electrodes mounted into the periphery of the measurement volume, it is possible to obtain sets of linearly independent measurements of this resistivity. Measurements of electrical resistivity via four electrodes are widely used in a variety of applications, mainly dealing with the imaging of conductive phase [33].

1.1 Background to the Investigation

This project has progressed through a number of researchers and stages at the University of Cape Town (U.C.T) in the last few years. Firstly, research was done by Smit [1, 2] whose task was to determine whether capacitance tomography was capable of imaging an air-gravel-seawater mixture. Secondly, research was done by Teague [3, 4] whose task was to determine whether neural networks could provide an improved and more accurate way of imaging and monitoring air-gravel-seawater mixtures.

Research was continued by the latter researcher [53] and a dual 16-electrode (16 capacitance plates and 16 resistance probes) impedance tomography system, employing frequency division multiplexing (FDM) and using square-wave excitation was developed for calculating the mass flow rate of an air-gravel-seawater mixture.

1.2 Purpose of this Thesis

This thesis investigates the use of an 8-electrode (8 capacitance plates and 8 resistance probes) impedance tomography system, employing frequency division multiplexing (FDM) and using sine-wave excitation, for multi-phase (air-gravel-seawater) cross-sectional imaging, as well as calculating the individual volume fraction predictions of the air, gravel and seawater that are placed in the measurement volume of the vessel (rig) under investigation.

This thesis serves as a stepping stone for the hardware development e.g. primary sensor system (electrodes), the sensor electronics (capacitance and resistance measurement modules), as well as the data acquisition system (DAS) that could be used if a dual-plane impedance tomography system, employing FDM and using sine-wave excitation to calculate the mass flow rate of an air-gravel-seawater mixture were to be developed. In this way the long-term goal of this project, the development of a system that monitors a multi-phase airlift used in offshore mining applications could be achieved.

This project relies heavily on the designing of the sensor electronics (capacitance and resistance measurement modules), as well as the improvement of the primary sensor system, to maximise the accuracy and performance of an 8-electrode system, with the possibility for upgrading it to a 16-electrode system. The main goal is to investigate the use of FDM employing sine-wave excitation for impedance tomography, by performing static tests employing air and/or gravel and seawater mixtures and comparing the results using FDM sine-wave excitation and FDM square-wave excitation.

However, in order for valid comparison between work done by the previous researcher to be achieved, the same software and data collection techniques that was employed and designed by Teague [53] for the neural network training and testing were used by the author.

1.3 Objectives of this Research

The objectives of this research, as specified by Prof. J. Tapson in connection with the development of a working 8-electrode impedance tomography rig were to:

- Investigate the research done on this project by previous researchers.
- Investigate the current applications in which capacitance, resistance and impedance tomography are used in research and in industry, and also to investigate the primary sensor systems, sensor electronics and data acquisition systems (DAS) adopted by them.
- Develop working prototypes of the different hardware modules that will be used in an 8-electrode (8 capacitance and 8 resistance electrodes) impedance tomography system employing FDM and using sine-wave excitation, and make provisions for a possible upgrade of the 8-electrode system to a 16-electrode (16 capacitance and 16 resistance electrodes) system employing FDM and using sine-wave excitation.
- Design and develop a working 8-electrode impedance tomography system.
- Verify and compare the performance of the 8-electode impedance tomography system to the previous research done by Teague [53], for static configurations of multi-phase air-gravel-seawater mixtures.

- Evaluate the ability of the system to differentiate between air and gravel mass in static situations.
- Draw conclusions regarding the performance, effectiveness and limitations of the system.
- Make recommendations for future project developments.

This project will only consider the development of a laboratory-based piece of equipment. Further work would therefore have to be done to convert this equipment into an instrument suitable for industry.

1.4 Layout of the Thesis

The contents of this thesis are organized into different chapters. A summary of each chapter is given below:

Chapter 1 is an introductory chapter. Its main function is to introduce the reader to the principles behind the project. This chapter gives the background to the investigation, the purpose and the objectives of this research, as well as the layout of this thesis.

Chapter 2 is a literature review. A summary of information relevant to the different time division multiplexing (TDM) techniques that have been used to sense and measure capacitance and/or resistance in various tomography systems, as well as to the concept of frequency division multiplexing (FDM) employed in this system, are contained in this chapter.

Chapter 3 was designed with the intention to provide the reader with a general understanding of what a neural network is, as well as an introduction to the architecture of the multi-layer perceptron, used by the software program employed by the author.

Chapter 4 elaborates on the different modules that were put together to form a unit that measures capacitance and resistance.

Chapter 5 describes to the reader how the training and testing data sets were obtained under static tests, as well as the technique used to vary the dielectric distribution within the area of interest (rig).

Chapter 6 details how the electric impedance tomography (EIT) system under investigation responded to the disturbances of the electric field (formed by the system in the testing vessel) caused by the insertion of the different size and material bubbles simulating air and gravel in the medium contained in the vessel (seawater).

Chapter 7 deals with the performance and the results of the different tests that were conducted on the final design, by using the multi-layer perceptron neural network to predict the individual volume fractions of air-gravel-water mixtures, with or without performing cross-sectional image reconstruction of the vessel.

Chapter 8 gives a list of conclusions drawn from the results of the investigation and experiments conducted.

Chapter 9 makes recommendations with the objective of further improving the system.

Appendix A contains the microprocessor assembly codes used for the generation of the different sine-wave and their quadrature frequencies needed by the project.

Appendix B deals with the modified section of the PBIL code used by the author in order to obtain the right sine-wave frequencies.

Appendix C contains the complete circuit diagrams of the impedance tomography system designed by the author.

CHAPTER 2

2. LITERATURE REVIEW

This section elaborates on the different time division multiplexing (TDM) techniques that have been used to sense and measure capacitance and/or resistance in various tomography systems.

Special interest is then given to explaining the concept of frequency division multiplexing (FDM), which was employed in this project.

2.1 Time Division Multiplexed Impedance Tomography

Time division multiplexing (TDM) is the method adopted by most standard tomography systems. These systems utilize the switching of different electrode combinations, so that capacitance (Electrical Capacitance Tomography (ECT)) and resistance (Electrical Resistance Tomography (ERT)) readings can be measured serially. However the frames per second rate that can be achieved with this technique is limited by the fact that the overall time dedicated to the measurement process is increased due to the switching that takes place between the electrodes [5].

2.1.1 Electrical Capacitance Tomography

In general, the measuring principle used in electrical capacitance tomography is that the capacitance measured between two electrodes is a function of the permittivity of the component or components in the measurement volume, as well as of the distribution of these components. Therefore, by mounting an array of electrodes peripherally and equidistantly around the measurement volume, sets of linearly independent measurements are possible by making use of permutations of combinations. These sets of linearly independent measurements can produce a sequence of images (with the help of a reconstruction algorithm) depicting the dielectric distribution across the plane of interest as

a function of time. It is also possible that quantitative information could be extracted by investigating a number of these computed images.

A significant difference between different tomographic techniques is the linearity of integration, since in a tomography system the actual measurement values obtained are of integral nature [6]. In linear tomography the path (or area) of integration is known, but in non-linear tomography they are not [6].

A capacitance tomography system can be divided into the following three sections:

- The primary sensor system (electrodes)
- The sensor electronics and capacitance measurement instruments (data acquisition system (DAS))
- A fast computer for the image reconstruction, or any other prediction that is required for the specific system, e.g. volumetric fraction predictions or velocity calculation for the phase or phases [7, 8, 9, 10 and 11] under investigation.

A schematic representation of the measurement chain for electrical capacitance tomography is shown in figure 2.1.

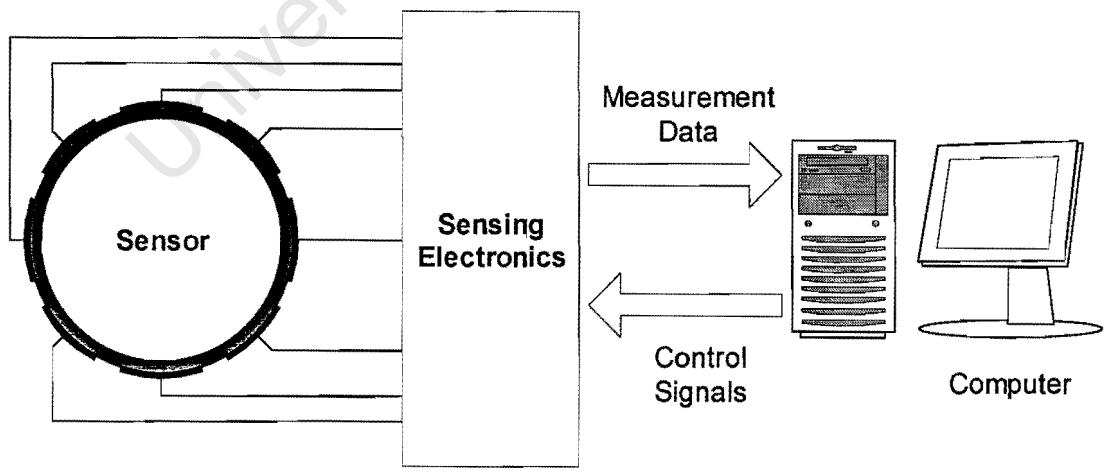

Figure 2.1: Block diagram of an ECT system with eight sensing electrodes.

2.1.1.1 Sensors

As has already been mentioned, the primary sensor system is generally represented by an array of electrodes mounted peripherally and equidistantly around the plane or planes of interest, giving it mechanical stability. The electrodes tend to be of low cost, easy to fabricate and install, and are usually manufactured from copper foil, brass, and galvanized iron or stainless steel plates [12].

The number of electrodes, which are mounted around the measurement volume, varies considerably among different tomography systems, due to the different applications that those systems are used for. Waterfall et al [13] used a six-electrode sensor system, Isaksen [14] and Xie et al [15] used eight-electrode systems, and Yang et al [16, 17, and 18] used twelve-electrode systems. Other systems were designed for sixteen-electrodes (Reinecke and Mewes [19]) and others used thirty-two-electrodes (Reinecke and Mewes [6]).

The main reason behind the trend of increasing the number of electrodes is due to the more favourable higher resolution graphical representation of the cross-sectional dielectric distribution of the measurement volume that can be attained. The drawback, however, is that more sophisticated capacitance sensing hardware must be employed due to the small levels of capacitance that will have to be detected between and around the sensing region [20].

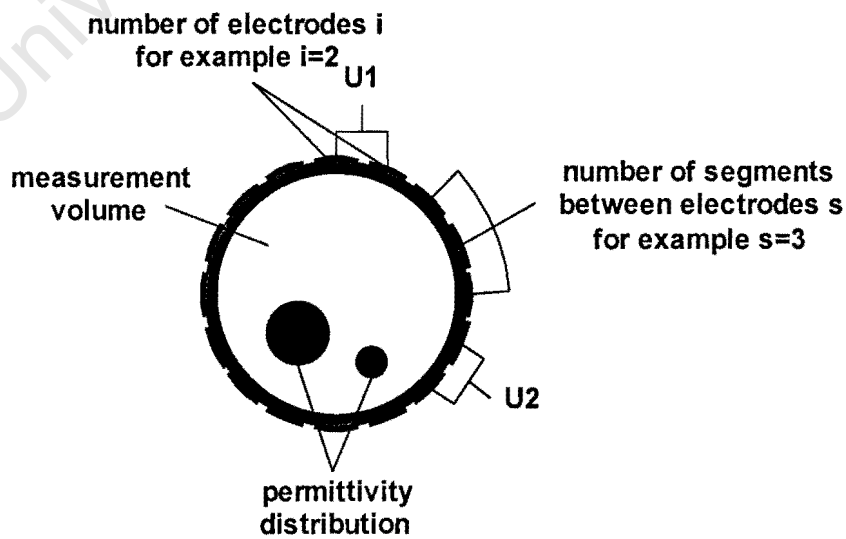

Figure 2.2: A 16-electrode sensor operated in a two-segment mode.

Also, with the electrodes being closer to each other, unfavourable edge effects will be more pronounced [21]. This disadvantage could be overcome by using more that one segment as one electrode, as proposed by Reinecke and Mewes [19]. This could be achieved, for example, by using a sixteen-electrode sensor in a two-segment mode configuration (see figure 2.2 on the previous page) instead of an eight-electrode sensor in a one-segment configuration.

Even though the total area covered by both systems is equal [6], the total number of linearly independent measurements obtained by sixteen-electrode sensor operating in a two-segment mode ($\frac{n}{2}(n-3)=104$, where n is the number of electrodes) is almost four times higher than that obtained by the eight-electrode sensor operating in one-segment mode ($\frac{n}{2}(n-1)=28$).

In order to avoid outside electromagnetic interference with the capacitance measurements, an earthed radial shield should be used to guard the measurement electrodes [22]. Also, even though added constructional effort will be required, the earthed radial shield should have radial extensions attached such a way that when the radial shield is placed around the rig (vessel), they will be positioned between the electrodes. Both the earthed radial shield and its radial extensions are illustrated in figure 2.3.

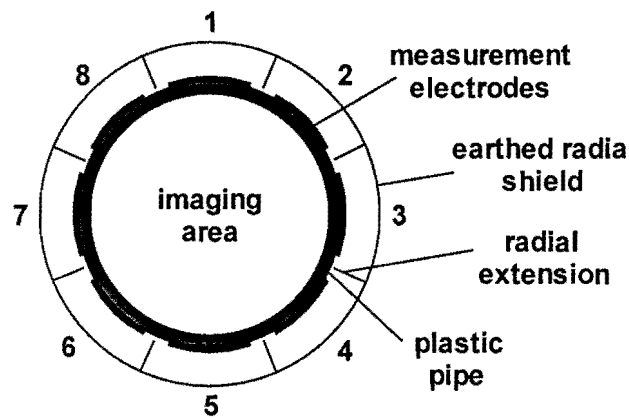

Figure 2.3: Cross-sectional view of an 8-electrode capacitive primary sensor.

This configuration ensures a more effective isolation of the electrodes when they are used in a one-segment mode, by ensuring that the electric field has to pass through the vessel and cannot simply pass around the outside of the vessel [6].

The shielding of the sensor in the axial direction is also of crucial importance. This shield can have the form of two plates segmented in a fashion analogous to the measurement electrodes, and positioned above and below the sensing electrodes. The axial guards should be grounded. This acts as a strong sink for electromagnetic fields outside the sensor, but also for the fields produced by the driving electrodes [6]. A schematic representation of this concept is shown in figure 2.4.

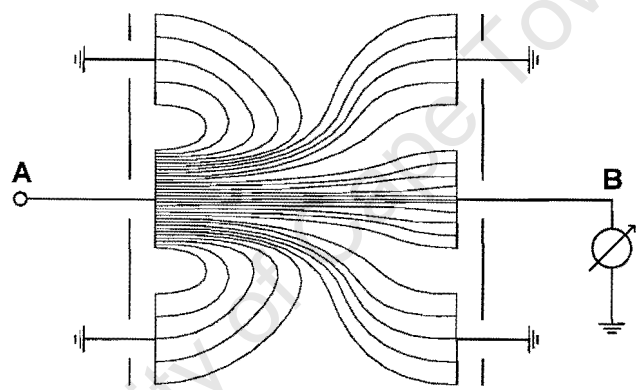

Figure 2.4: Schematic representation of the electric field formed between the transmitting electrode A and receiving electrode B, where their axial guards are earthed.

On the other hand, the axial guards could be used as driven guards. A two-dimensional image has to be reconstructed from a three-dimensional data [23, 24]. However by driving the axial guards a well-shielded compressed homogenous electrical field in the measurement volume is generated.

As can be seen from figure 2.5 on the next page, by driving the axial guards, the field created is parallel to the sensing region and can therefore be automatically simplified into a two-dimensional field [25]. However, Wang [26] disagrees with this concept and warns us that under heterogeneous conditions the driven guards introduce inconsistencies in the field and therefore do not form a compressed parallel field.

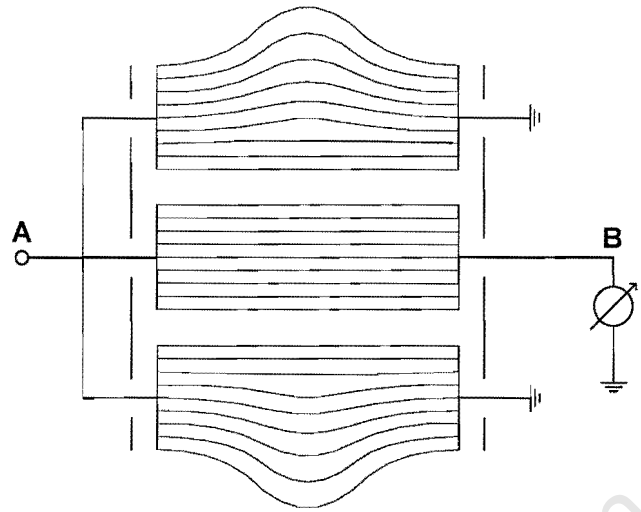

Figure 2.5: Schematic representation of the electric field formed between the transmitting electrode A and receiving electrode B, where their axial guards are driven.

Finally, while several of the electrode segments of the capacitive primary sensor are used during one measurement, others remain uninvolved. Those electrodes, according to Reinecke and Mewes [6, 19], could either be grounded as shown in figure 2.6(a) or they could left floating, as it is illustrated in figure 2.6(b).

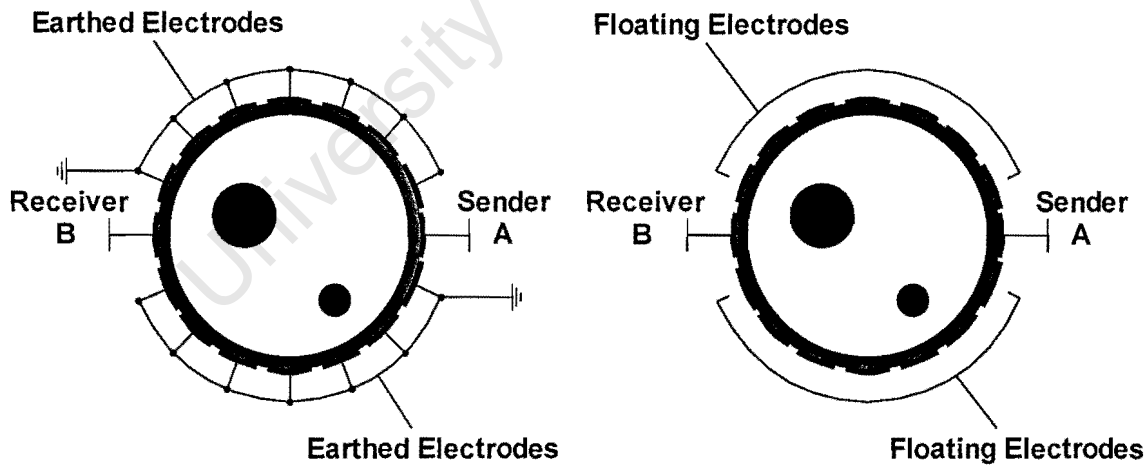

(a) (b)

Figure 2.6: Schematic diagram illustrating the switching state where only two sensing electrodes (A and B) are used, while the remaining free electrodes are (a) earthed and (b) floating.

A major advantage of the first case (see figure 2.6 (a)) is that only one driving electrode is present, while all the others can be used for the measurement in parallel. The second set up

(see figure 2.6 (b)) allows higher measurement values, as well as producing a more compact homogenous field [19].

2.1.1.2 Capacitance Measuring Techniques

The data acquisition system performs the task of switching between the desired electrode combinations and measuring the corresponding capacitance value. Two types of capacitance measuring circuits (used to measure the capacitance between two electrodes) are under investigation. The first is a charge/discharge circuit and the second is an AC-based circuit.

The charge/discharge capacitance measuring circuit in a differential configuration is shown in figure 2.7(a) and the switching waveforms in figure 2.7(b). Note that C_X is the unknown capacitance being measured. Also, the stray capacitors C_{S1} and C_{S2} have been grounded and capacitors C are smoothing capacitors, serving to protect the op-amps against switching voltage spikes.

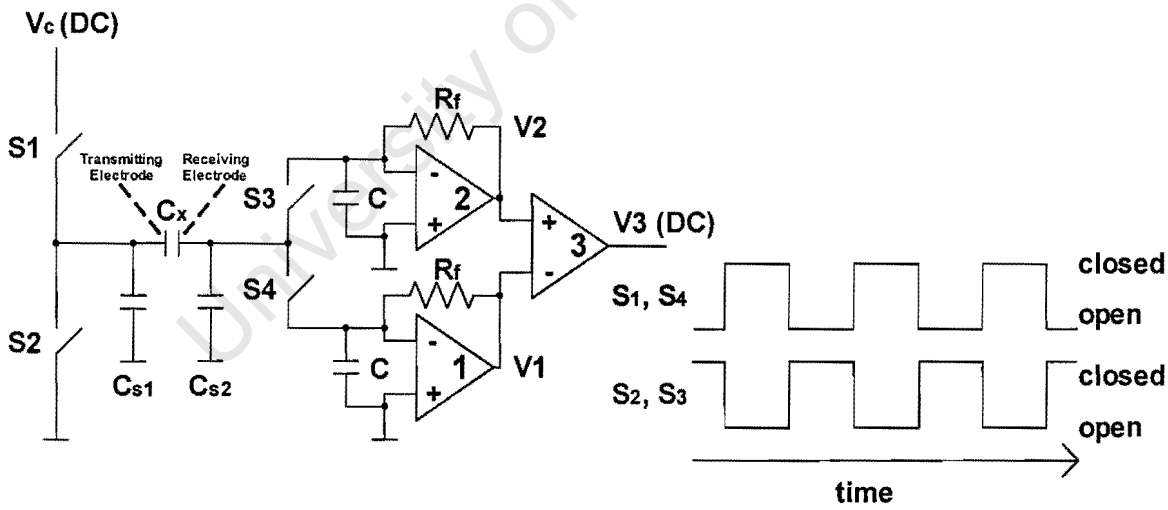

(a) (b)

Figure 2.7: (a) Differential charge/discharge capacitance transducer measuring the unknown capacitance C_X and (b) switching wave forms.

The output of this circuit is a dc measurement signal, which is proportional to the measured capacitance [8]. The main disadvantage of this transducer is that it suffers from a charge injection problem [18].

The AC-based capacitance measuring circuit is shown in figure 2.8. A sine-wave voltage (excitation source), Vi(t), is applied to the capacitance under measurement, C_X, producing an ac-input current. The op-amp's capacitance and resistance feedback (C_f and R_f respectively) converts this current into an ac-voltage. The feedback resistor is required to prevent the op-amp's output from drifting, which would eventually saturate the op-amp. Note that the stray capacitors C_{S1} and C_{S2} have been grounded. The output of this circuit is an ac-signal with a magnitude proportional to the measured capacitance [16, 27, 28].

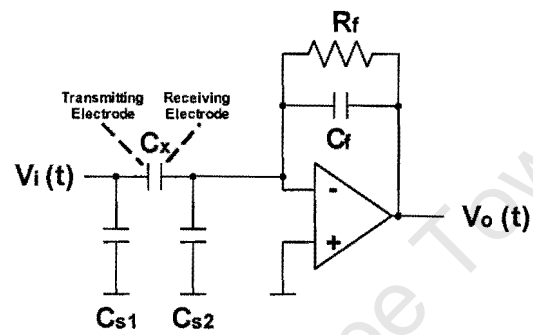

Figure 2.8: AC-based capacitance transducer measuring the unknown capacitance C_X. Capacitances C_{S1} and C_{S2} are stray capacitances.

This technique has the following benefits:

- Stability, due to a low baseline drift
- Accuracy, due to a high SNR
- Good stray immunity [6].

2.1.1.3 Data Collection Strategies

As has already been mentioned, the generation of linearly independent measurements, as illustrated in figure 2.9 on the next page, is done by sequentially measuring the capacitance between two electrodes (the driving electrode and the measuring electrode).

The standard data collection protocol for capacitance tomography is shown in figure 2.9. As can be seen in figure 2.9(a), in the first cycle the capacitance is measured between electrodes 1 and 2, in the second cycle between electrodes 1 and 3 (figure 2.9(b)), in the third cycle between electrodes 1 and 4 (figure 2.9(c)), and so on until all the capacitances have been collected.

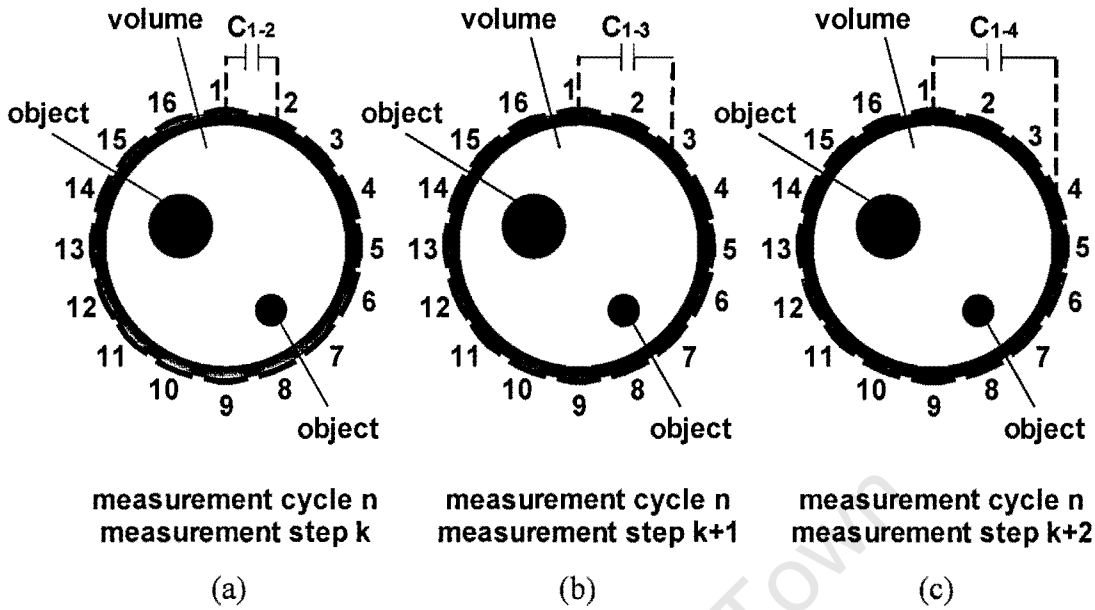

Figure 2.9: A schematic representation of the sequential sampling of the electrodes.

The resulting N number of linearly independent electrode combinations is given by $N = \frac{n}{2}(n-1)$, where n is the number of electrodes mounted on the rig.

Other data collection protocols also exist [29], but which one suitable depends entirely on the designer and the application that the tomography system is aimed for.

2.1.1.4 Image Reconstruction Techniques

Many algorithms aimed at the reconstruction of cross-sectional images depicting a dielectric distribution have been developed over the years. The most popular ones are those that use linear back projection (LBP), the reason being that LBP algorithms are the simplest in concept and the easiest to understand [6, 14]. It is however, very difficult to extract quantitative information from an LBP image [14]. Attempts have been made to use LBP algorithm equations in an iterative scheme, employing finite element modelling (FEM) and linearization [6, 14].

Other developers moved towards more computing intensive and accurate algorithms e.g.

the Model-based reconstruction (MOR) algorithm and the algebraic reconstruction technique (ART). The motivation for developing such algorithms was to be able to extract quantitative information from capacitance tomography data [14].

Lookup table methods were also developed. Such methods could give both high resolution and high speed, but they are highly application dependent and there will always be the risk that process conditions present in practice are not tabulated in the 'look-up' table [14].

Finally, reconstruction techniques based on artificial neural networks have also been developed for achieving both high speed and reasonably high accuracy [3, 4, 20, 30 and 31].

2.1.1.5 Applications of ECT

In the recent years, many areas of research for the application of capacitance tomography have come to light. Much of this research has been devoted to the imaging of non-conductive phases in vessels or pipelines. In general, ECT has been used for the monitoring of gas-liquid systems (gas-oil) [32], gas-solid systems (transportation of granular solids) [7], gas-gas systems (combustion processes) [6] and also multiphase systems [6].

2.1.2 Electrical Resistance Tomography

The measurement principle used in electrical resistance tomography is based on the fact that the resistance measured between two electrodes is a function of the resistivity of the components across the plane of interest, as well as their distribution. Therefore, by employing an array of equally spaced electrodes mounted into the periphery of the measurement volume, the collection of sets of linearly independent measurements of this resistivity is possible. These sets of linearly independent measurements, with the help of a reconstruction algorithm, can map the spatial distribution of resistivities within the measurement volume. As is the case of electrical capacitance tomography, quantitative information can be extracted by investigation of the mapping.

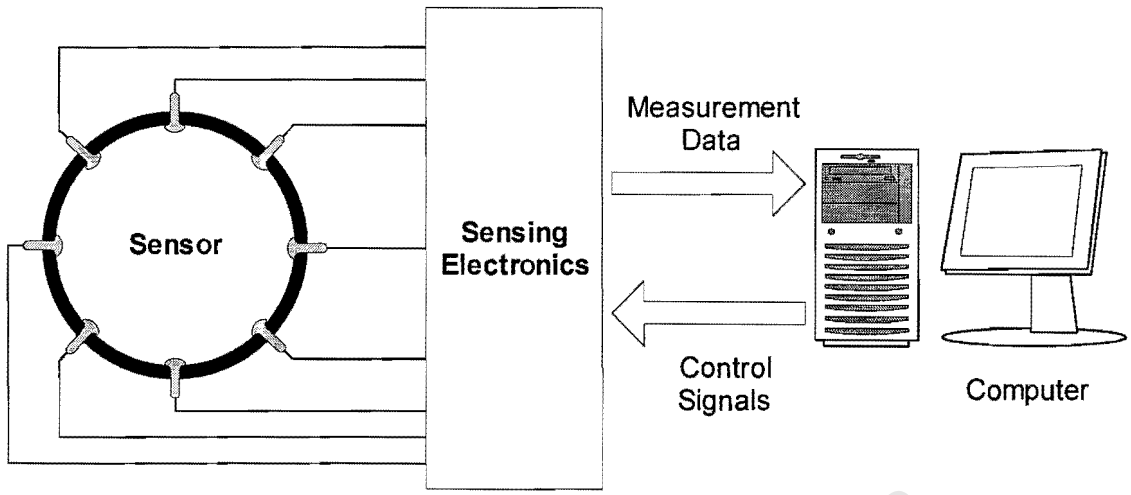

Figure 2.10: Block diagram of an ERT system with eight sensing electrodes.

As can be see from the block diagram in figure 2.10, the structure of a typical electrical resistance tomography (ERT) system is composed of three main parts:

- Sensors
- A data acquisition system (DAS)
- A system/host computer for image reconstruction or any other applications, e.g. velocity calculation for the phase or phases [9, 10 and 11] under investigation, and volumetric fraction predictions.

2.1.2.1 Sensors

Unlike the sensors employed for electrical capacitance tomography (ECT) (mentioned in section 2.1.1.1), the sensors in ERT systems must be in continuous electrical contact with the electrolyte inside the process vessel. In addition, according to Dickin and Wang [33], the sensors must be more conductive than the electrolyte in order to obtain reliable measurements.

For the majority of the process applications, the electrodes are metallic and can be fabricated from stainless steel, silver, gold, platinum, silver palladium or any other suitable material exhibiting a number of properties [33]. Furthermore, the sensor should be of low

cost, easy to fabricate and install, have good electrical conduction properties and be resistant to abrasion and corrosion.

The size of electrodes used, is also of high importance, considering that the most widely used resistance measurement method is the current-injecting and voltage measurement method.

Again, according to Pinheiro et al [34], a large surface area is required for the current-injecting electrodes, so that an even current density can be ensured across the area of interest. Pinheiro et al [34] also indicate that a small surface area, ideally a needle point, is required for the voltage measuring electrodes, so that the 'averaging' of several equipotentials is avoided. Further investigation from Wang et al [35], showed that the loss in measurement sensitivity as a result of using larger electrodes was minimal.

As in ECT, in ERT the number of electrodes which are equidistantly mounted into the periphery of the measurement volume vary considerably among the different tomographic systems developed. These variations depend upon the designer and the application or applications that the system is being designed for.

Once again, placing the sensing electrodes too close to one another will result in electrical interference between them [36].

An earthed radial shield guarding the measurement electrodes could also be used in ERT systems. Also axial guard electrodes place around, next to, or above and below the current-injecting, voltage measuring probes could be employed. Ma et al [24, 25] reveal in their study that guard electrodes would not only improve the uniformity of the sensing field distribution so that it might simulate the two-dimensional field better, but might also decrease the axial range of the measuring space. They also state that by keeping the probe dimensions constant, and increasing the guard electrode height, a more accurate two-dimensional field can be obtained. In addition the sensing probes could be kept relatively

closer to each other, due to the fact that the axial guard electrodes would prevent the sensing probes electrically interfering with each other [36].

2.1.2.2 Resistance Measuring Techniques

The data acquisition system (DAS) implemented by the ERT systems perform the functions of switching between all the possible probe combinations and also measuring the equivalent resistance values.

The standard method for measuring resistance used by most ERT systems involves the current-injection (alternating current because it has the advantage of eliminating any long-term polarization effects at the electrodes [37]) and voltage measurement method. This technique is illustrated in figure 2.11.

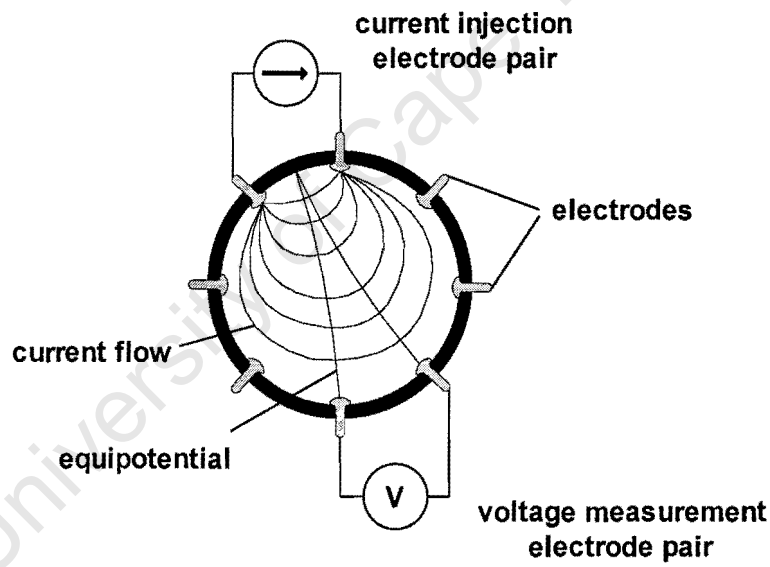

Figure 2.11: Diagram illustrating the current-injecting and voltage measuring method.

The potential difference between the two voltage sensing electrodes is usually measured by a differential amplifier, whose output is demodulated by a phase detector. The resultant signal is the low-pass filtered and a dc-signal proportional to the resistance is obtained.

2.1.2.3 Data Collection Strategies

Good data collection strategies are vital, as potentially misleading images can be reconstructed if a full set of independent measurements is not collected [33]. The data

collection strategies that are employed by most of the ERT systems are: the adjacent strategy, the opposite strategy, the diagonal strategy, and the conducting boundary strategy.

The adjacent strategy, illustrated in figure 2.12, is the most popular data collection strategy. According to this protocol, current is applied through two neighbouring electrodes and the voltages are measured from successive pairs of neighbouring electrodes. In the next cycle, current is then applied through the next pair of electrodes and the voltage measurement is repeated.

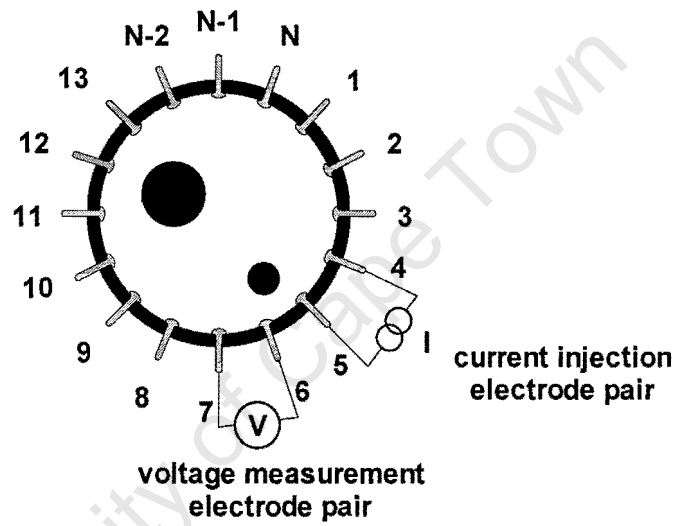

Figure 2.12: The adjacent measurement strategy.

Using this method the number, N, of independent measurements possible is given by the formula, $N = \frac{n}{2}(n-1)$, where n is the number of electrodes mounted into the rig. However, in order to avoid electrode/electrolyte contact impedance measurements [37], the voltage is not measured at a current-injecting electrodes and therefore the total number of independent measurements N, is reduced to $N = \frac{n}{2}(n-3)$.

The main disadvantage of the four-electrode adjacent pair measurement protocol is that since most of the injected current travels near the peripheral electrodes, a uniform distribution is not achieved [38].

The opposite strategy, shown in figure 2.13 on the next page, and as the name suggests, applies current through diametrically opposed electrodes.

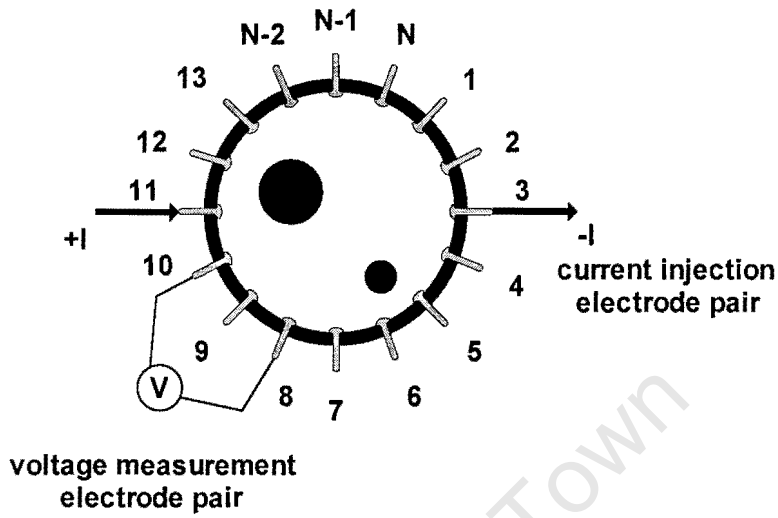

Figure 2.13: The opposite measurement strategy.

This protocol works as follows. The voltage reference is the electrode adjacent to the current injecting-electrode. Thus, for a particular pair of current-injecting electrodes, the voltages are measured with respect to the reference at all the electrodes except the current-injecting ones [33]. Using this method the number N, of independent measurements achieved is $N = \frac{n}{4}(\frac{3n}{2} - 1)$.

Thus, for n = 16, the above formula yields N = 92 compared to N = 120 for the adjacent strategy when contact impedance is not being avoided. Consequently, according to Dickin and Wang [33] the image resolution will be decreased by as much as 23% compared to the adjacent strategy for the same number of electrodes.

The diagonal strategy, is illustrated in figure 2.14 on the next page, and it is also known as the cross method. According to this protocol, current is injected between electrodes separated by large dimensions. For example, in a sixteen-electrode tomography system the data collection procedure is as follows: electrode 1 is fixed as the current reference probe and current is injected through this electrode and electrodes 3, 5, ..., 15 successively.

Electrode 2 is fixed as the voltage reference probe. Therefore, for each of the above current pairs the voltages from all electrodes except the current electrodes are measured with respect to electrode 2. The current and voltage references are then changed to electrode 4 and electrode 3 respectively, and the voltage measuring process is executed once more. The process carries on until all voltage measurements have been collected.

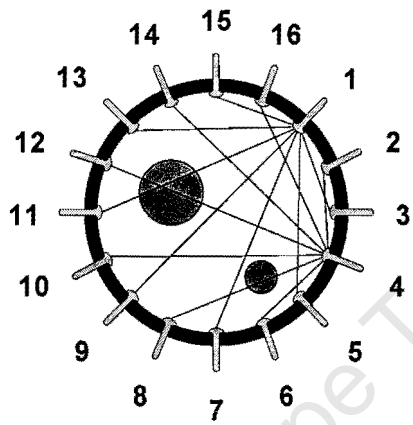

Figure 2.14: The diagonal measurement strategy.

The outcome, with respect to the adjacent strategy, is a more uniform current distribution in the region being imaged but it has lower sensitivity in the periphery compared to the adjacent method [33].

The conduction boundary strategy is shown in figure 2.15 on the next page. This protocol was devised by Wang et al [39] and also used by Yuen et al [40], for process vessels and pipelines with electrically conducting boundaries. The conducting boundary strategy employs only two electrodes, as opposed to the preceding four-electrode measurement strategies.

This protocol works as follows: by applying an alternating current between each one of the electrodes and the conducting vessel and measuring voltages between other electrodes and the vessel, the shunting effect from the metallic wall of the vessel is overcome and the amplitude of the resultant signal is significantly increased [39].

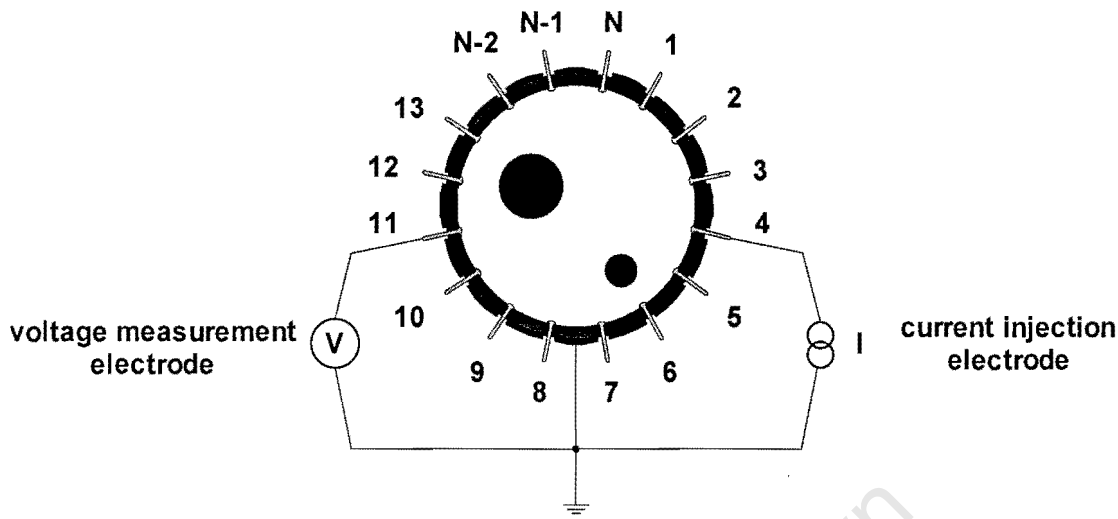

Figure 2.15: The conducting boundary measurement strategy.

According to Wang et al [39], the large grounded surface of the conducting boundary also provides a good electric shield to prevent extraneous electromagnetic interference from other industrial equipment.

2.1.2.4 Image Reconstruction Techniques

In order to determine the internal distribution of resistivities within the process vessel from measurements acquired from an array of electrodes mounted into the periphery, a number of reconstruction algorithms have been devised.

Most of them implement the back projection technique, using finite difference models (FDM) or finite element models (FEM) [33]. Also the use of Newton-Raphson algorithms or modified Newton-Raphson algorithms (MNR) is very popular [41].

2.1.2.5 Applications of ERT

Measurements of electrical resistivity via four electrodes are widely used in a variety of applications, mainly dealing with the imaging of conductive phase [33]. There are numerous aqueous-based processes to which ERT is suited. These applications range from geophysical prospecting to silicon wafer manufacturing, as well as for liquid-liquid mixing [33], solid-liquid mixing [42, 43] and cyclone separation [33].

2.2 Frequency Division Multiplexed Impedance Tomography

As was revealed in section 2.1, much research has been done to improve the primary sensor systems employed for time division multiplexing (TDM) tomography systems, as well as on speeding up the data acquisition systems (DAS). Also, a large amount of research has been done on the design of high-speed communication links for process tomography systems [44, 45] for the purpose of allowing on-line (real-time) monitoring of different processes [46].

A study done by Teague [3], shows that the data collection strategies implemented by most of the TDM tomography systems developed up until today, including the sixteen-electrode (eight capacitance and eight conductance) impedance tomography rig which measures 56 linearly independent measurements and obtains only one frame of data every two minutes used by Teague [3], would not be able to give the 200 frames/s that is needed for the real-time monitoring of the seawater-air-gravel application that our system is aimed at.

A new measurement technique therefore had to be developed. The following section will discuss the concept on which this new measurement technique is based.

2.2.1 The Theory of the Frequency Division Multiplexing Concept

As has already been stated, even though TDM systems are easy to implement, achieving a higher number of frames per second in these tomography systems relies on the fact that the overall time dedicated to the measurement process is increased due to the switching that takes place between the electrodes.

In this case (TDM) the data acquisition system implemented is used to do the sequential sampling of the electrodes and therefore in practise, a driving and a receiving (measuring) electrode can be identified. Most of the impedance TDM systems use a single capacitance and a single resistance sensing circuit, which are temporarily connected one at a time to the driving and receiving electrode. Once the output reading of the system is stable, the

measurement is taken and the sensing circuits are multiplexed serially between the remaining electrode combinations.

However, some TDM tomography systems use more than one sensing circuit [33] in order to obtain more than one capacitance or resistance measurement at the same time and therefore to achieve higher frame rates.

The frequency division multiplexing (FDM) technique used by the author is an extension of that concept, but it should not be confused with the technique used in spectroscopic frequency tomography [47].

Using the frequency division multiplexing measuring technique, the disadvantages of the slow overall measuring time suffered by the TDM tomography systems is surpassed by employing multiple dedicated drivers, all of which transmit simultaneously, each one operating at a different frequency.

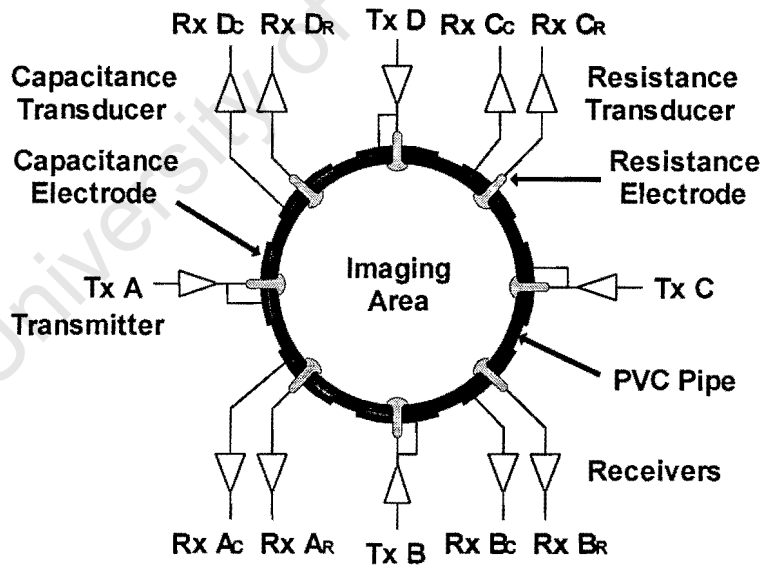

Figure 2.16: Cross-sectional view of an 8-electrode (8 capacitance plates and 8 resistance probes) vessel employing FDM, showing the transmitter/receiver arrangement employed by the author.

The system used by the author (illustrated in figure 2.16) consists of four dedicated transmitters and four dedicated receivers, with each receiver consisting of a capacitance and a resistance transducer.

In the primary sensing system, the probes used for resistance sensing are mounted into the vessel in the centre of the plates used for capacitance sensing. All sixteen electrodes are mounted equidistantly in groups of two around the vessel's periphery. A result of this is that the capacitance plates and the resistance probes are sensing the same measurement volume (plane of interest).

On the transmitters' side, four different sinusoidal signals are being transmitted continuously and simultaneously into the vessel. Each dedicated transmitter drives a plate and a probe with the same signal.

On the receivers' side, the four dedicated receivers collect all the sinusoidal signals transmitted by the four drivers simultaneously. Every receiver will receive eight signals. Since each one of them is connected to a capacitance plate and a resistance probe, four of those signals will be received by the capacitance transducer and the other four signals will be received by the resistance transducer.

Let's take receiver A as an example. Receiver A will receive two signals, one on the capacitance plate and one on the resistance probe, from transmitter A modulated by the material between receiver A and transmitter A. It will also receive two signals, one on the capacitance plate and one on the resistance probe, from transmitter B modulated by the material between receiver A and transmitter B and similarly for transmitters C and D. The same process is applied to receiver B, receiver C and receiver D.

The receiver circuitry is able to separate the received signals into the components corresponding to the different current paths, with the help of synchronous detection. This process is illustrated in figure 2.17 on the next page.

As can be seen, in figure 2.17, the way that synchronous detection works is by employing a reference signal coherent with the signal applied on the transmitting plate and probe, to extract the resistance of a particular path, while a 90^0 phase-shifted version of the same reference signal extracts the capacitance of that path. The signals are then amplified

individually, optimising their dynamic range, and then are low-pass filtered, so that dc-signals whose magnitudes are proportional to the capacitance and resistance of the specific path can be obtained.

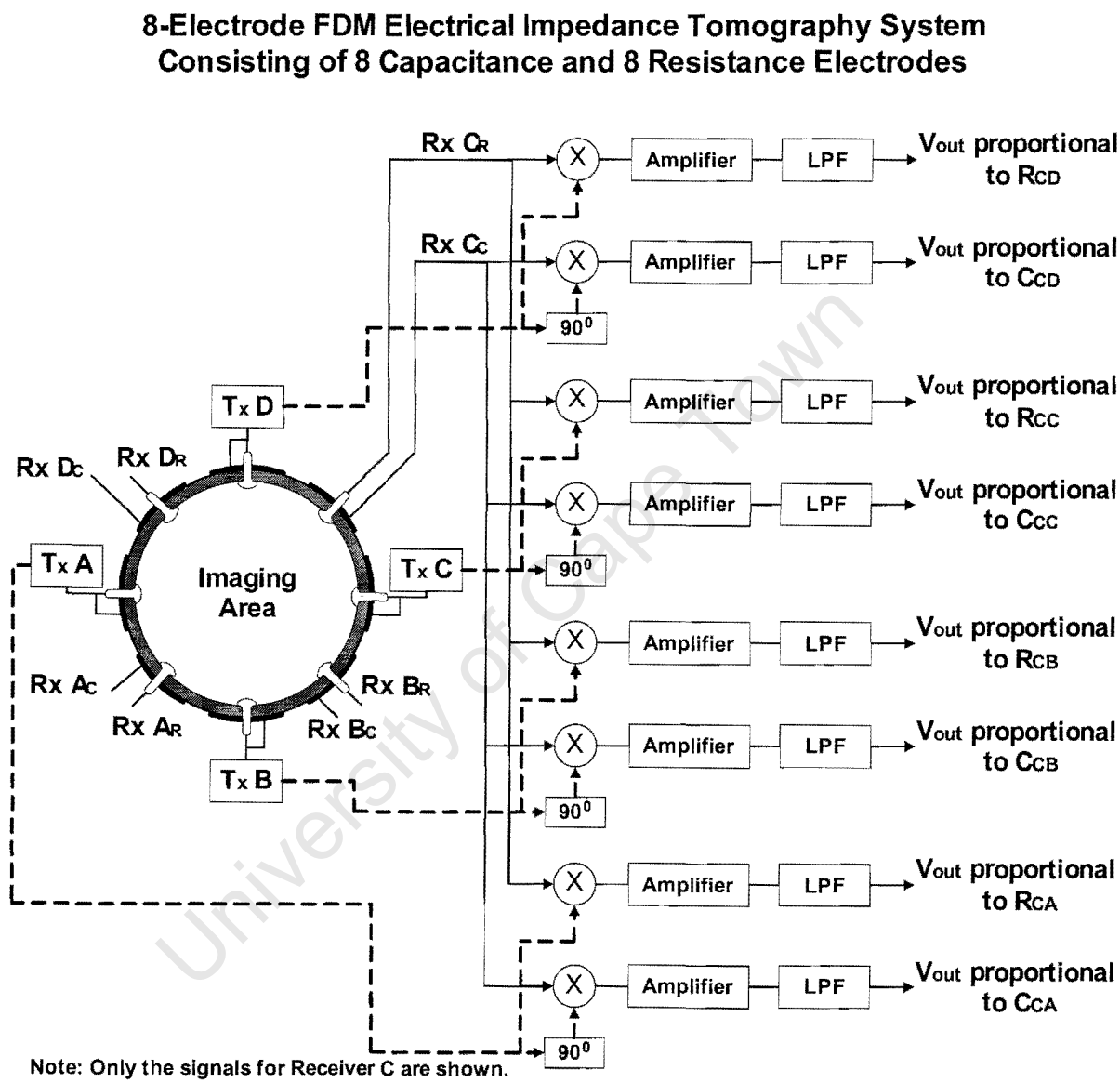

Figure 2.17: Block diagram representation of the synchronous detection performed to the signals obtained from receiver C.

From the above discussion the reader can see that no switching takes place between different electrode combinations and therefore the sensing circuitry is immune to the resistance and capacitance of the switching circuitry (used by most TDM tomography

systems). Also much higher data frame rates can be achieved by any system that uses this technique, with the only limiting factors being the bandwidth of the sensor electronics and the ability of the DAS to capture those dc-voltages at the required data frame rates.

The main disadvantage of this technique is that the number of linear independent measurements N, obtained by this technique is given by the formula, $N = \frac{n^2}{8}$, where n is the number of electrodes used. Therefore, for the 16-electrode system described above the number of independent measurements is 32.

However if a higher number of electrodes is used, then higher resolution images may be achieved. Another rig, employing thirty-two sensing electrodes and using the same FDM technique described previously, but using square waves is being developed at the moment to verify such an assumption.

CHAPTER 3

3. NEURAL NETWORKS

This section is intended to provide the reader with a general understanding of what a neural network is, as well as an introduction to the architecture of the multi-layer perceptron, as used by the software program employed by the author in order for reconstruction of the different cross-sectional images of the vessel, and retrieval of the volume fraction predictions of the three phases (seawater-air-gravel) under investigation.

The feed-forward architecture, as well as the regression techniques implemented by the software program, developed by G. Teague, is the only neural network discussed. According to G. Teague's BSc. Thesis for the University of Cape Town [3], a number of different neural networks, intended for the same application, were investigated. The multi-layer feed-forward neural network gave the most satisfactory results.

3.1 Neural Networks Fundamentals

Neural networks have received much attention from the research community over the years. It is worth noting that the topic of neural networks is given various names by the different authors, such as: artificial neural systems, connectionist models, parallel distributed processing models, layered self-adaptive systems, self-organizing systems, neurocomputers etc. There are various subtle differences between the definitions the authors use, but they are all roughly synonymous [48].

According to Greene [49], a neural network is defined as a highly parameterized mathematical function, and can be described as a layered network of neurons. This mathematical function can provide a general framework for representing a non-linear functional mapping [3].

The neurons will often be represented by a weighted linear sum, z_j, of the input signals followed by a linear or a non-linear function, $y_j = f(z_j)$ [44]. The function $f(z_j)$ is called an activation function, and this function's role is to determine the output activity of the specific neuron by using the input value. One typical case, as described by equation 3.1, uses a binary threshold function [45],

$$y_j = f(z_j) = \begin{cases} ON & if\ z_j > threshold \\ OFF & if\ z_j < threshold \end{cases} \qquad (3.1)$$

Different neural networks use different $f(z_j)$ functions, but the internal structure of the neuron, i.e. linear sum followed by a function $f(z_j)$, is common to most networks [48]. In addition to the threshold function, such as the one shown in equation 3.1, the activation function, f(), can also be a linear function or a non-linear function.

The weights and the activation function dictate the operation of the network [49]. However varying the weights will allow the network to carry out different computations, since usually the activate function, f(), is fixed. Neural networks can have either adaptive weights or fixed weights.

Neural networks that use adaptive weights employ learning laws to adjust the values of the interconnection strengths. On the other hand, the neural networks that use fixed weights must be able to determine their weights explicitly from the description of the problem. Therefore the task that they have to accomplish must be well defined a priori.

There are two types of learning laws: supervised and unsupervised. Supervised learning occurs when the network is supplied with both the input values and the correct output values, and the network adjusts its weights based upon the error of the computed output. Unsupervised learning occurs when the network is only provided with the input values, and it has to adjust the interconnection strengths based solely on the input values and the current network output. Learning laws define how the network is to adjust its weights using an error function or some other criteria [48].

A major advantage of neural networks over the standard computing methods is their ability

to generalize for previously unseen input variables, if, of course, there is sufficient information within the input set of variables to predict the correct output.

Also, according to Adler and Guard [50], higher accuracy of the reconstructed image can be expected by neural networks, due to the fact that they are simply trained by example and do not make various assumptions like other standard reconstruction techniques. Careful implementation of neural networks could also provide the user with the advantage of real-time imaging of fast changing processes [20, 30 and 31].

3.2 Architecture of the Multi-layer Perceptron

The perceptron is the basic element in many neural network architectures. Neural network architectures can be classified in two groups based upon their operation during the recall phase. These two groups are: feed-forward and feed-back. As has already been mentioned, only the feed-forward multi-layer perceptron is dealt with here, since it has consistently out-performed radial basis function neural networks [3].

According to Greene [49], a multi-layer perceptron is a densely interconnected, layered network of neurons. As is illustrated in figure 3.1 on the next page, a feed-forward multi-layer perceptron neural network consists of an input layer, which performs a distributive task, a hidden or a number of hidden layers, and an output layer.

Each layer contains a number of neurons, and each neuron has a corresponding set of adaptable weights. The role that the adaptive weights play is to specify the strength of connection between the actual neuron and the previous layer of neurons. The number of hidden layers in the neural network is equal to the number of layers formed by the adaptive weights [3].

In a feed-forward network the output of any given neuron cannot be fed back to itself directly or indirectly through other neurons. Thus its present output does not influence future outputs [48]. In these networks computations are completed in a single pass.

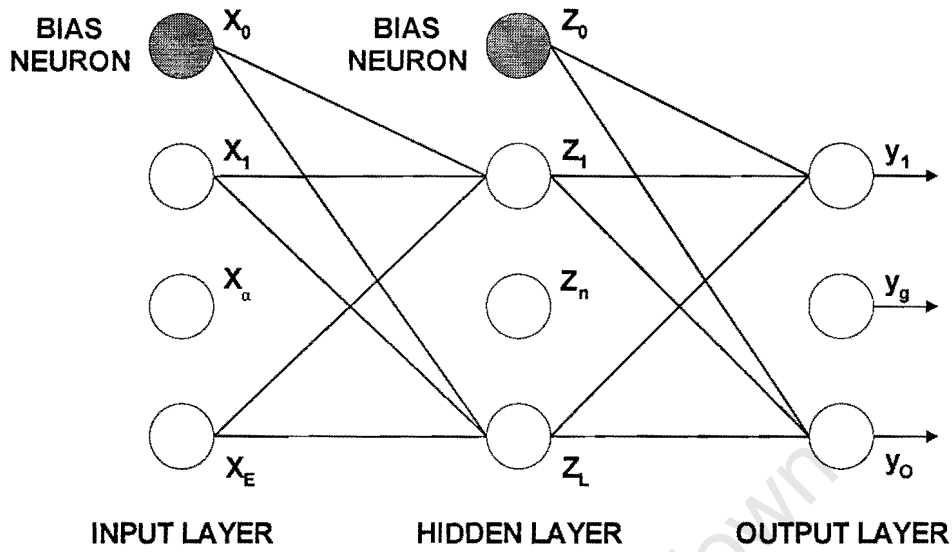

Figure 3.1: General structure of a double-layer feed-forward neural network, showing an input layer, which performs a distributive task, a hidden layer, and an output layer.

When an input pattern is presented to the input terminals of a network, the neurons in the first layer compute output values and pass these values onto the next layer. Each layer in turn receives input values from the previous layer, computes output values and passes these values onto the next layer. When the output values of the final layer are determined the computation ends. The rule can only be broken during the training phase or the learning portion of the recall phase, when the output of a neuron can be used to adjust its weights, thus influencing future outputs of the neuron.

As is illustrated in figure 3.2 on the next page, every neuron consists of a combination and an activation function. Therefore, if, for example, we take neuron L, its combination function is the weighted-sum of its inputs. This can be expressed mathematically as [51]:

$$a_L = \sum_{\alpha=0}^{E} x_\alpha w_{L\alpha} \qquad (3.2)$$

Note the $w_{L\alpha}$ is the weight specifying the strength of connection between neuron L in the hidden layer and neuron α in the input layer.

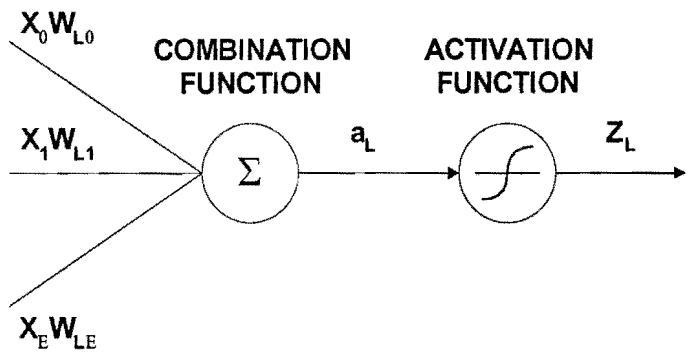

Figure 3.2: Neuron L.

From figure 3.2 it can be seen that a_L is next going through the activation function $g(a_L)$, and therefore the output of neuron L can be expressed as $z_L = g(a_L)$.

The activation function can be a logistic sigmoid, a hyperbolic tangent, or even a linear function. Its main goal is to introduce a non-linearity into the neural network so that the network will be able to model a non-linear functional mapping between the input and the output variable [3].

The software program employed by the author uses the hyperbolic tangent activation functions for two-phase (seawater-air or seawater-gravel) image reconstruction and volume fraction predictions. The hyperbolic tangent can result in faster training since both positive and negative outputs are possible [3]. For three-phase (seawater-air-gravel) image reconstruction and volume fraction prediction, the software program employs 1-of-C output layer encoding [3].

Finally, training a neural network determines the position and orientation of the decision boundary. To accomplish this, two things have to be determined. Firstly, the derivative of the error function with respect to network weights needs to be calculated. This can be done by using the back-propagation algorithm [3]. Secondly, the computed derivatives are used to adjust the weights in the network in order to minimize the error function. This can be done by using the gradient descent or the resilient back-propagation algorithms [3].

CHAPTER 4

4. EIT SYSTEM STRUCTURE

This chapter describes the different modules that were combined to implement a frequency division multiplexed (FDM) electrical impedance tomography (EIT) system to monitor the changes in capacitance and resistance caused by the insertion of air and/or gravel in a seawater medium. This information was also transmitted to a computer and stored in databases to be used later for training and testing of the neural network.

Since this project also serves as a means of determining if the cross-sectional image reconstruction and volume fraction predictions could be improved by using sine-wave excitation, the author used the primary sensor system (8 capacitance and 8 resistance electrode rig) and air-tube and gravel-bubble placement system (described in chapter 5) that was used by Teague in his Ph.D. study [53].

Nonetheless, in designing the system hardware the author took into consideration a possible upgrade of the 8-electrode EIT system to a 16-electrode (16 capacitance and 16 resistance electrodes) EIT system, and therefore provisions for such a system were made.

The main components (see figure 4.1 on the next page) of the system are:

- The primary sensor system,
- The frequency generation boards (2 boards providing 4 different sine-waves and their quadratures),
- The transmitter and receiver boards (4 boards each),
- The synchronous detection boards (4 boards) and,
- The sample controller board interfacing with the EIT system and the PC30G data acquisition card.

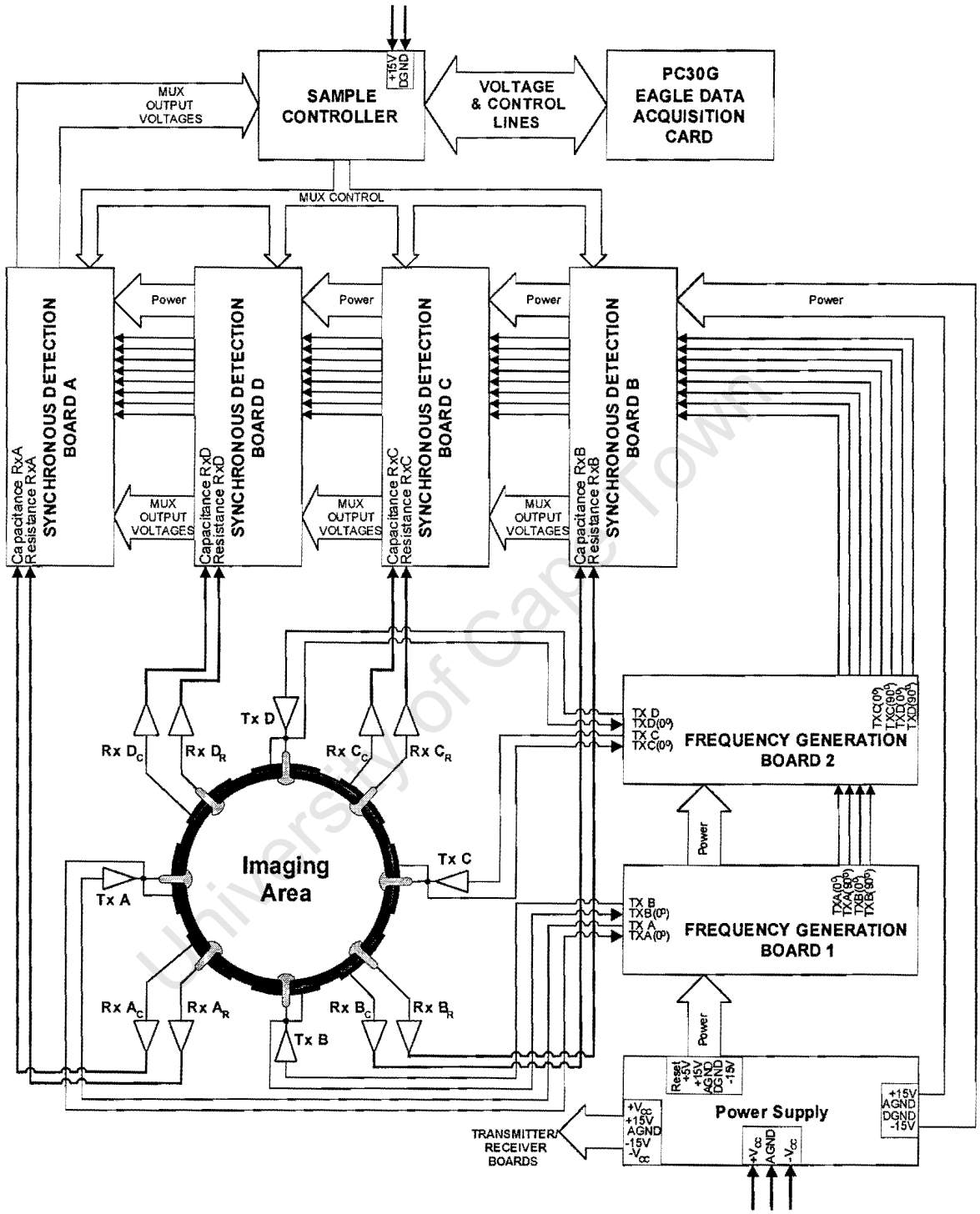

Figure 4.1: Block diagram illustrating the interactions between the different circuit boards in a 8-electrode frequency division multiplexed impedance tomography system.

4.1 Primary Sensor System

An extensive study (covered in Chapter 2) was done by the author covering the following topics:

- Attaining a better 2D electric field inside the area of interest,
- Improving isolation between electrodes for minimum interference between the capacitance and resistance electrodes, as well as electromagnetic interference.

These concepts were however not implemented in the design of the system simply because such precautions were not taken by Teague [53], and a comparison of the author's EIT system with Teague's [53] 8-electrode EIT system employing square-wave excitation instead of sinusoidal excitation was more important.

The rig, illustrated in figure 4.2, which was also used in previous research projects [1, 2, 3, 4, 53], is constructed from a PVC pipe with an inside diameter of 220mm, an outside diameter of 250mm, and a height of 300mm.

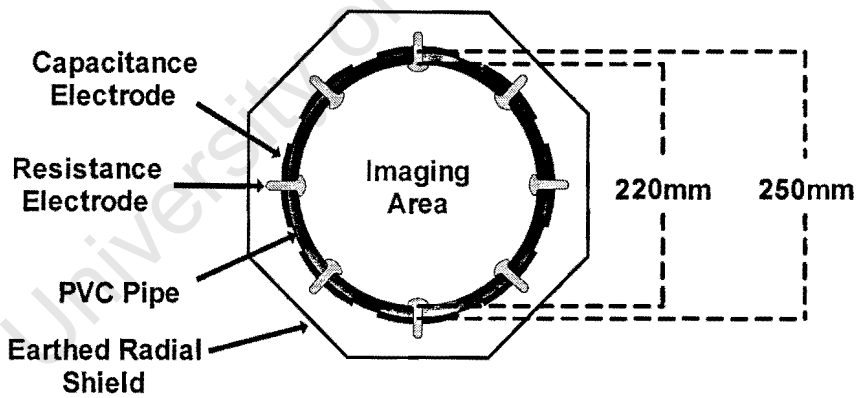

Figure 4.2: Primary sensor system using 8-capacitance and 8-resistances electrodes.

The PVC pipe (rig) is positioned vertically throughout the project and its one end is sealed so that seawater can be retained at all times. An array of capacitance electrodes is mounted peripherally and equidistantly around the measurement volume. This array consists of eight galvanized steel plates. Also, at the centre of each capacitance plate is a 6mm stainless steel machine screw threaded through the rig's wall and used as a resistance

probe. The 8 resistance probes are ground flush with the inside pipe wall and therefore are in constant contact with the seawater contained by the rig.

In addition an earthed radial shield is placed around the rig so that electromagnetic interference can be avoided.

4.2 The EIT Sensor Electronics

This section covers in detail all the hardware modules that were designed for an 8-electrode EIT system employing FDM and using sine-wave excitation.

4.2.1 Frequency Generation

As has been mentioned previously, the author used FDM impedance tomography employing sine-wave excitations. One of the many reasons for adopting sine-wave excitation in the system was due to the fact that the previous research [53] showed that even though generating a square-wave frequency and its quadrature was an easy and cost effective process, the use of all four square-wave frequencies simultaneously (in an 8-electrode system) or 8 square-wave frequencies (in a 16-electrode system) was not an easy task at all. Keeping a clean, noise free, 200Hz pass-band (as required by the system), proved to be difficult.

It was decided that each sine-wave and its quadrature would be generated independently of all other frequencies and their quadratures by using PIC16F84A microcontrollers. Therefore the 4 sine-waves and their quadratures required by the 8-electrode system were generated using four PIC16F84A microcontrollers, since this type of microcontroller is accurate, simple and very easy to program. Hence, a wide variety of sine-waves and their 90^0 phase shifted versions could be generated by either modifying the code on the microcontroller or by changing the microcontroller's external crystal.

Initially, an attempt was made to generate 16 different sine-wave frequencies, trying to compensate for the possibility of using the same data acquisition system (DAS) for a dual 16-electode impedance tomography system using frequency division multiplexing. The

frequency range from which the frequencies were to be chosen was from 15kHz to 78.125kHz, with the PIC microcontrollers being able to provide 127 individual frequencies within that range.

The reasons behind choosing such a range of frequencies were:

- Useful capacitance and resistance results were obtained for the specific 8-electrode system by using any sine-wave frequencies from 15kHz and above.
- 78.125kHz was the highest sine-wave frequency that could be generated by the PIC16F84A microcontroller.
- Since a two-electrode measurement protocol was chosen for the resistance measurements, the contact impedance, which is a result of the electrochemical reaction taking place between the stainless steel resistance probes and the ionic solution (seawater), becomes a very important parameter. According to Hervieu and Seleghim [55], this contact impedance becomes negligible (for the case where only one of the phases is conductive) if a sufficiently high excitation frequency is used. However, excessively high frequencies should be avoided, as electromagnetic effects and external noise become a problem.

The output sine-waves and their quadratures were generated by hard-coding the microcontrollers with port set instructions, 'NOP' instructions and a 'GOTO' instructions at the end of the sequence ensuring that the loop repeated and the sine-waves and their 90^0 phase shifted versions are transmitted again.

Figure 4.3 on the next page, illustrates a block diagram representation of one of the two frequency generator boards used in the 8-electode impedance tomography rig. The circuit diagram details of the frequency generation boards are provided in Appendix C on page 138.

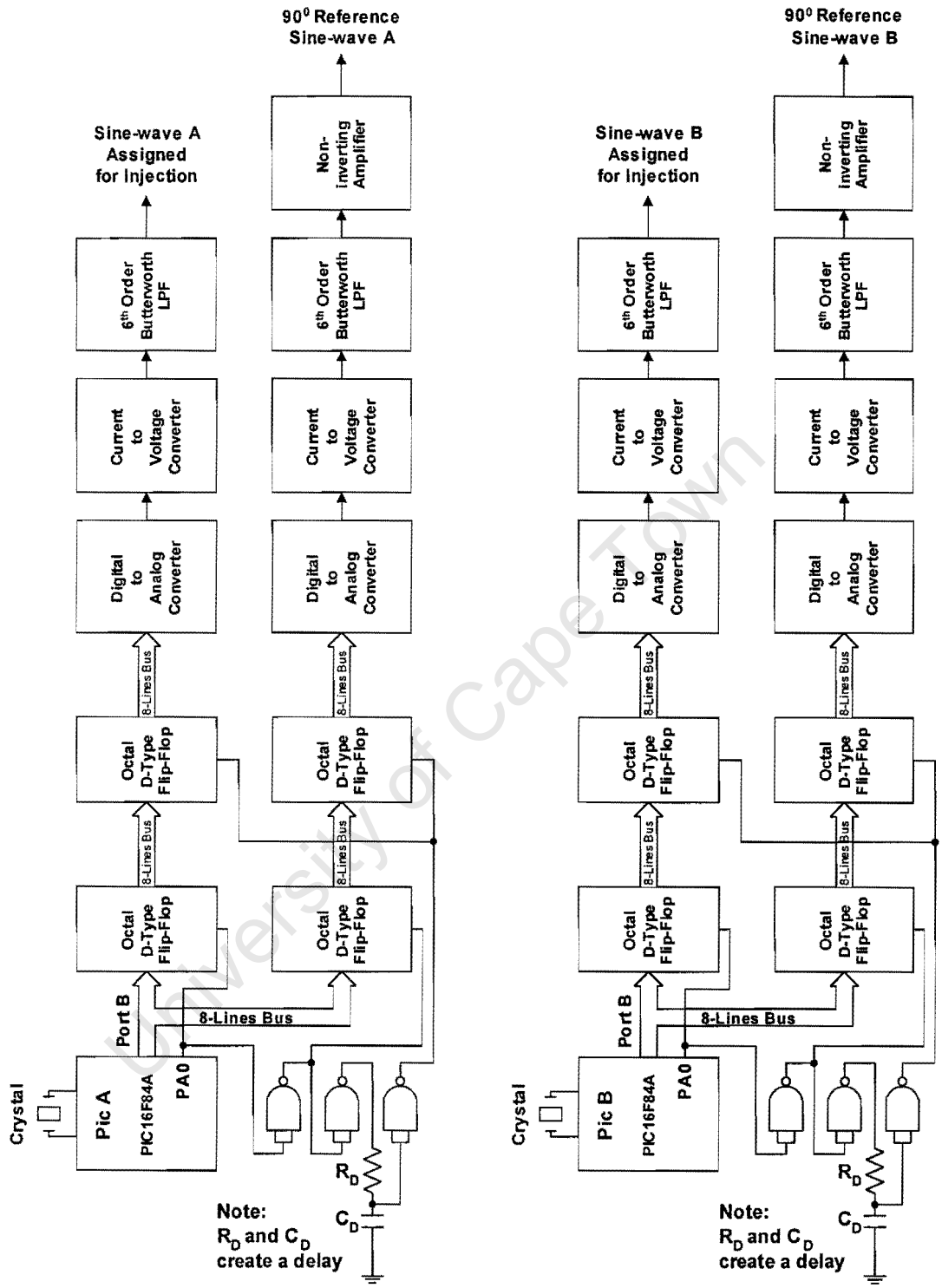

Figure 4.3: Block diagram of a frequency generation board depicting the generation of two sine-waves and their 90^0 phase-shifted versions.

The frequency generation boards work as follows. Each board generates two frequencies and their 90^0 phase-shifted versions. Tests showed that representing each sine-wave digitally by using eight discrete samples for the transmitted frequency and eight discrete samples for its quadrature (used for demodulating the capacitance signals obtained by the system) were more than adequate. These 16 samples are stored on to a PIC and spaced equally with 'NOP' instructions. The codes used for generating the final 4 transmitted frequencies and their quadratures are contained in Appendix A on page 129.

Port B of the PIC16F84A microcontroller is an 8-pin bi-directional port, used only as an output port in this application. It is used to supply the discrete samples of the required sine-wave and its quadrature sine-wave to the inputs of two octal D-type flip-flops, where they are clock to the outputs of the flip-flops, one at a time (first the injection sine-wave and then its 90^0 phase-shifted version) with the help of pin PA0 of port A of the PIC and a NAND gate (see figure 4.3). After a fixed external delay, formed by an RC combination, the outputs of the first set of flip-flops are clocked simultaneously through another set of octal D-type flip-flops and fed individually to the rest of the circuit.

The 16 discrete samples making up the required sine-waves and their quadratures are then converted from their binary representation to analogue signals and low-pass filtered to give the required sine-waves. Even though this technique is laborious, it can provide a sine-wave and its quadrature with an accuracy of $\pm 0.5^0$ to each other.

Table 4.1 contains the 16 frequencies and the crystals used by the PICs in order to generate the required frequencies by using the above described method. Since the author was only experimenting with an 8-electrode rig employing frequency division multiplexing, only the first four frequencies were required to be implemented by his system. The reason for choosing this set of frequencies (grouping them like that) was to determine whether the filtering provided by the system was enough for such minimal frequency separation. The author wanted to used the first 8 frequencies for the 1^{st} 16-elecrode tomography system and the remaining 8 frequencies for the 2^{nd} 16-electrode tomography system (dual 16-electrode system) in the case where the filtering provide by the system was satisfactory. In

the case where such filtering was not provided by the system, the author could try to used the 1st, 3rd, 5th, ... frequencies for the 1st 16-elecrode tomography system and the 2nd, 4th, 6th, ... frequencies for the 2nd 16-electrode tomography system.

Possible Sine-Wave Frequencies for a Dual 16-Electrode FDM Impedance Tomography Rig					
Numbers	Frequencies (Hz)	Crystals (MHz)	Numbers	Frequencies (Hz)	Crystals (MHz)
1st	20833.33	20	9th	42656.25	16.38
2nd	23809.52	16	10th	45454.55	16
3rd	26315.79	16	11th	48076.92	20
4th	28846.15	12	12th	52083.33	20
5th	31418.18	11.0592	13th	56875	16.38
6th	34125	16.38	14th	63984.38	16.38
7th	36764.71	20	15th	69444.44	20
8th	39375	16.38	16th	78125	10

Table 4.1: Table containing 16 frequencies that can be provided by the PIC16F84A microcontrollers, employed by the system, in the case where a dual 16-electode FDM impedance tomography rig was to be implemented.

Initial tests showed that beside the 2nd and 3rd harmonics of the fundamental frequencies, as listed in table 4.1, being introduced into the system by the power op-amps used by the transmitter boards (covered in section 4.2.2), many other frequency components were present at the outputs of the receivers (covered in section 4.2.3).

It was established that the rig, which was filled with seawater, acted as a signal mixer. For example, let us consider two of the frequencies, f1 and f2, which are injected into the rig. The output signals presented by the system, before any processing was performed, contained the following frequency components: f1, f2, 2f1, 2f2, 3f1, 3f2, f2±f1, f1± (f2-f1), f1± (f2+f1), f2± (f2-f1), f2± (f2+f1) and so on.

After multiplying these component frequencies with the reference sine-waves (and their quadratures), unwanted components were present in the system's 200Hz pass-band. Tests also showed that the above problem was not present when tap water was placed into the

rig. This suggested that the high conductivity and associated electrolytic chemistry of the seawater created the signal mixing.

Therefore, a different approach of obtaining a set of frequencies had to be developed where the system would not have to suffer from the above problem. A similar approach to the one employed by Teague [53] was used by the author to solve the above problem. The approach required the use of an optimisation search algorithm, employing Population-Based Incremental Learning or PBIL, to determine a set of 16 output frequencies that produce the optimal frequency separation and hence minimal output ripple.

Population-Based Incremental Learning is a simple but powerful stochastic (i.e. non-deterministic) search algorithm. It can be considered to be an abstraction of the simple Generic Algorithm, in that its dynamics closely resemble those of the latter [54]. However, it is simpler to implement and considerably more effective, both in numeric optimization and combinational searches [54].

The author used a program, which implemented PBIL and was written by Teague [53] but was modified by the author to suit his needs. The code for the program is contained in Appendix B on page 133.

The PBIL program could only supply 8 frequencies that produced the optimal frequency separation, which resulted in no interference within the 200Hz pass-band.

Initially the algorithm obtains a set of possible transmitter frequencies by using the standard crystal frequencies available with the number of 'NOP' instructions that are required by the system to obtain the required frequency. Using this way of generating the sine-wave frequencies, a set of 127 different frequencies between 15kHz and 78.125kHz are generated by the program. Then a trial solution represented by a 64-bit binary sequence is obtained, where each byte corresponds to one of the 127 different frequencies, which are also being indexed by an 8-bit binary value. The number of maximum generations and trial solutions are set by the user, and the code also supplies the user with the minimum ripple

frequency on the outputs of the synchronous detectors for a given set of transmitter frequencies. In the end the code supplies the user with 8-frequencies, with optimal frequency separation and minimal output ripple.

I would like to mention here that that even though the frequencies that were obtained by the code eliminated the initial problem i.e. no unwanted frequency components were present in the system's pass-band, some noise contributed to the system by the 50Hz $220V_{AC}$ (Mains) was present. Table 4.2 contains the 8-frequncies that were obtained using PBIL. The first four frequencies were implemented in the 8-electrode FDM impedance tomography rig by the author.

Possible Sine-Wave Frequencies for a 16-Electrode FDM Impedance Tomography Rig		
Numbers	Frequencies (Hz)	Crystals (MHz)
1st	24375	16.38
2nd	37500	12
3rd	39375	16.38
4th	46875	12
5th	50000	16
6th	56875	16.38
7th	62500	16
8th	78125	20

Table 4.2: Table containing the 8 frequencies that will be used in the case where a 16-electrode FDM impedance tomography rig is to be implemented.

4.2.2 Injection of Signals into the Rig

The FDM impedance tomography system uses four transmitter boards. The boards are mounted around the rig and each one of them is positioned next to a specific transmitting plate and probe. The transmitter path for the capacitance plate and the resistance probe is the same and therefore the resistance probe is mounted directly in the centre of the capacitance plate and the transmitter plate and probe are in direct contact with each other (see figure 4.4 on the next page).

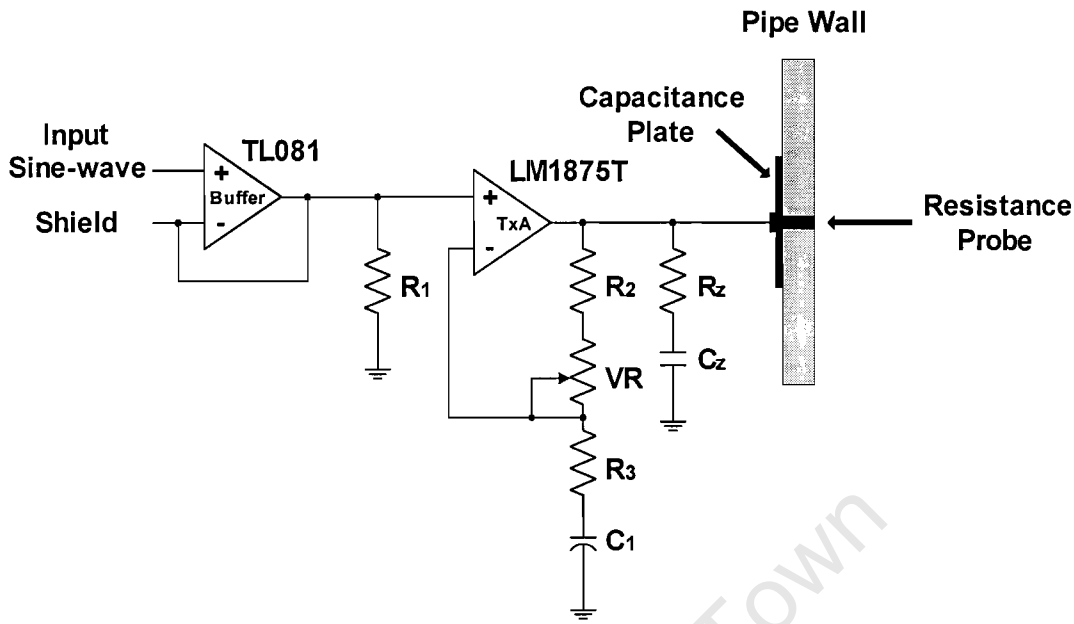

Figure 4.4: Diagram of the transmitter for an 8-electrode frequency division multiplexed impedance tomography system.

The task of the driver board is to amplify and inject into the rig one of the two different frequency sine-waves provided by each frequency generating board. As already mentioned, each frequency generating board provides two different sine-waves and their quadratures to the system. Measurements of resistance obtained by an LCR meter (Escort – ELC2260 – LCR Meter) showed that the average resistance between an electrode pair is approximately 50Ω. Since each driver board effectively drives four receivers in parallel the average load impedance becomes 12.5Ω and therefore a power op-amp was required to perform the driving.

The power op-amp used was an LM1875T which was configured in the non-inverting mode (see figure 4.4) and was preceded by an op-amp (TL081) configured as a buffer, so that the capacitance of the cable used to provide the sine-wave from the frequency generating board to the transmitter board could be eliminated. The circuit details are provided in Appendix C on page 139.

Although this power op-amp proved to be a capable driver for the load presented by the 8-

electrode rig, further research will have to be done for an op-amp with higher gain-bandwidth product than the one provided by the LM1875T, if the same driver boards are to be used for the implementation of a 16-electrode rig. Also, the monitoring of its output, using a spectrum analyzer, showed evidence of distortion introduced into the system by the specific power op-amp. In general, small frequency components of the 2nd and 3rd harmonics of the fundamental transmitted frequency were present on its output.

Finally due to the electrochemical reactions between the seawater and the resistance probes, corrosion of the resistance probes started to be come evident.

4.2.3 Receiving Capacitance and Resistance Signals

The FDM impedance tomography system uses four receiver boards. The boards are mounted around the rig and each one of them is placed next to a specific receiver capacitance plate and resistance probe. As illustrated in figure 4.5 the capacitance and resistance paths are isolated. The capacitance receiver plates have a larger centre hole than the capacitance transmitter plates to ensure that there is no electrical contact between the capacitance plates and the resistance probes.

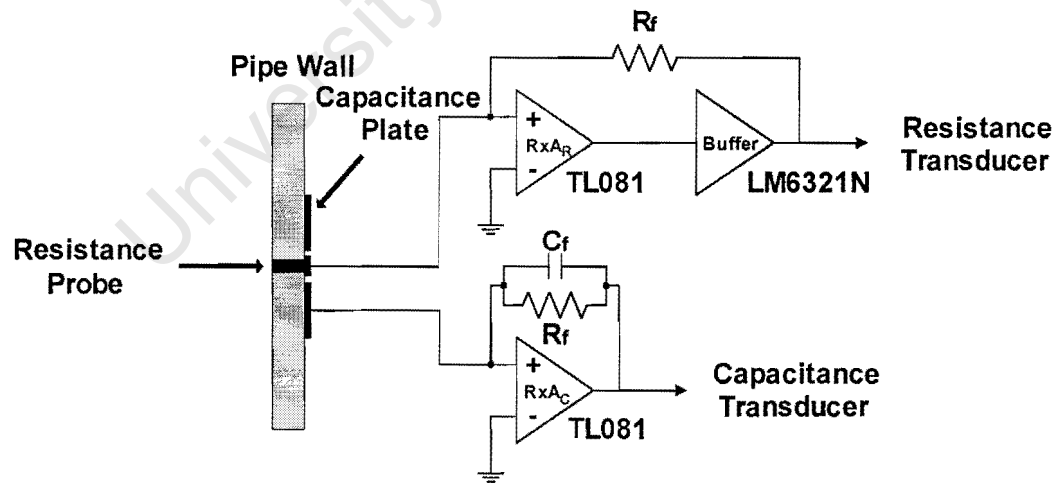

Figure 4.5: Diagram of the receiver for an 8-electrode frequency division multiplexed impedance tomography system.

The task of the receiver boards is to detect and feed through (to the rest of the system) any capacitance and/or resistance fluctuations that might occur in the measurement volume.

Figure 4.5 on the previous page, depicts a simplified diagram of the receiver board which consists of a capacitance and a resistance transducer.

The resistance receiver consists of an op-amp (TL081) and a buffer (LM6321N) with a high current output. The role of the buffer is to provide the required current to the feedback resistor (R_f) so that the op-amp does not saturate. The way the resistance transducer works is as the non-conductive phases (air and gravel) are being inserted in the third phase (seawater), the measured resistance between the electrode pairs increases and the amplitude of the waveform decreases.

The capacitance receiver consists of a single op-amp (TL081). The output of this capacitance transducer is given by equation 4.1 [28]. In this equation the output voltage V_O is obtained by relating the feedback capacitance C_F to the unknown capacitance C_X for a transmitter voltage V_E.

$$V_O = -\frac{C_X}{C_F} * V_E \qquad \textbf{4.1}$$

Ideally, C_F should be chosen as small as possible [28]. The resistance feedback R_F is placed in parallel with C_F ensuring that the op-amp will not saturate as a result of DC bias currents charging up C_F. The circuit details are provided in Appendix C on page 140.

4.2.4 Applying Synchronous Detection on the Received Signals

An interesting method that combines accuracy, dynamic range and speed is synchronous detection, also called homodyne or phase-sensitive detection. In this method, as illustrated in figure 4.6 the output is rectified by being inverted during alternate half cycles.

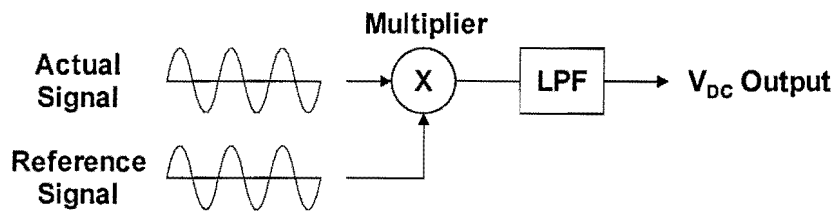

Figure 4.6: Basic principle of synchronous ('homodyne') detection.

The major advantage of using synchronous detection, which periodically inverts the signal (proportional to the change in capacitance or resistance) turning it into DC, is that it does not make use of the polarity of the actual signal (which may be dominated by noise) to determine when the inversion must occur. This obviously requires a clean reference signal, in this case a sine-wave, which is in phase (if an output signal proportional to the change in resistance) or 90^0 out of phase (if an output signal proportional to the change in capacitance) with the signal that needs to be rectified.

As can be seen the inversion of the actual signal will take place at the right time even if it is contaminated with noise. Synchronous detection works well up to frequencies of a few megahertz, at least; [56] the big disadvantage is the need for a coherent reference signal.

The FDM impedance tomography system uses four synchronous detection boards, each performing synchronous detection for one complete channel, where a channel incorporates both the capacitance and resistance signals from a specific receiver, as shown in figure 4.7. Also figure 4.7 on the next page, illustrates the provisions that were made so that the boards could be used for a 16-electrode FDM impedance tomography system as well.

As can be seen from figure 4.7, the two signals received from the receiver board RxA and passed to the synchronous detection board consist of a superposition of components from the different transmitters.

These signals are multiplied, using AD633J analogue multipliers, with a reference signal coherent with the signal applied on the transmitting plate and probe, to extract the resistance of a particular path. A 90^0 phase-shifted version of the same reference signal extracts the capacitance of that path. The signals are then amplified individually by op-amps configured in the inverting mode and having variable gains, optimizing their dynamic range and then are low-pass filtered by 4^{th} order Butterworth filters with cut-off frequencies of 200Hz. The results are dc-signals whose magnitudes are proportional to the capacitance and resistance of the specific path can be obtained.

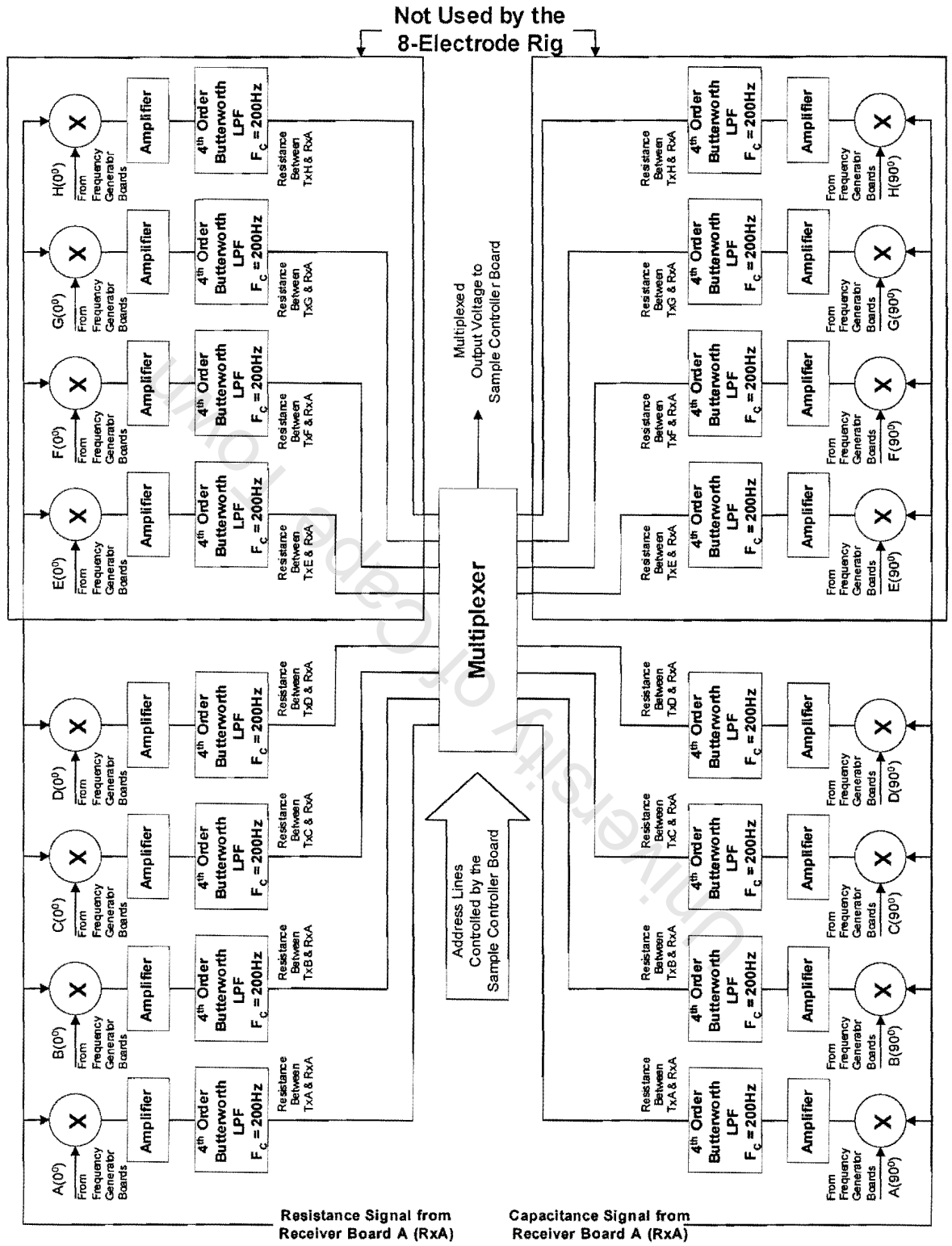

Figure 4.7: Block diagram of the synchronous detector circuit board showing a complete channel.

Multiplexing of the dc-signals was also required as the Eagle PC30G data acquisition card used to capture the output voltages has only 16 analogue input channels and we require that 32 voltages (for the 8-electrode FDM impedance tomography system) or 128 voltages (for a 16-electrode FDM impedance tomography system) should be captured. The multiplexing for the FDM impedance tomography system takes place after the measurements are performed thus isolating the data acquisition process from the transducer systems. Thus, the system does not affect the capacitance or resistance reading, and does not have to wait between each sample for the voltages to stabilize.

A single DG406CJ 16-input CMOS analogue switch (on each synchronous detection board) is used to multiplex the four capacitance and four resistance readings (for the 8-electrode FDM impedance tomography system) or the eight capacitance and eight resistance readings (for a 16-electrode FDM impedance tomography system) for each channel. The address lines of these multiplexers are driven by the sample controller board and each output of the multiplexers is also supplied to the sample controller board.

Tests on the output voltages of the 4^{th} order low-pass filters with cut-off frequencies set at 200Hz showed the absence of unwanted frequency components (small frequency components of 50Hz and 150Hz do exist) and further tests on the outputs of the multipliers showed that unwanted frequencies existed for 1kHz and above. The circuit details of the synchronous detector boards are provided in Appendix C on page 141.

4.2.5 System-Computer Interfacing

The capturing of the system's output voltages (dc-voltages proportional to the capacitance and resistance changes) was done with the use of an Eagle PC30G data acquisition card plugged into the reconstruction computer. This card can provide its user with a sample rate of 100ksamples/s, provided that the data is sampled directly to the memory under the supervision of the Direct Memory Access (DMA) controller. The card also supports 16 analogue input voltages in the range from +10V to -10V, as well as three 8-bit bi-directional digital input-output ports.

The author used the software for accessing the information (dc-voltages) from the PC30G card that was written by Teague [53]. The author also used the sample controller board, which was modified to suite his needs, that was also designed by Teague [53]. The sample controller board was designed for a dual 16-electrode FDM impedance tomography system and it is capable of providing a sample rate of 80ksamples/s.

The reason behind constructing the sample controller board was so that the capturing process could be sped-up. With the use of the sample controller board streaming could be employed, which is similar to single-channel DMA except that it permits unlimited amounts of data to be transferred and therefore high sampling rates can be achieved. In other words, if the sample controller board was omitted from the system-computer interface the address lines of the analogue multiplexers (DG406CJ) would have to be driven by the digital input-output lines provided by the PC30G card through software incorporated in the main software program. Using this, any advantage that would have been gained by using streaming would be negated by the fact that after every 4 samples (or 8 samples for a 16-electrode system or 16 samples for a dual 16-electrode system) the software would have had to increment the address lines of the analogue multiplexers.

With the use of the sample controller board, high sampling rates are obtained as it controls the address lines of the analogue multiplexers externally. Thus, the three digital lines used by the PC30G card (PA0, External Trigger and PA1) are only used to configure the sample controller card before and after a complete data set has been retrieved.

Figure 4.8 on the next page, is a block diagram of the sample controller board and illustrates how this board interfaces with the four synchronous detection boards (or 8 synchronous detection boards for a 16-electrode FDM system or 16 synchronous detection boards for a dual 16-electrode FDM system) and the PC30G card. The circuit details of the sample controller board are provided in Appendix C on page 142.

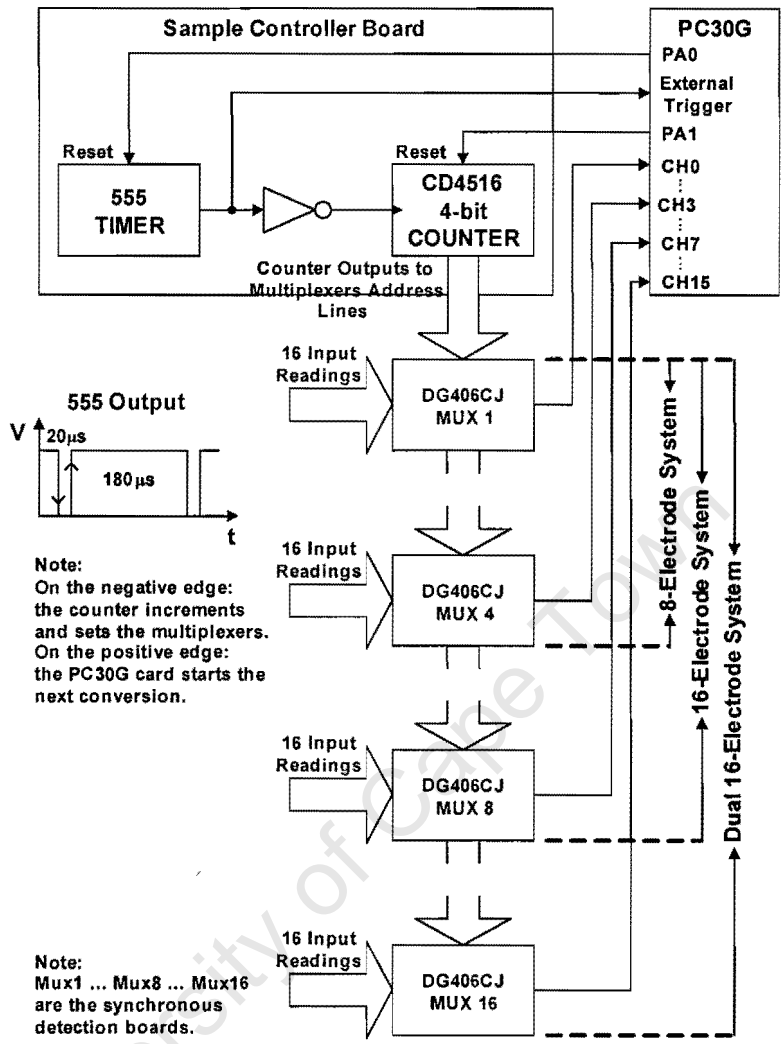

Figure 4.8: Block diagram of the PC30G card interfacing with the sample controller board, and the synchronous detection boards.

CHAPTER 5

5. GENERATING THE TRAINING AND TESTING DATA

This section is intended to show the reader how the training and testing data sets were obtained under static tests, as well as the technique used to vary the dielectric distribution within the area of interest (vessel).

The use of the air-tube and gravel-bubble placement system [3] employed by the author had been designed with the intention that the disturbance of the dielectric distribution created by the placement system within the vessel was varied in a systematic, consistent and structured way. Also, even though the process used to disturbed the electric field within the vessel was achieved manually, a considerable amount of data was able to be collected, so that it could be used later on for the training and testing of the neural network.

As was mentioned in Chapter 2, the training of neural networks requires large quantities of data, something which was not attainable using the manual data collection technique employed by the author. The reason behind using such a process to disturb the electric field within the vessel was that training and testing of the neural network could be done with voltages obtained by the hardware system proportional to the real capacitances and resistances in the vessel, and not with simulated ones (capacitances and resistances) obtained from the use of Finite Element Models [50]. Therefore, even though such a technique would severely limit the attainable amount of training and testing data, problems of having to model the noise and drift of the real system would be eliminated, and the actual capability of the system and the frequency multiplexing technique (FDM), could be shown. Also, the image reconstruction would be more accurate [3].

I would like to mention here that the author used the same air-tube and gravel-bubble placement technique as used by Teague in his Ph.D. study [53] to obtaining data sets for

training and testing of the neural network. This was done to ensure a good and fair comparison between the results obtained from his system and the results obtained by the author's system.

5.1 Air Tube and Gravel Bubble Placement System

This system was designed so that a three phase (air, gravel and seawater) image reconstruction and volume fraction predictions could be done. Polystyrene foam was used to represent air, since its dielectric is very close to that of air. Figure 5.1 illustrates a number of air-tubes used by the author.

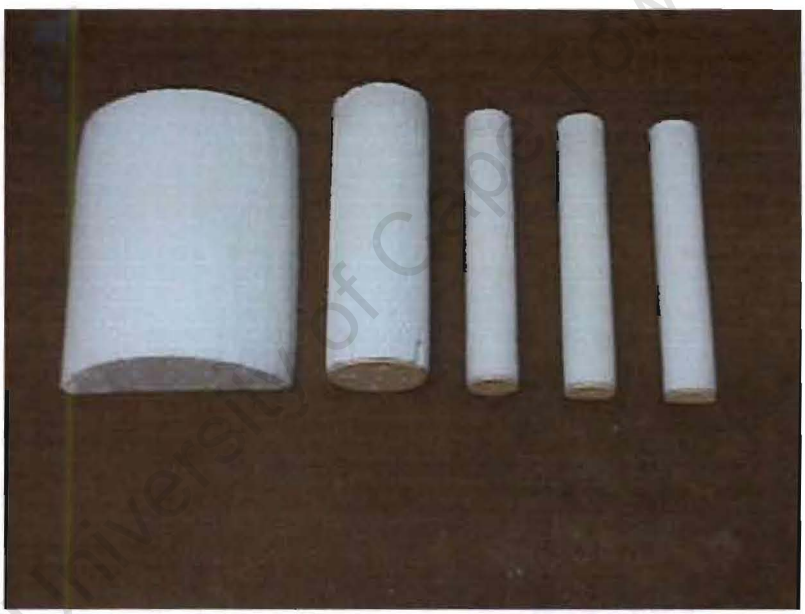

Figure 5.1: Photograph of the different size and shape air-tubes.

Gravel chips placed in nylon stockings were used as gravel-bubbles. The gravel-bubbles that were used were longer than the capacitance plates mounted on the periphery of the vessel. Figure 5.2 on the next page illustrates a number of the gravel-bubbles used by the author. According to Teague [3] the nylon stocking used is unlikely to affect the readings.

The smallest air-tube and gravel-bubble used were 45mm in diameter, ensuring that an image resolution of 20% of the vessel's diameter could be achieved. The largest air-tube

and gravel-bubble used had a diameter of 90mm. A half round air-tube with diameter 220mm was also used.

Figure 5.2: Photograph of the different size and shape gravel bubbles.

Table 5.1 contains the relative dielectric constants of the three phases, as well as the dielectric constant of the polystyrene foam used to simulate air.

PHASES	RELATIVE DIELECTRIC CONSTANT (AT 25^{0}C)
POLYSTYRENE FOAM	1.25
AIR	1.00054
SAND – GRAVEL	3 to 5
WATER	78.54

Table 5.1: Dielectric constants of the materials used.

The vessel used for the study is a PVC pipe with an inside diameter of 220mm, an outside diameter of 250mm, and a height of 300mm.

The air-tube and gravel-bubble placement system consists of a round plate, made of Perspex with a diameter of 220mm. This round plate has 37 steel nails protruding from it,

in the arrangement shown in figure 5.3. This 'bed-of-nails' is placed inside the vessel, positioned flat on the bottom of the vessel. The steel nails act as locators for individual air-tubes. All air-tubes have centre holes on their bottom and top sides to ensure that they are vertically positioned inside the vessel. By positioning a small air-tube on all 37 nails, 37 different positions could be obtained and therefore the entire cross-section of the vessel would be covered.

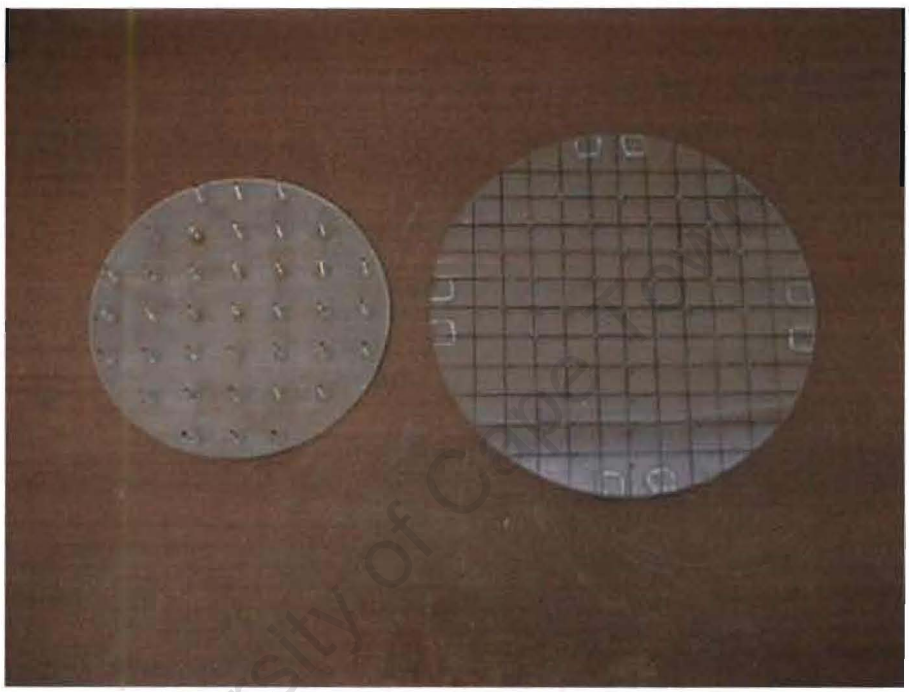

Figure 5.3: Photograph of the 'bed-of-nails' and the lid.

A Perspex lid, shown in figure 5.3, is placed on top of the vessel. The lid has a matrix of lines drawn on it, dividing the vessel cross-section into discrete pixels. The pixel size is such that four pixels can represent a small air-tube and gravel-bubble (see figure 5.4 (a) and 5.4 (c) on the next page) and twelve pixels can represent a big air tube and gravel bubble (see figure 5.4 (b) and 5.4(d) on the next page). These pixels are used to graphically illustrate the desired output required from the neural network for that specific frame of data. Each frame consists of 32 readings.

The Perspex lid also has 37 holes drilled into it in such a way that the holes in the lid and the nails of the 'bed-of-nails' coincide. The operator can ensure that the air-tubes used are

vertically positioned inside the vessel by inserting a nail through the hole of the lid into the top hole of the air-tubes (see figure 5.4 (a), (b)). These can also be used to suspend the gravel-bubbles from the Perspex lid (see figure 5.4(c), (d)).

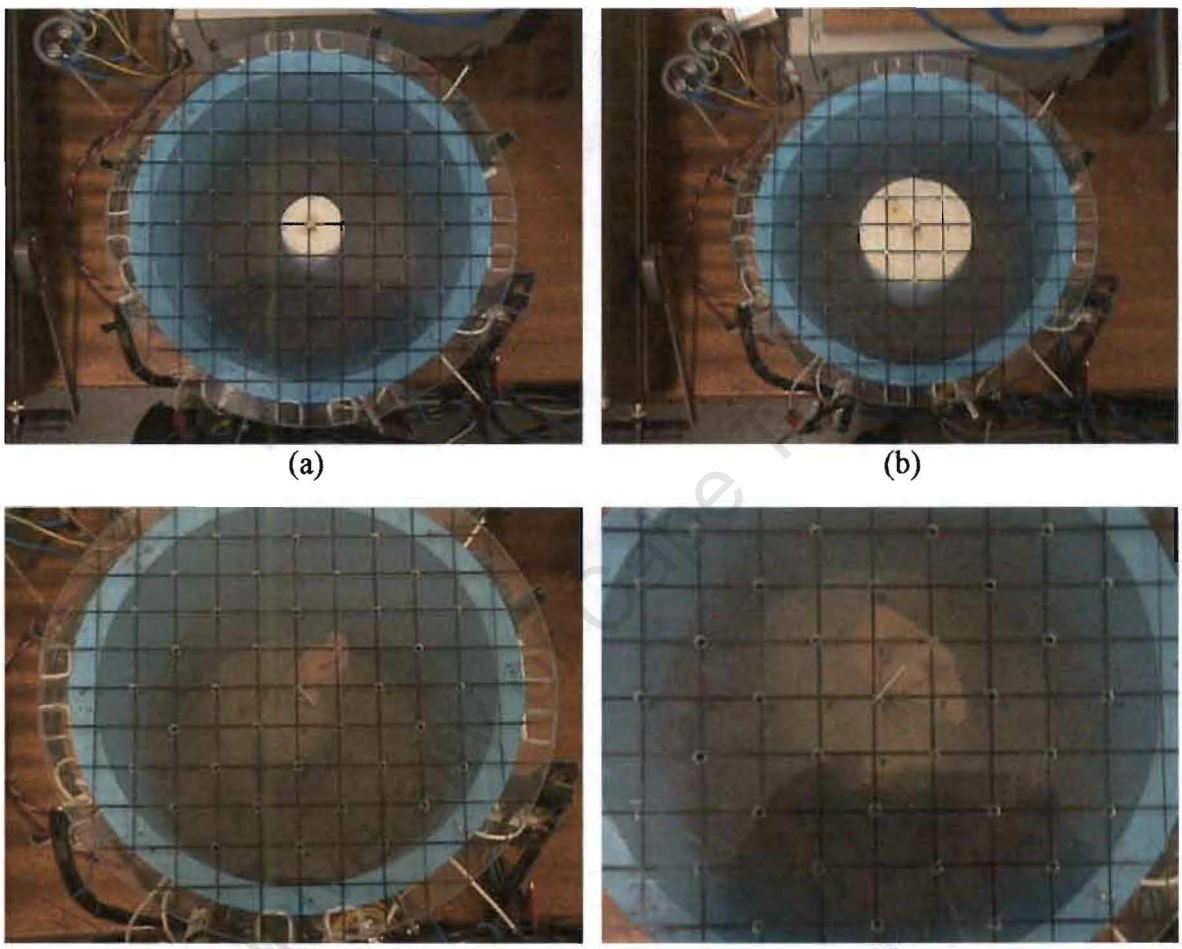

Figure 5.4: Photographs of (a) a small and (b) a big air-tube under investigation, positioned in the centre of the vessel and of (c) a small and (d) a big gravel-bubble under investigation, positioned also in the centre of the vessel.

5.2 Training and Testing Data Generation

The neural network employed by the author used supervised learning. Therefore, both the input and the desired network output needs to be specified. In this application the network inputs are the 32 voltages representing the 32 linearly independent electrode combinations.

Sixteen of those voltages are proportional to the capacitances formed in the vessel and the other sixteen voltages are proportional to the resistances formed in the vessel. The desired network output is a graphical representation of the dielectric distribution within the vessel. This is provided to the neural network by the user via the graphical user interface shown in figure 5.5.

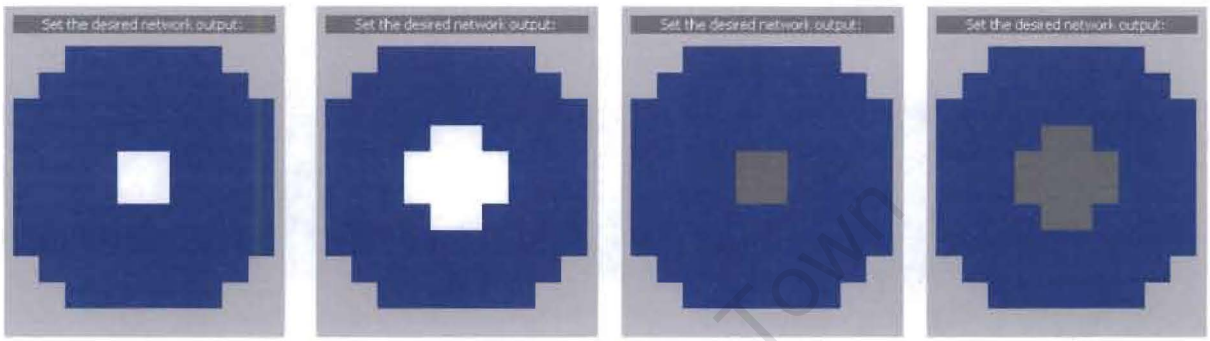

(a) (b) (c) (d)

Figure 5.5: Screen captures of (a) small and (b) big air-tubes, and (c) small and (d) big gravel-bubbles of desired network outputs employing the graphical user interface.

By looking through the Perspex lid from above, the user can identify which pixels are air, gravel and seawater in the vessel and set the corresponding pixel on the graphical user interface. Blue represents seawater, white represents air and grey represents gravel.

For the training of the neural network the author used data collected by placing single air-tubes (both sizes) in seawater, and by placing single gravel-bubbles (both sizes) in seawater. In other words, an element of one phase (air or gravel) was placed in a specific location within the second phase (seawater) and three readings were taken.

ORDER	PHASES IN THE VESSEL DURING TEST	POSITIONS
1	Small Air-Tube and Seawater	37
2	Big Air-Tube and Seawater	17
3	Small Gravel-Bubble and Seawater	25
4	Big Gravel-Bubble and Seawater	17

Table 5.2: Table containing the data used to train the neural network.

The phase (air or gravel) is then moved to another position in the second phase (seawater) and a reading is taken again. This procedure is repeated until most of all the possible combinations of air tube and gravel-bubble positions have been covered. The order in which the data for the training of the neural network was collected is shown in table 5.2 on the previous page.

For the testing of the neural network the author used combinations of air-tubes, combinations of gravel-bubbles and combinations of both air-tubes and gravel-bubbles placed in seawater. Again, three readings were taken for each of the position of the above mentioned combinations. The process was carried on until enough information was collected. The order in which the data for the testing of the neural network was collected is shown in table 5.3.

ORDER	PHASES IN THE VESSEL DURING TEST	POSITIONS
1	Small and/or Big Air-Tubes and Seawater	36
2	Small and/or Big Gravel-Bubbles and Seawater	28
3	Small and/or Big Air-Tubes, Gravel-Bubbles and Seawater	64

Table 5.3: Table containing the data used to test the neural network.

As can be seen from the above, the data used for testing the neural network did not form part of the data used to train it. The reason for using such testing data was so that the generalization performance of the neural network could be tested i.e. the ability of the system to generalize for previously unseen data. Also, more realistic results could be obtained by trying to see if the neural network could generalize from single air-tubes or gravel-bubbles from one phase used in the training data, to combinations of air-tubes and gravel-bubbles of different phases.

The generalization ability of the neural network is assessed by using the following two measures. The first one is called the threshold error, which is a percentage value depicting the percentage of the pixels which are not predicted correctly. This measure is used so that

a comparison between the desired network output and the network prediction could be provided.

The other measure is called volume fraction error. Specifically three volume fractions are provided by the system: one for air, one for gravel and one for seawater. The volume fraction error is the percentage error of the volume fraction prediction for each of the three phases. This measure is independent of pixel position.

CHAPTER 6

6. EXPERIMENTAL RESULTS

This chapter is intended to show the reader how the electric impedance tomography (EIT) system under investigation responded to disturbances in the electric field (formed by the system in the testing vessel). These disturbances were created by placing tubes and bubbles of various sizes and materials within the vessel. These artificial disturbances simulate the propagation of air and gravel respectively through the medium contained in the vessel (seawater).

It is necessary that that the reader has a good understanding of the system's response to variation of the dielectric distribution within the vessel, before he/she can appreciate the performance of the neural network in reconstruction of the cross-sectional view of the rig, as well as its performance in predicting the volume fractions.

The following section contains a small, but very carefully chosen representative sample of the results obtained. This data sample was retrieved by the training database that was used to train the neural network. Each page consists of a picture illustrating the required neural network output, a table containing 32 values depicting the electric field disturbance in volts, and two graphs indicating the values that were stored in the training database.

The picture shows the air-tube or gravel-bubble that was used to disturb the electric field within the vessel, as well as its position in the rig. As was already mentioned, three colours are used to indicate the materials (three phases) inside the rig. Blue represents seawater, white air, and grey gravel. Relevant size information is represented as follows: four pixels indicate a small air-tube or gravel-bubble (diameter of 45mm) and twelve pixels indicating a large air-tube or gravel-bubble. The small air-tube and gravel-bubble ensure that an image resolution of 20% of the vessel's diameter can be achieved and the big ones an image resolution of 40%.

The table contains 32 values depicting the electric field disturbance in volts. These values give an indication of the relative magnitude of the disturbance caused by the insertion of the various objects between specific transmitter and receiver combinations. They are the results of subtracting the values that were recorded when the air tube or gravel bubble depicted in the picture of the page was positioned in the rig from the values that were recorded by the EIT system when there was nothing but seawater in the vessel. Each value in the table is an average value of 75 values of the above subtractions.

It was noted that even though the readings should decrease as air and gravel have lower permittivity and higher resistivity that seawater, some of them were increased. This phenomenon is explained as follows. According to Xie et al [15], in capacitance tomography the electrical flux lines within the vessel (rig) will be redistributed by the introduction of a different phase into the vessel. Hence, more electric flux lines will be absorbed by certain electrodes, resulting in over-shooting effects. Also, according to Hervieu and Seleghim [55], in resistance tomography the introduction of a non-conducting object (phase) in the region of an electrode results in a current deficiency at that particular electrode and a current excess at its neighbour electrodes. For large non-conductive electrodes this current deficiency extends to multiple electrodes.

The two graphs on the bottom of the page display the dc-voltages proportional to the capacitance ($CAP._w$) and resistance ($RES._w$), for a specific transmitter-receiver pair that were obtained when the vessel contained only seawater, as well as the capacitance ($CAP._{a-w}$ or $CAP._{g-w}$) and resistance ($RES._{a-w}$ or $RES._{g-w}$), for a specific transmitter-receiver pair that were obtained when the vessel contained air and seawater or gravel and seawater. The two graphs are representations of the values that were stored in the training database, so that they could be used later on for the training of the neural network.

The training database is divided into 4 sections, each section containing the data recorded when tubes of differing types were placed within the medium of the vessel at various positions. The tube types for each section are as follows:

1. Small diameter air-tube.

2. Small diameter gravel-bubble.
3. Large diameter air-tube.
4. Large diameter gravel-bubble.

The testing database is not dealt with here, as it contains combinations of the single tubes and/or bubbles (see Chapter 7) used to create the training database.

Three types of test are shown in this chapter. These tests illustrate the results that were obtained by placing single small or big air-tubes or gravel-bubbles directly in front or close to the transmitters TxA and TxD and the receivers RxA and RxD, as well as the centre of the rig. Transmitter TxA transmits the lowest sinusoidal frequency (24.375kHz) of the system and transmitter TxD transmits the highest sinusoidal frequency (46.875kHz).

In the following results the reader will be able to see that the system performs well along the periphery of the vessel, but very poorly as the two phases under investigation (air and gravel) move away for the periphery wall and towards the centre of the vessel.

6.1 Capacitance and Resistance Values Measured by the System

Section 1 - Disturbance Source: small air-tube in front of transmitter TxD.

1. Results

		Receivers							
		Electric Field Disturbance (V)							
		RxA		RxB		RxC		RxD	
		Cap.	Res.	Cap.	Res.	Cap.	Res.	Cap.	Res.
Transmitters	TxA	-0.03581	-0.04883	-0.03662	-0.04231	-0.01953	-0.00247	-0.03662	-0.04639
	TxB	-0.06104	-0.05941	-0.06348	-0.05941	-0.05696	-0.06592	-0.05534	-0.05371
	TxC	-0.0651	-0.06999	-0.07812	-0.07406	-0.09522	-0.10416	-0.04964	-0.04557
	TxD	0.57536	0.520013	0.601397	0.552573	0.56559	0.621747	0.459797	0.465493

(b)

(a)

Figure 6.1: (a) The neural network desired output for the electric field disturbance (in volts) shown in the table above. (b) Table containing 32 numbers showing the electric field disturbance (in volts) that was caused by the insertion of the small air-tube in the vessel in the position illustrated in figure 6.1 (a).

2. Description

The capacitive and resistive transducers accurately detect the disturbance caused by inserting the small air-tube in front of transmitter TxD.

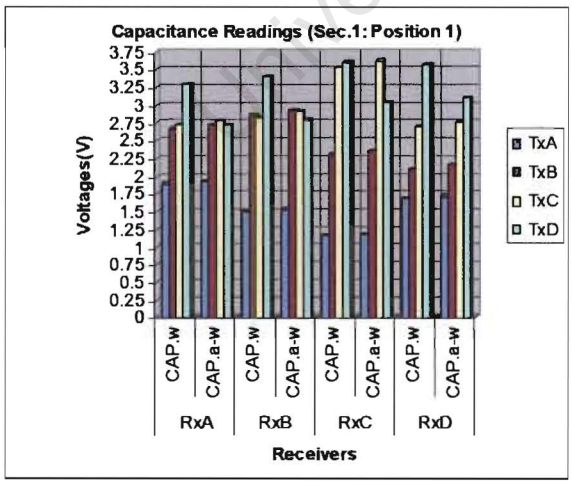

(a)

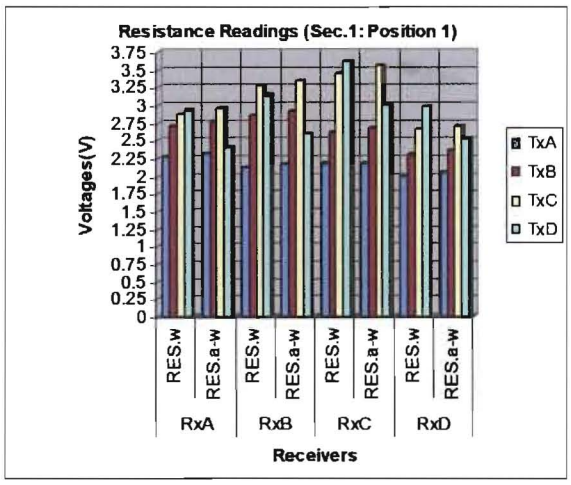

(b)

Figure 6.2: DC voltages proportional to (a) the capacitance and (b) the resistance detected by the system. These values represent figure 6.1 (a) and were used for training the neural network.

Section 1 - Disturbance Source: small air-tube in front of transmitter TxA.

1. Results

		Receivers							
		Electric Field Disturbance (V)							
		RxA		RxB		RxC		RxD	
		Cap.	Res.	Cap.	Res.	Cap.	Res.	Cap.	Res.
Transmitters	TxA	0.197434	0.307463	0.207859	0.325001	0.210322	0.349482	0.208537	0.315073
	TxB	-0.04962	-0.03719	-0.03784	-0.04203	-0.03178	-0.02514	-0.0123	0.001337
	TxC	-0.01752	-0.00983	-0.02	-0.02274	-0.02066	-0.00829	-0.01503	-0.0045
	TxD	-0.0479	-0.03145	-0.07401	-0.07284	-0.07223	-0.06165	-0.08848	-0.06192

(b)

(a)

Figure 6.3: (a) The neural network desired output for the electric field disturbance (in volts) shown in the table above. (b) Table containing 32 numbers showing the electric field disturbance (in volts) that was caused by the insertion of the small air-tube in the vessel in the position illustrated in figure 6.3 (a).

2. Description

The capacitive and resistive transducers detect a smaller disturbance than the one caused by the air-tube in front of TxD, but equally well.

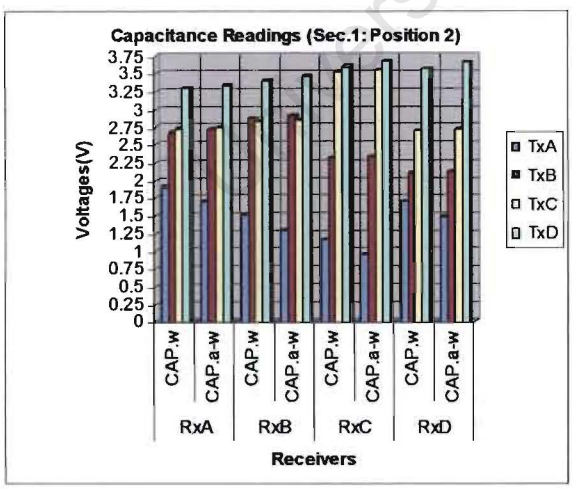

(a)

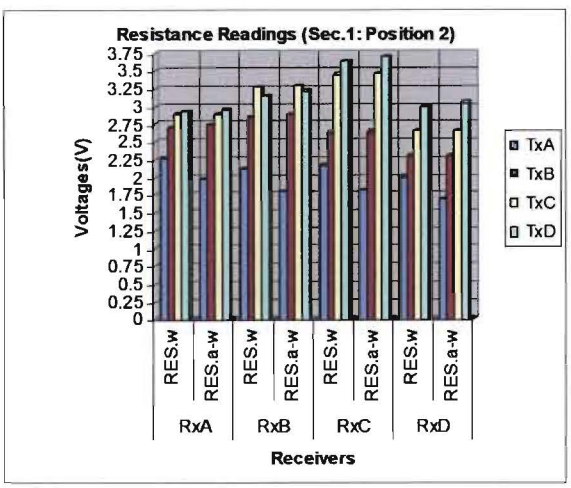

(b)

Figure 6.4: DC voltages proportional to (a) the capacitance and (b) the resistance detected by the system. These values represent figure 6.3 (a) and were used for training the neural network.

Section 1 - Disturbance Source: small air-tube in front of receiver RxD.

1. Results

		Receivers							
		Electric Field Disturbance (V)							
		RxA		RxB		RxC		RxD	
		Cap.	Res.	Cap.	Res.	Cap.	Res.	Cap.	Res.
Transmitters	TxA	-0.03658	-0.0724	-0.0333	-0.06201	-0.02667	-0.04702	0.001018	0.320501
	TxB	-0.0715	-0.08421	-0.06714	-0.09049	-0.06452	-0.07279	0.01175	0.394852
	TxC	-0.07783	-0.09229	-0.08213	-0.10801	-0.08622	-0.096	0.09474	0.461717
	TxD	-0.08081	-0.07829	-0.09092	-0.09969	-0.10803	-0.1064	-0.02247	0.497706

(b)

(a)

Figure 6.5: (a) The neural network desired output for the electric field disturbance (in volts) shown in the table above. (b) Table containing 32 numbers showing the electric field disturbance (in volts) that was caused by the insertion of the small air-tube in the vessel in the position illustrated in figure 6.5 (a).

2. Description

The capacitive transducer RxD detects a smaller disturbance in comparison to that detected by the resistive transducers RxD.

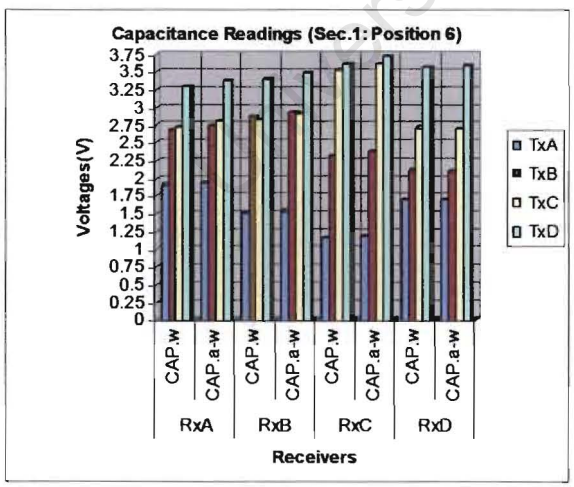

(a)

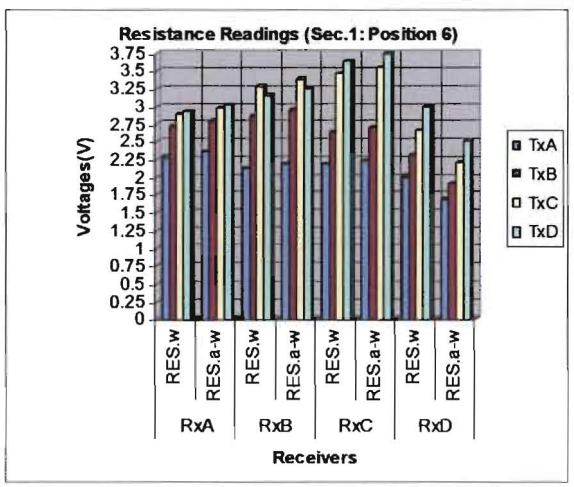

(b)

Figure 6.6: DC voltages proportional to (a) the capacitance and (b) the resistance detected by the system. These values represent figure 6.5 (a) and were used for training the neural network.

Section 1 - Disturbance Source: small air-tube in front of receiver RxA.

1. Results

		Receivers							
		Electric Field Disturbance (V)							
		RxA		RxB		RxC		RxD	
		Cap.	Res.	Cap.	Res.	Cap.	Res.	Cap.	Res.
Transmitters	TxA	0.010485	0.256708	-0.016	-0.03753	-0.01989	-0.04105	-0.02279	-0.05751
	TxB	0.001804	0.328324	-0.06836	-0.09042	-0.05163	-0.06601	-0.03491	-0.06257
	TxC	0.030745	0.380314	-0.06565	-0.09486	-0.06357	-0.07776	-0.05841	-0.08156
	TxD	0.039154	0.406806	-0.07207	-0.08626	-0.07405	-0.0765	-0.06899	-0.08436

(b)

(a)

Figure 6.7: (a) The neural network desired output for the electric field disturbance (in volts) shown in the table above. (b) Table containing 32 numbers showing the electric field disturbance (in volts) that was caused by the insertion of the small air-tube in the vessel in the position illustrated in figure 6.7 (a).

2. Description

The capacitive transducer RxA detects a smaller disturbance in comparison to that detected by the resistive transducers RxA.

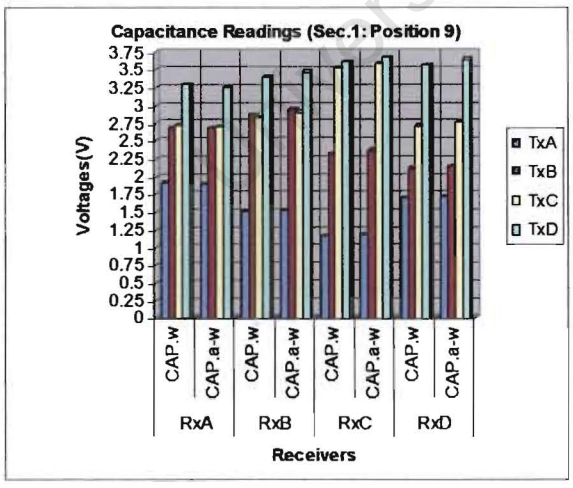

(a)

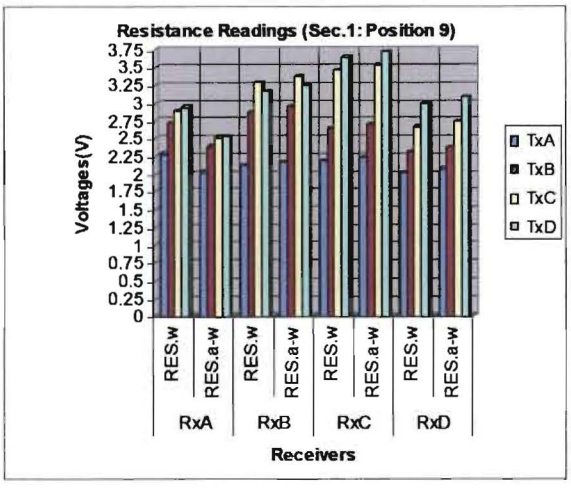

(b)

Figure 6.8: DC voltages proportional to (a) the capacitance and (b) the resistance detected by the system. These values represent figure 6.7 (a) and were used for training the neural network.

Section 1 - Disturbance Source: small air-tube close to transmitter TxD.

1. Results

		Receivers							
		Electric Field Disturbance (V)							
		RxA		RxB		RxC		RxD	
		Cap.	Res.	Cap.	Res.	Cap.	Res.	Cap.	Res.
Transmitters	TxA	0.003887	0.002353	0.007053	0.0145	0.021251	0.026132	0.001626	-0.00434
	TxB	-0.02079	-0.02288	-0.02604	-0.03274	0.004163	-0.00344	0.000991	-0.01121
	TxC	-0.00687	-0.00678	-0.0255	-0.03346	-0.02541	-0.03183	0.015828	0.011032
	TxD	0.048195	0.049459	0.05443	0.045571	0.000001	0.008138	-0.00859	-0.00597

(b)

(a)

Figure 6.9: (a) The neural network desired output for the electric field disturbance (in volts) shown in the table above. (b) Table containing 32 numbers showing the electric field disturbance (in volts) that was caused by the insertion of the small air-tube in the vessel in the position illustrated in figure 6.9 (a).

2. Description

The disturbance detected by the system's capacitance and resistance transducers is noticeably smaller in comparison to the one where the air-tube was positioned in front of TxD even though the air-tube was moved only 45mm away from the periphery wall.

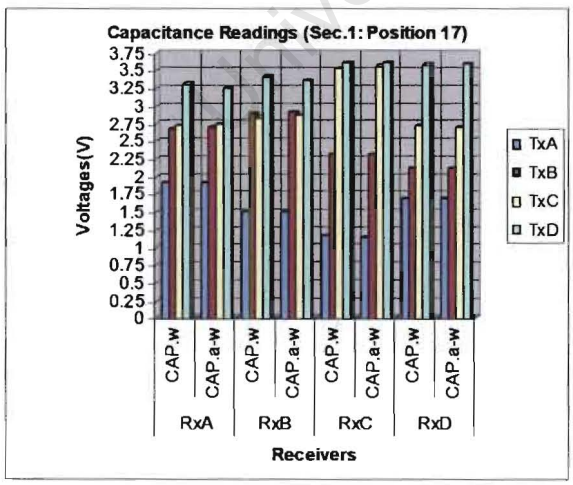

(a)

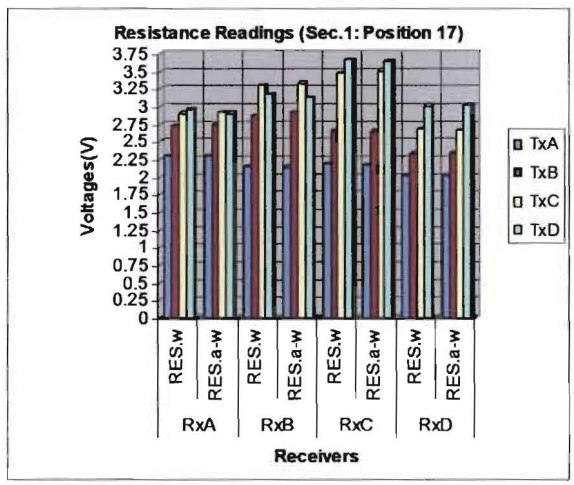

(b)

Figure 6.10: DC voltages proportional to (a) the capacitance and (b) the resistance detected by the system. These values represent figure 6.9 (a) and were used for training the neural network.

Section 1 - Disturbance Source: small air-tube in the centre of the rig.

1. Results

		Receivers							
		Electric Field Disturbance (V)							
		RxA		RxB		RxC		RxD	
		Cap.	Res.	Cap.	Res.	Cap.	Res.	Cap.	Res.
Transmitters	TxA	-0.00213	-0.01896	0.009019	0.000927	0.013477	0.003708	-0.00142	-0.02781
	TxB	-0.01833	-0.03077	-0.0175	-0.03732	0.012251	0.003979	0.013925	-0.0172
	TxC	0.025251	0.018375	-0.00482	-0.02202	-0.00294	-0.0092	0.031721	0.002464
	TxD	0.030405	0.020457	0.032509	0.018309	-0.00468	-0.00061	-0.00348	-0.02557

(b)

(a)

Figure 6.11: (a) The neural network desired output for the electric field disturbance (in volts) shown in the table above. (b) Table containing 32 numbers showing the electric field disturbance (in volts) that was caused by the insertion of the small air-tube in the vessel in the position illustrated in figure 6.11 (a).

2. Description

The disturbance detected by the system's capacitance and resistance transducers is very small but still sufficient for the system to detect.

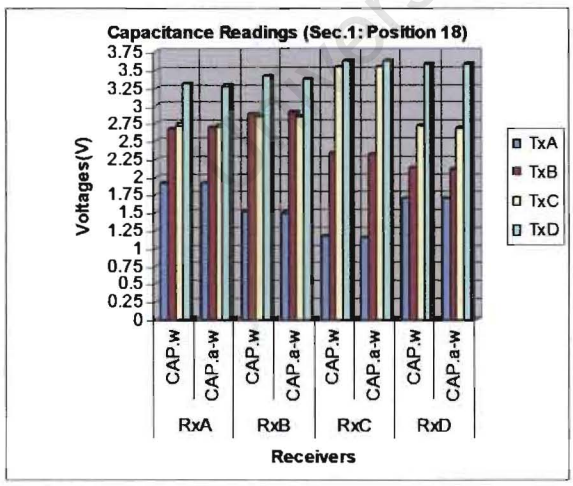

(a)

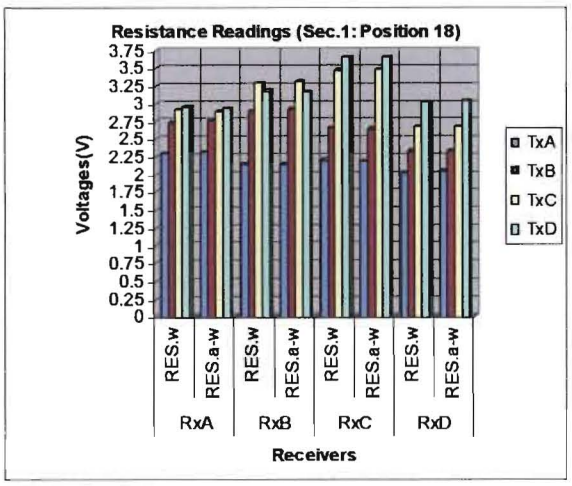

(b)

Figure 6.12: DC voltages proportional to (a) the capacitance and (b) the resistance detected by the system. These values represent figure 6.11 (a) and were used for training the neural network.

Section 1 - Disturbance Source: small air-tube close to transmitter TxA.

1. Results

		Receivers							
		Electric Field Disturbance (V)							
		RxA		RxB		RxC		RxD	
		Cap.	Res.	Cap.	Res.	Cap.	Res.	Cap.	Res.
Transmitters	TxA	0.001352	-0.0217	0.021157	0.014374	0.020076	0.018443	-0.00488	-0.01546
	TxB	-0.01411	-0.02659	-0.00651	-0.02387	0.011124	-0.00516	0.023056	0.011662
	TxC	0.005154	-0.00488	-0.01383	-0.02739	-0.00922	-0.03065	0.009493	-0.00461
	TxD	0.053166	0.044488	0.029566	0.021153	0.009769	0.004883	0.002984	-0.00651

(b)

(a)

Figure 6.13: (a) The neural network desired output for the electric field disturbance (in volts) shown in the table above. (b) Table containing 32 numbers showing the electric field disturbance (in volts) that was caused by the insertion of the small air-tube in the vessel in the position illustrated in figure 6.13 (a).

2. Description

The disturbance detected by the system's capacitance and resistance transducers is noticeably smaller in comparison to the one where the air-tube was positioned in front of TxA even though the air-tube was moved only 45mm away from the periphery wall.

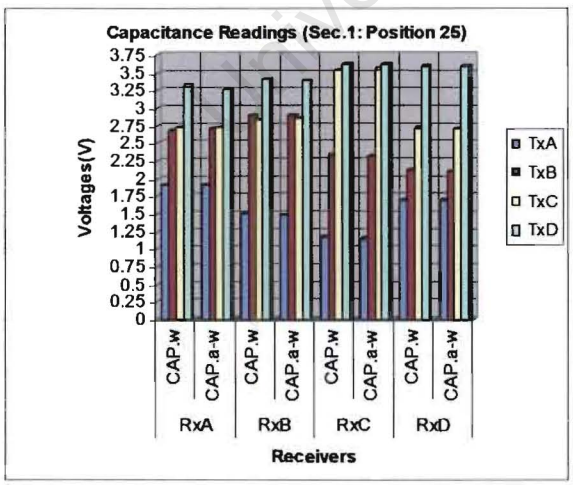

(a)

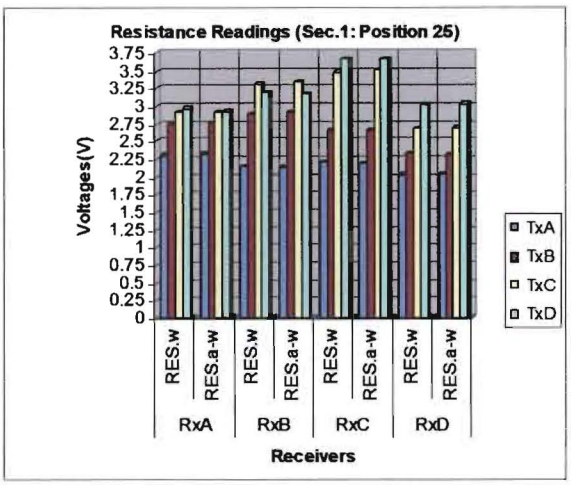

(b)

Figure 6.14: DC voltages proportional to (a) the capacitance and (b) the resistance detected by the system. These values represent figure 6.13 (a) and were used for training the neural network.

Section 2 - Disturbance Source: small gravel-bubble in front of transmitter TxD.

1. Results

		Receivers							
		Electric Field Disturbance (V)							
		RxA		RxB		RxC		RxD	
		Cap.	Res.	Cap.	Res.	Cap.	Res.	Cap.	Res.
Transmitters	TxA	-0.01953	-0.0293	-0.01872	-0.02523	-0.00895	-0.02034	-0.02848	-0.03093
	TxB	-0.04642	-0.03662	-0.04883	-0.04801	-0.04395	-0.04476	-0.04802	-0.02929
	TxC	-0.05941	-0.05615	-0.06592	-0.06755	-0.08056	-0.08464	-0.04313	-0.03011
	TxD	0.387367	0.33203	0.402833	0.34668	0.365393	0.362143	0.309247	0.288903

(b)

(a)

Figure 6.15: (a) The neural network desired output for the electric field disturbance (in volts) shown in the table above. (b) Table containing 32 numbers showing the electric field disturbance (in volts) that was caused by the insertion of the small gravel-bubble in the vessel in the position illustrated in figure 6.15 (a).

2. Description

The capacitive and resistive transducers detect a smaller disturbance than the one caused by the small air-tube in front of TxD, but still a noticeable one. This difference should also help the neural network to distinguish between air and gravel in this specific position.

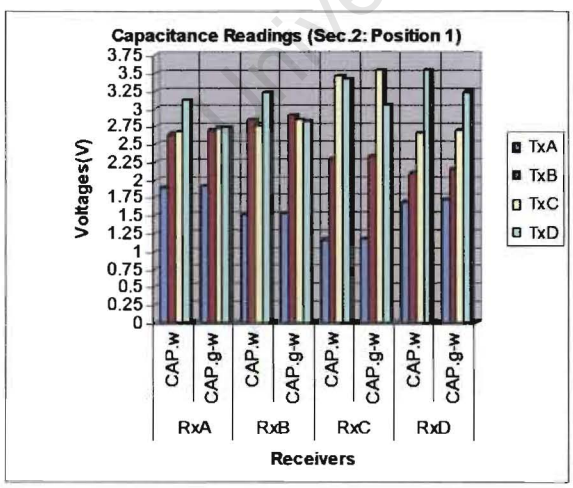

(a)

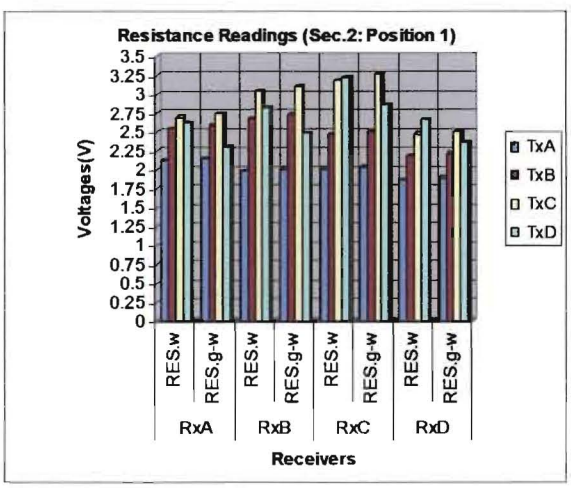

(b)

Figure 6.16: DC voltages proportional to (a) the capacitance and (b) the resistance detected by the system. These values represent figure 6.15 (a) and were used for training the neural network.

Section 2 - Disturbance Source: small gravel-bubble close to transmitter TxD.

1. Results

		Receivers							
		Electric Field Disturbance (V)							
		RxA		RxB		RxC		RxD	
		Cap.	Res.	Cap.	Res.	Cap.	Res.	Cap.	Res.
Transmitters	TxA	-0.00522	-0.01743	-0.00048	-0.00312	0.005975	0.00295	-0.0096	-0.01763
	TxB	-0.02	-0.02398	-0.01841	-0.02011	-0.00282	-0.01428	-0.00852	-0.006
	TxC	-0.00841	-0.01245	-0.01506	-0.02102	-0.01828	-0.02957	0.013498	0.009523
	TxD	0.028885	0.020616	0.030515	0.020548	-0.01193	-0.01963	-0.00953	-0.01146

(b)

(a)

Figure 6.17: (a) The neural network desired output for the electric field disturbance (in volts) shown in the table above. (b) Table containing 32 numbers showing the electric field disturbance (in volts) that was caused by the insertion of the small gravel-bubble in the vessel in the position illustrated in figure 6.17 (a).

2. Description

The disturbance detected by the system is noticeably smaller to the one where the small gravel-bubble was positioned in front of TxD. Furthermore, the values in the above table are very similar to the ones for the case of the small air-tube placed at the same position.

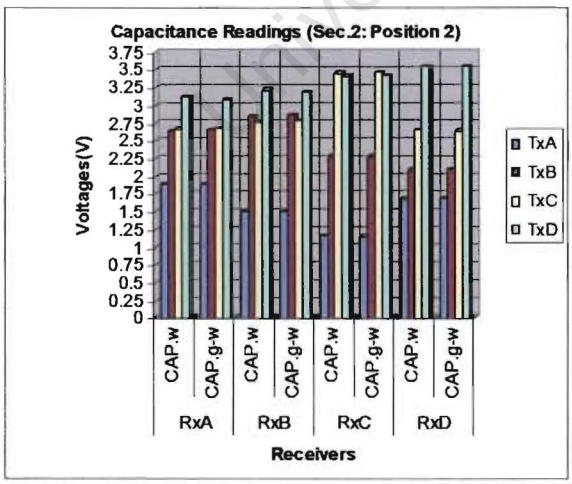

(a)

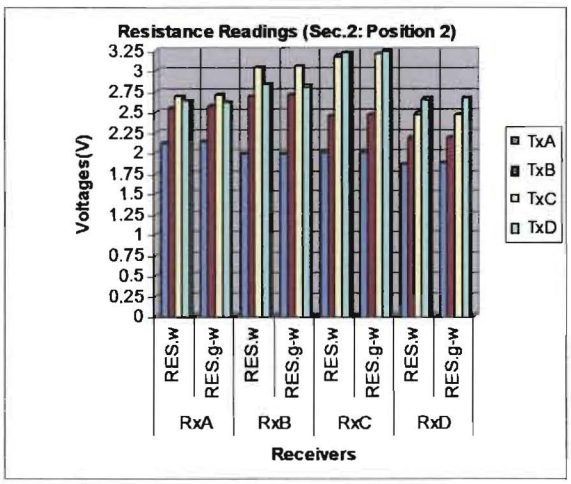

(b)

Figure 6.18: DC voltages proportional to (a) the capacitance and (b) the resistance detected by the system. These values represent figure 6.17 (a) and were used for training the neural network.

Section 2 - Disturbance Source: small gravel-bubble in the centre of the rig.

1. Results

		Receivers							
		Electric Field Disturbance (V)							
		RxA		RxB		RxC		RxD	
		Cap.	Res.	Cap.	Res.	Cap.	Res.	Cap.	Res.
Transmitters	TxA	-0.00963	-0.01858	0.004746	0.00434	0.002986	-0.00223	-0.01268	-0.01654
	TxB	-0.02373	-0.03004	-0.02299	-0.02882	-0.00319	-0.00984	-0.00156	-0.00549
	TxC	0.006778	0.001966	-0.0179	-0.02089	-0.01702	-0.02415	0.007465	-0.00211
	TxD	0.011389	0.010306	0.015459	0.008542	-0.00841	-0.01566	-0.01336	-0.01316

(b)

(a)

Figure 6.19: (a) The neural network desired output for the electric field disturbance (in volts) shown in the table above. (b) Table containing 32 numbers showing the electric field disturbance (in volts) that was caused by the insertion of the small gravel-bubble in the vessel in the position illustrated in figure 6.19 (a).

2. Description

The disturbance detected by the system's transducers is very small but still sufficient for the system to detect. The values in the above table are very close to the ones collected by the system when the small air-tube was placed in the middle of the rig.

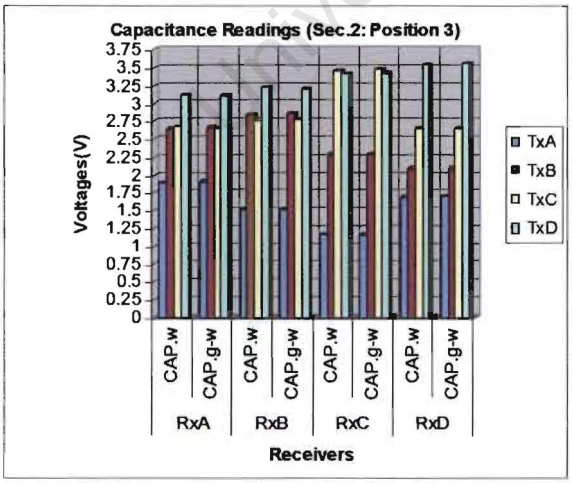

(a)

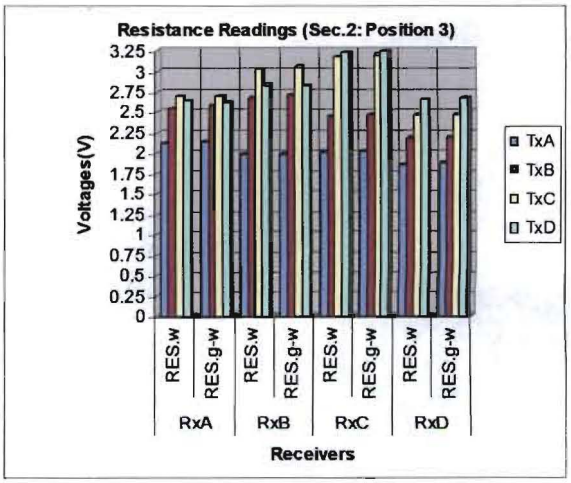

(b)

Figure 6.20: DC voltages proportional to (a) the capacitance and (b) the resistance detected by the system. These values represent figure 6.19 (a) and were used for training the neural network.

Section 2 - Disturbance Source: small gravel-bubble close to receiver RxD.

1. Results

		Receivers							
		Electric Field Disturbance (V)							
		RxA		RxB		RxC		RxD	
		Cap.	Res.	Cap.	Res.	Cap.	Res.	Cap.	Res.
Transmitters	TxA	-0.00468	-0.01933	0.006304	0.002033	0.013024	0.006207	0.000712	0.008137
	TxB	-0.03276	-0.04242	-0.02574	-0.03856	-0.01801	-0.03571	0.00315	0.022481
	TxC	-0.04232	-0.06236	-0.04924	-0.07528	-0.053	-0.08219	-0.01038	-0.00539
	TxD	0.019126	0.000808	-0.0004	-0.00793	-0.02197	-0.03754	-0.0117	-0.00956

(b)

(a)

Figure 6.21: (a) The neural network desired output for the electric field disturbance (in volts) shown in the table above. (b) Table containing 32 numbers showing the electric field disturbance (in volts) that was caused by the insertion of the small gravel-bubble in the vessel in the position illustrated in figure 6.21 (a).

2. Description

The disturbance detected by the system's capacitance and resistance transducers is very small even though the gravel-bubble is only 22mm away from the periphery wall.

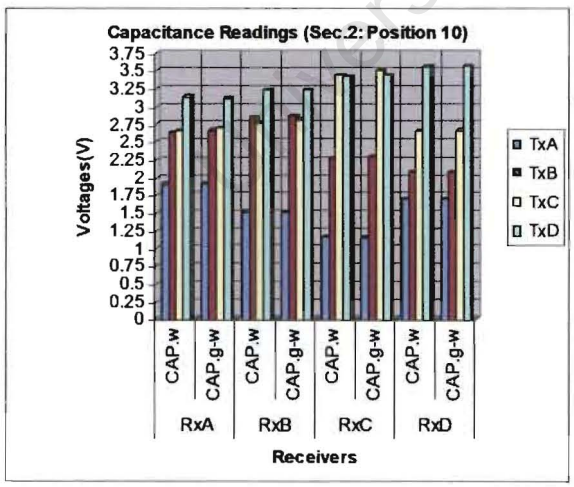

(a)

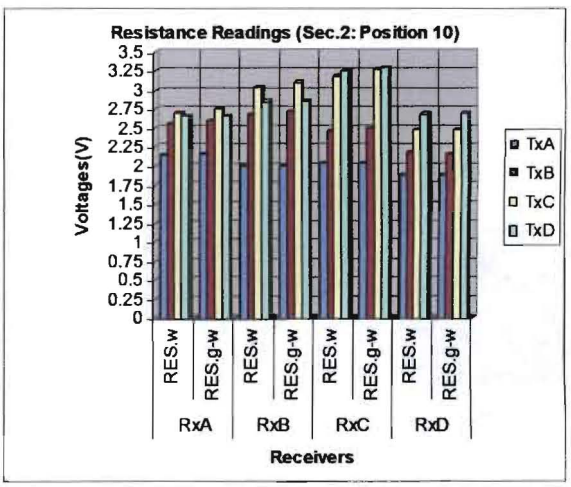

(b)

Figure 6.22: DC voltages proportional to (a) the capacitance and (b) the resistance detected by the system. These values represent figure 6.21 (a) and were used for training the neural network.

Section 2 - Disturbance Source: small gravel-bubble close to transmitter TxA.

1. Results

		Receivers							
		Electric Field Disturbance (V)							
		RxA		RxB		RxC		RxD	
		Cap.	Res.	Cap.	Res.	Cap.	Res.	Cap.	Res.
Transmitters	TxA	0.003933	-0.01234	0.017224	0.018447	0.016552	0.0116	-0.00482	-0.00868
	TxB	-0.03405	-0.04035	-0.02624	-0.03832	-0.01675	-0.0272	-0.00129	0.006719
	TxC	-0.03364	-0.04957	-0.05371	-0.07596	-0.05419	-0.07514	-0.03268	-0.039
	TxD	0.025227	0.008408	0.002443	-0.01343	-0.00868	-0.02299	-0.01309	-0.00963

(b)

(a)

Figure 6.23: (a) The neural network desired output for the electric field disturbance (in volts) shown in the table above. (b) Table containing 32 numbers showing the electric field disturbance (in volts) that was caused by the insertion of the small gravel-bubble in the vessel in the position illustrated in figure 6.23 (a).

2. Description

The detected disturbance is noticeably smaller than the one where the small gravel-bubble is positioned in front of TxA (see position 25). Furthermore, the values in the above table are very similar to those for the case of the small air-tube placed at the same position.

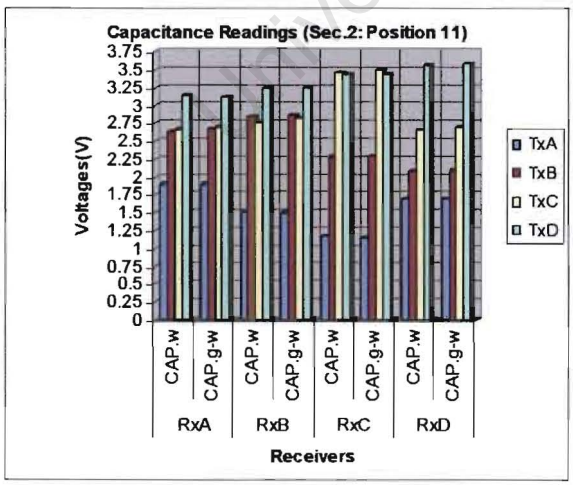

(a)

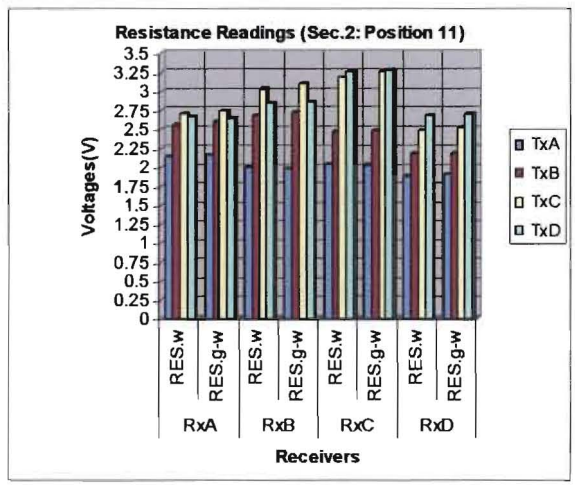

(b)

Figure 6.24: DC voltages proportional to (a) the capacitance and (b) the resistance detected by the system. These values represent figure 6.23 (a) and were used for training the neural network.

Section 2 - Disturbance Source: small gravel-bubble close to receiver RxA.

1. Results

		Receivers							
		Electric Field Disturbance (V)							
		RxA		RxB		RxC		RxD	
		Cap.	Res.	Cap.	Res.	Cap.	Res.	Cap.	Res.
Transmitters	TxA	0.003595	0.107761	0.00454	-0.00176	-0.00434	-0.01801	-0.01685	-0.0198
	TxB	-0.02963	0.115526	-0.05443	-0.07388	-0.03747	-0.05287	-0.02201	-0.01882
	TxC	-0.02903	0.12597	-0.08179	-0.10593	-0.08304	-0.1104	-0.0672	-0.0726
	TxD	0.007732	0.506067	-0.04028	-0.04496	-0.04015	-0.0589	-0.04052	-0.04143

(b)

(a)

Figure 6.25: (a) The neural network desired output for the electric field disturbance (in volts) shown in the table above. (b) Table containing 32 numbers showing the electric field disturbance (in volts) that was caused by the insertion of the small gravel-bubble in the vessel in the position illustrated in figure 6.25 (a).

2. Description

The disturbance detected by the system's capacitance and resistance transducers is very small even though the gravel-bubble is only 22mm away from the periphery wall.

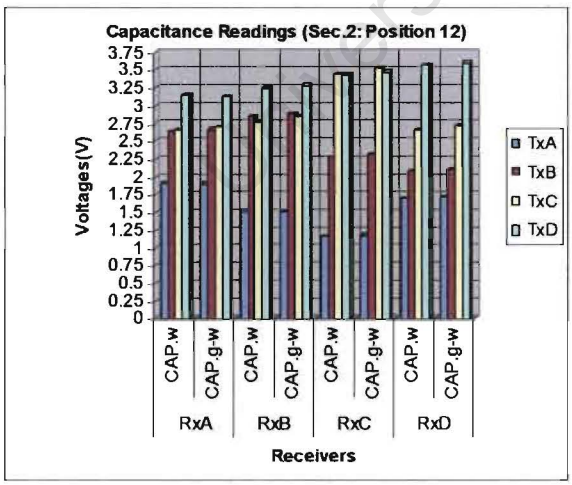

(a)

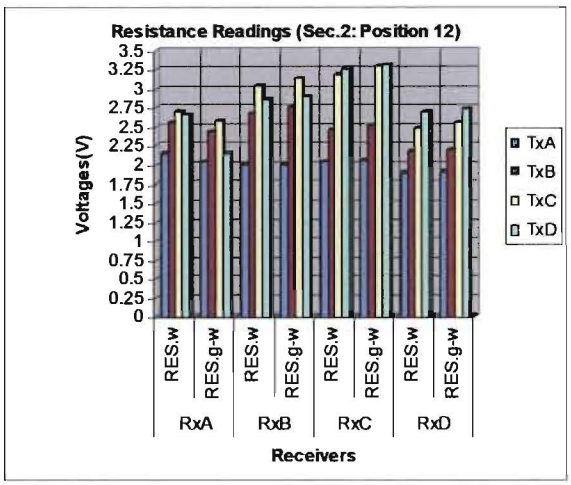

(b)

Figure 6.26: DC voltages proportional to (a) the capacitance and (b) the resistance detected by the system. These values represent figure 6.25 (a) and were used for training the neural network.

Section 2 - Disturbance Source: small gravel-bubble in front of transmitter TxA.

1. Results

		Receivers							
		Electric Field Disturbance (V)							
		RxA		RxB		RxC		RxD	
		Cap.	Res.	Cap.	Res.	Cap.	Res.	Cap.	Res.
Transmitters	TxA	0.149873	0.207656	0.153673	0.21186	0.154351	0.213827	0.134208	0.177408
	TxB	-0.05548	-0.063	-0.04374	-0.06504	-0.03533	-0.05419	-0.01987	-0.01668
	TxC	-0.06971	-0.08633	-0.08301	-0.11366	-0.08334	-0.11366	-0.06741	-0.07446
	TxD	-0.00326	-0.01004	-0.02523	-0.03947	-0.02957	-0.04618	-0.03737	-0.0415

(b)

(a)

Figure 6.27: (a) The neural network desired output for the electric field disturbance (in volts) shown in the table above. (b) Table containing 32 numbers showing the electric field disturbance (in volts) that was caused by the insertion of the small gravel-bubble in the vessel in the position illustrated in figure 6.27 (a).

2. Description

The transducers detect a smaller disturbance (than the one caused by the small gravel-bubble in front of TxD) but still a noticeable one. There is also a distinguishable difference between the air values and gravel values collected by the system at this position.

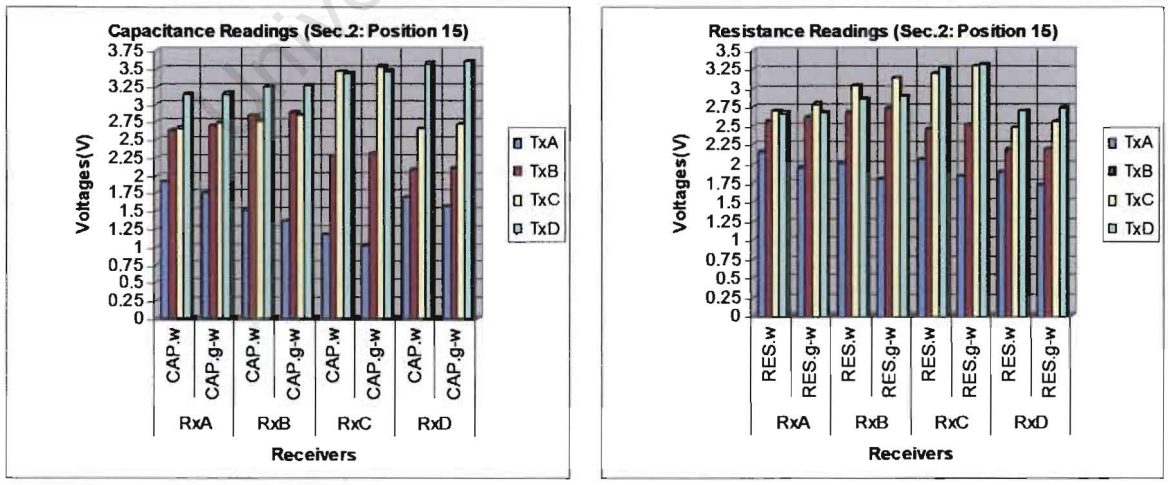

(a) (b)

Figure 6.28: DC voltages proportional to (a) the capacitance and (b) the resistance detected by the system. These values represent figure 6.27 (a) and were used for training the neural network.

Section 3 - Disturbance Source: big air-tube in front of transmitter TxD.

1. Results

		Receivers							
		Electric Field Disturbance (V)							
		RxA		RxB		RxC		RxD	
		Cap.	Res.	Cap.	Res.	Cap.	Res.	Cap.	Res.
Transmitters	TxA	-0.11475	-0.16846	-0.08952	-0.13916	-0.02686	-0.04314	-0.15462	-0.19287
	TxB	-0.1831	-0.18717	-0.18636	-0.1945	-0.12614	-0.13183	-0.15788	-0.13428
	TxC	-0.17741	-0.17334	-0.23356	-0.23844	-0.30029	-0.32145	-0.06755	-0.0529
	TxD	1.728517	1.488443	1.785483	1.56657	1.665847	1.70166	1.443687	1.337077

(b)

(a)

Figure 6.29: (a) The neural network desired output for the electric field disturbance (in volts) shown in the table above. (b) Table containing 32 numbers showing the electric field disturbance (in volts) that was caused by the insertion of the big air-tube in the vessel in the position illustrated in figure 6.29 (a).

2. Description

The capacitive and resistive transducers easily detect the disturbance caused by inserting the big air-tube in front of transmitter TxD.

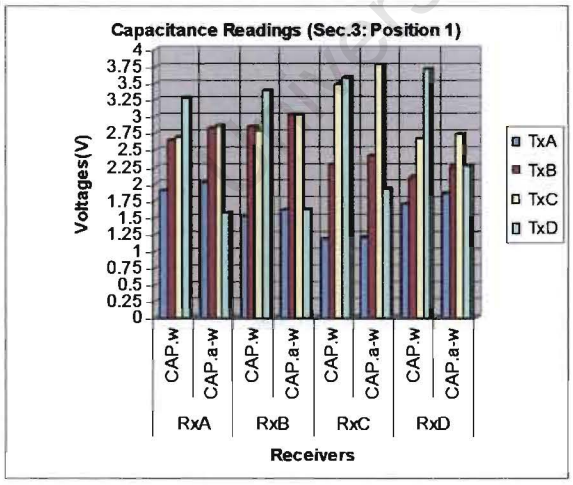

(a)

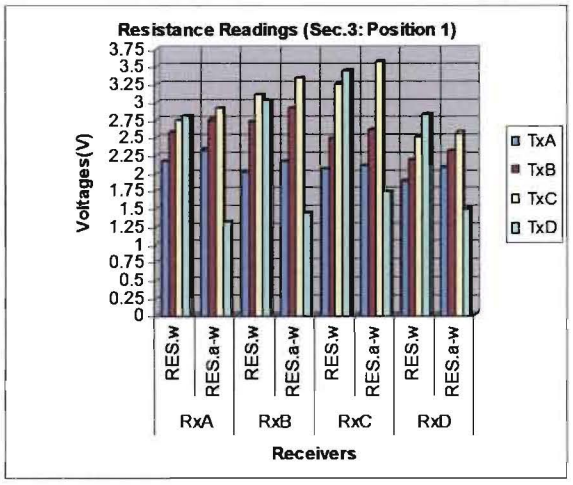

(b)

Figure 6.30: DC voltages proportional to (a) the capacitance and (b) the resistance detected by the system. These values represent figure 6.29 (a) and were used for training the neural network.

Section 3 - Disturbance Source: big air-tube in front of transmitter TxA.

1. Results

		Receivers							
		Electric Field Disturbance (V)							
		RxA		RxB		RxC		RxD	
		Cap.	Res.	Cap.	Res.	Cap.	Res.	Cap.	Res.
Transmitters	TxA	0.791722	1.123757	0.777997	1.141762	0.791112	1.175786	0.778197	1.036022
	TxB	-0.23137	-0.23839	-0.16622	-0.19979	-0.11047	-0.1325	-0.00051	-0.01836
	TxC	-0.12644	-0.11795	-0.17253	-0.20574	-0.17339	-0.19236	-0.11525	-0.1269
	TxD	0.007372	0.014903	-0.1415	-0.15539	-0.19354	-0.20925	-0.26347	-0.27613

(b)

(a)

Figure 6.31: (a) The neural network desired output for the electric field disturbance (in volts) shown in the table above. (b) Table containing 32 numbers showing the electric field disturbance (in volts) that was caused by the insertion of the big air-tube in the vessel in the position illustrated in figure 6.31 (a).

2. Description

The capacitive and resistive transducers detect a smaller disturbance than the one caused by the air-tube in front of TxD but equally well.

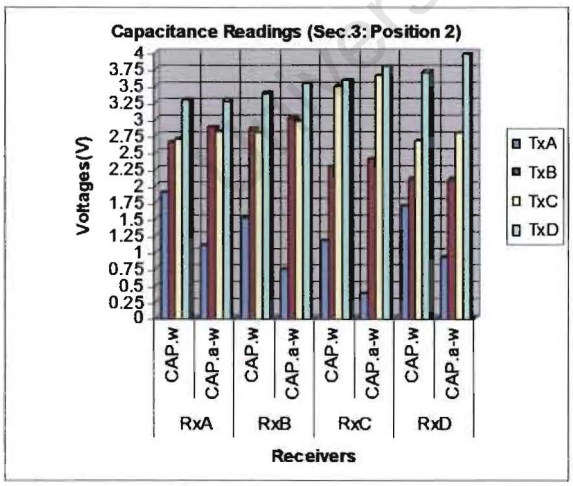

(a)

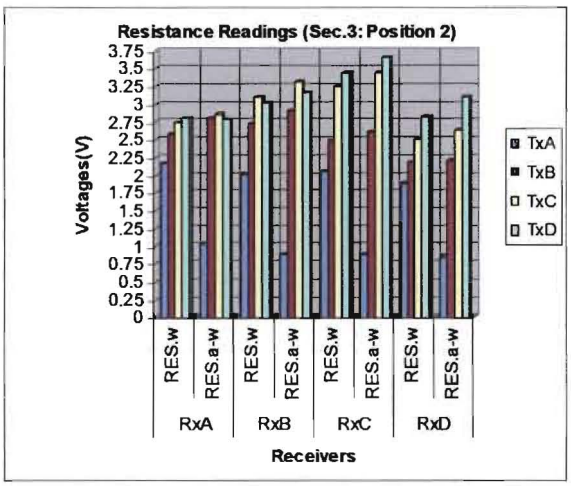

(b)

Figure 6.32: DC voltages proportional to (a) the capacitance and (b) the resistance detected by the system. These values represent figure 6.31 (a) and were used for training the neural network.

Section 3 - Disturbance Source: big air-tube close to transmitter TxD.

1. Results

		Receivers							
		Electric Field Disturbance (V)							
		RxA		RxB		RxC		RxD	
		Cap.	Res.	Cap.	Res.	Cap.	Res.	Cap.	Res.
Transmitters	TxA	-0.03133	-0.05331	0.000813	-0.01709	0.054931	0.077514	-0.03744	-0.0649
	TxB	-0.05392	-0.05676	-0.05534	-0.07406	0.03418	0.042113	0.015868	0.011188
	TxC	-0.00773	-0.00956	-0.0765	-0.09705	-0.08158	-0.09644	0.094808	0.084029
	TxD	0.189008	0.151569	0.209558	0.154824	-0.01486	-0.01669	-0.03174	-0.06449

(b)

(a)

Figure 6.33: (a) The neural network desired output for the electric field disturbance (in volts) shown in the table above. (b) Table containing 32 numbers showing the electric field disturbance (in volts) that was caused by the insertion of the big air-tube in the vessel in the position illustrated in figure 6.33 (a).

1. Results

The disturbance detected by the system's capacitance and resistance transducers is noticeably smaller in comparison to the one where the air-tube was positioned in front of TxD even though the air-tube was moved only 22mm away from the periphery wall.

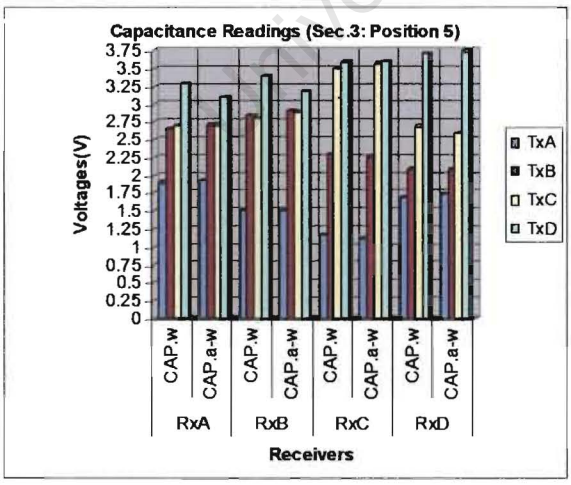

(a)

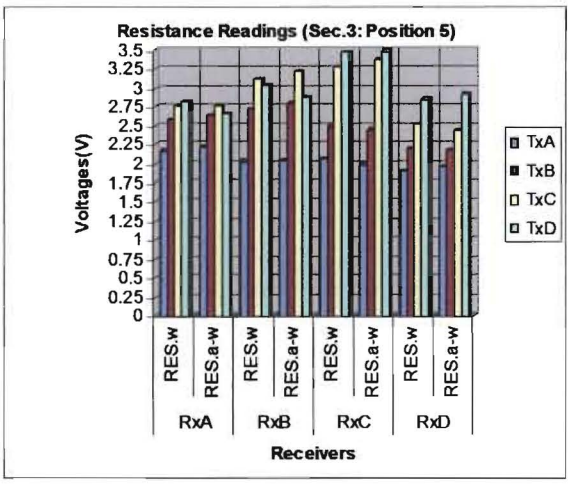

(b)

Figure 6.34: DC voltages proportional to (a) the capacitance and (b) the resistance detected by the system. These values represent figure 6.33 (a) and were used for training the neural network.

Section 3 - Disturbance Source: big air-tube in the centre of the rig.

1. Results

		Receivers							
		Electric Field Disturbance (V)							
		RxA		RxB		RxC		RxD	
		Cap.	Res.	Cap.	Res.	Cap.	Res.	Cap.	Res.
Transmitters	TxA	-0.02492	-0.04283	0.03418	0.033365	0.039569	0.048064	-0.02258	-0.04044
	TxB	-0.06719	-0.07706	-0.06124	-0.09155	0.049033	0.04308	0.03815	0.026192
	TxC	0.058697	0.057226	-0.06266	-0.0855	-0.05885	-0.07721	0.06663	0.045829
	TxD	0.075126	0.054982	0.089217	0.050708	-0.06597	-0.08596	-0.06572	-0.08346

(b)

(a)

Figure 6.35: (a) The neural network desired output for the electric field disturbance (in volts) shown in the table above. (b) Table containing 32 numbers showing the electric field disturbance (in volts) that was caused by the insertion of the big air-tube in the vessel in the position illustrated in figure 6.35 (a).

2. Description

The disturbance detected by the system's capacitance and resistance transducers is very small but still sufficient for the system to detect.

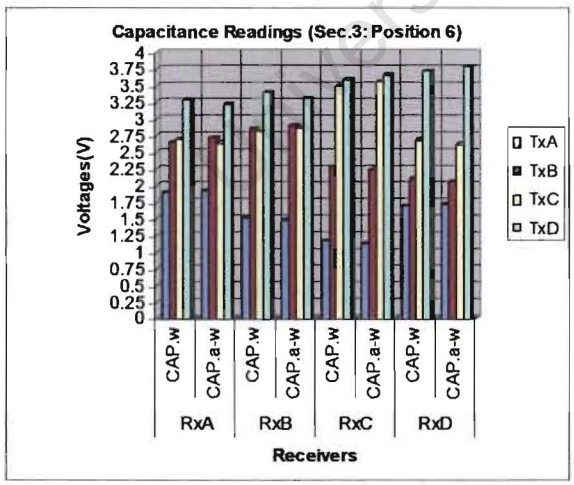

(a)

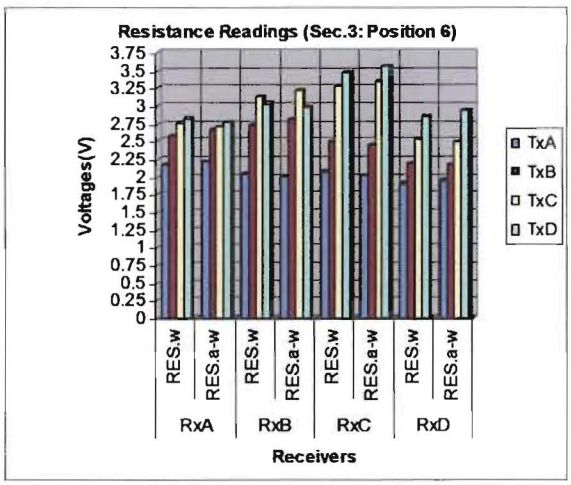

(b)

Figure 6.36: DC voltages proportional to (a) the capacitance and (b) the resistance detected by the system. These values represent figure 6.35 (a) and were used for training the neural network.

Section 3 - Disturbance Source: big air-tube in front of receiver RxD.

1. Results

		Receivers							
		Electric Field Disturbance (V)							
		RxA		RxB		RxC		RxD	
		Cap.	Res.	Cap.	Res.	Cap.	Res.	Cap.	Res.
Transmitters	TxA	-0.13255	-0.20579	-0.06104	-0.118	-0.01231	-0.03607	-0.09949	0.676626
	TxB	-0.20604	-0.22507	-0.18453	-0.21932	-0.14587	-0.17146	-0.0353	0.895233
	TxC	-0.17629	-0.18193	-0.2124	-0.24389	-0.23066	-0.25523	-0.0174	1.066435
	TxD	-0.01347	-0.02019	-0.13764	-0.14206	-0.31387	-0.32705	-0.16378	1.144866

(b)

(a)

Figure 6.37: (a) The neural network desired output for the electric field disturbance (in volts) shown in the table above. (b) Table containing 32 numbers showing the electric field disturbance (in volts) that was caused by the insertion of the big air-tube in the vessel in the position illustrated in figure 6.37 (a).

2. Description

The capacitive transducer RxD doesn't detect a positive disturbance. On the other hand resistive transducer RxD detects a very big disturbance.

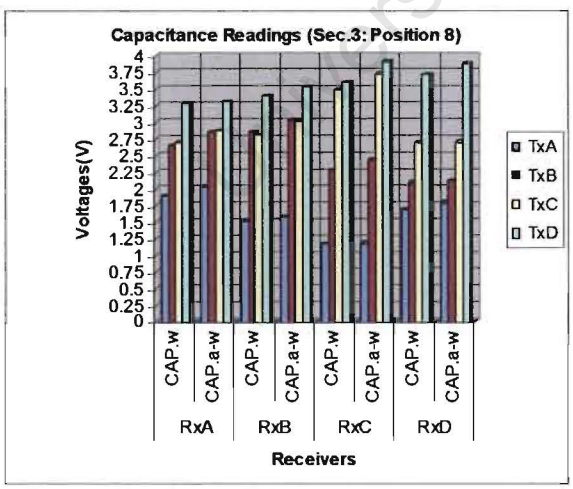

(a)

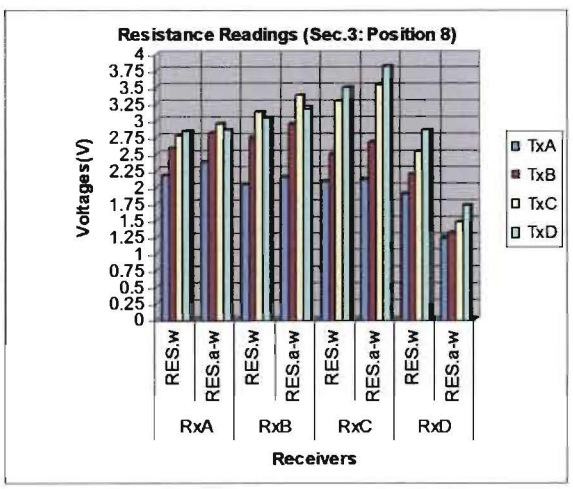

(b)

Figure 6.38: DC voltages proportional to (a) the capacitance and (b) the resistance detected by the system. These values represent figure 6.37 (a) and were used for training the neural network.

Section 3 - Disturbance Source: big air-tube close to transmitter TxA.

1. Results

		Receivers							
		Electric Field Disturbance (V)							
		RxA		RxB		RxC		RxD	
		Cap.	Res.	Cap.	Res.	Cap.	Res.	Cap.	Res.
Transmitters	TxA	-0.01953	-0.03988	0.071613	0.07975	0.073242	0.096435	-0.01465	-0.01994
	TxB	-0.08179	-0.09236	-0.06022	-0.08545	0.003253	-0.00936	0.082193	0.068763
	TxC	0.021978	0.020755	-0.0586	-0.08749	-0.06062	-0.0765	0.031738	0.019125
	TxD	0.138752	0.128168	0.027672	0.003662	-0.06307	-0.07649	-0.08138	-0.10132

(b)

(a)

Figure 6.39: (a) The neural network desired output for the electric field disturbance (in volts) shown in the table above.
(b) Table containing 32 numbers showing the electric field disturbance (in volts) that was caused by the insertion of the big air-tube in the vessel in the position illustrated in figure 6.39 (a).

2. Description

The disturbance detected by the system's capacitance and resistance transducers is noticeably smaller in comparison to the one where the air tube was positioned in front of TxA, even though the air-tube was moved only 22mm away from the periphery wall.

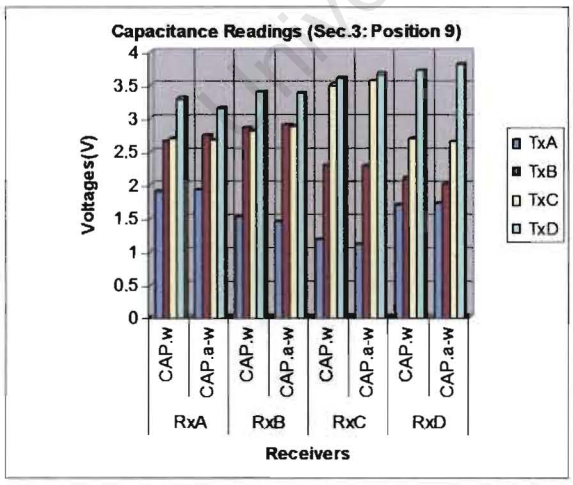

(a)

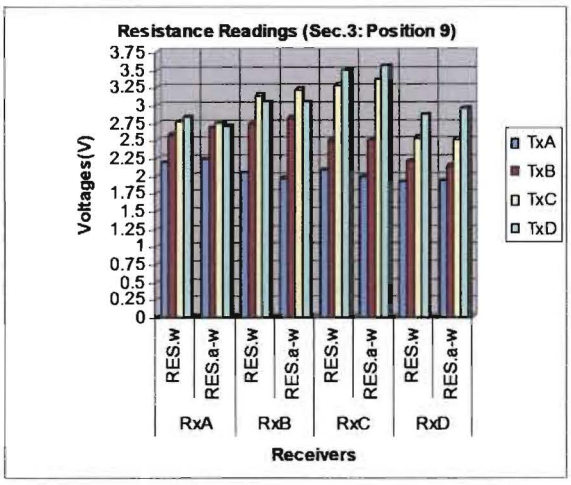

(b)

Figure 6.40: DC voltages proportional to (a) the capacitance and (b) the resistance detected by the system. These values represent figure 6.39 (a) and were used for training the neural network.

Section 3 - Disturbance Source: big air-tube in front of receiver RxA.

1. Results

		Receivers							
		Electric Field Disturbance (V)							
		RxA		RxB		RxC		RxD	
		Cap.	Res.	Cap.	Res.	Cap.	Res.	Cap.	Res.
Transmitters	TxA	-0.0416	0.545145	0.009767	-0.00651	-0.04141	-0.07869	-0.10396	-0.16067
	TxB	-0.11134	0.646615	-0.20122	-0.24292	-0.08362	-0.10849	0.001125	-0.0204
	TxC	0.045271	0.844371	-0.18718	-0.22405	-0.17298	-0.20213	-0.1299	-0.14033
	TxD	0.078587	0.921071	-0.14394	-0.14847	-0.1736	-0.19623	-0.18209	-0.19353

(b)

(a)

Figure 6.41: (a) The neural network desired output for the electric field disturbance (in volts) shown in the table above. (b) Table containing 32 numbers showing the electric field disturbance (in volts) that was caused by the insertion of the big air-tube in the vessel in the position illustrated in figure 6.41 (a).

2. Description

The capacitive transducer RxA detects a very small disturbance. On the other hand resistive transducer RxA detects a significantly larger disturbance.

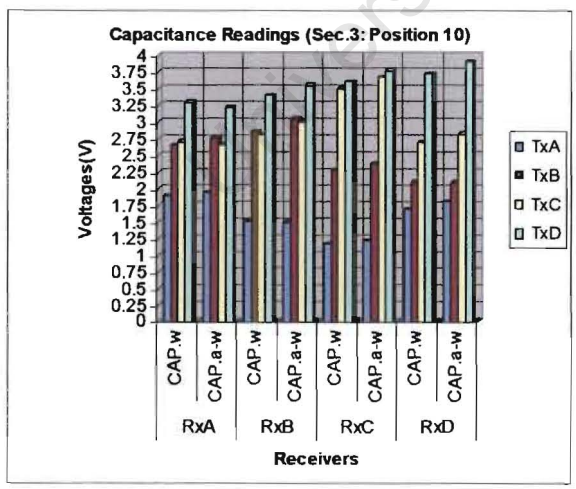

(a)

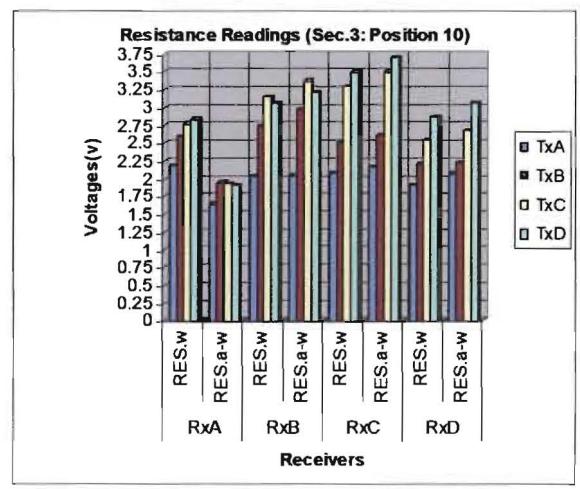

(b)

Figure 6.42: DC voltages proportional to (a) the capacitance and (b) the resistance detected by the system. These values represent figure 6.41 (a) and were used for training the neural network.

Section 4 - Disturbance Source: big gravel-bubble close to transmitter TxD.

1. Results

		Receivers							
		Electric Field Disturbance (V)							
		RxA		RxB		RxC		RxD	
		Cap.	Res.	Cap.	Res.	Cap.	Res.	Cap.	Res.
Transmitters	TxA	-0.00814	-0.01872	0.009763	0.00407	0.021973	0.034993	-0.01465	-0.01464
	TxB	-0.02604	-0.02848	-0.02686	-0.02604	0.008957	0.008137	0.010583	0.008953
	TxC	-0.01465	-0.01953	-0.04069	-0.04802	-0.04476	-0.05046	0.023603	0.029297
	TxD	0.06348	0.05371	0.06592	0.05941	-0.01872	-0.01872	-0.01872	-0.02523

(b)

(a)

Figure 6.43: (a) The neural network desired output for the electric field disturbance (in volts) shown in the table above.
(b) Table containing 32 numbers showing the electric field disturbance (in volts) that was caused by the insertion of the big gravel-bubble in the vessel in the position illustrated in figure 6.43 (a).

2. Description

The disturbance detected by the system's capacitance and resistance transducers is very small. There is sufficient difference between the air values and gravel values collected by the system at this position.

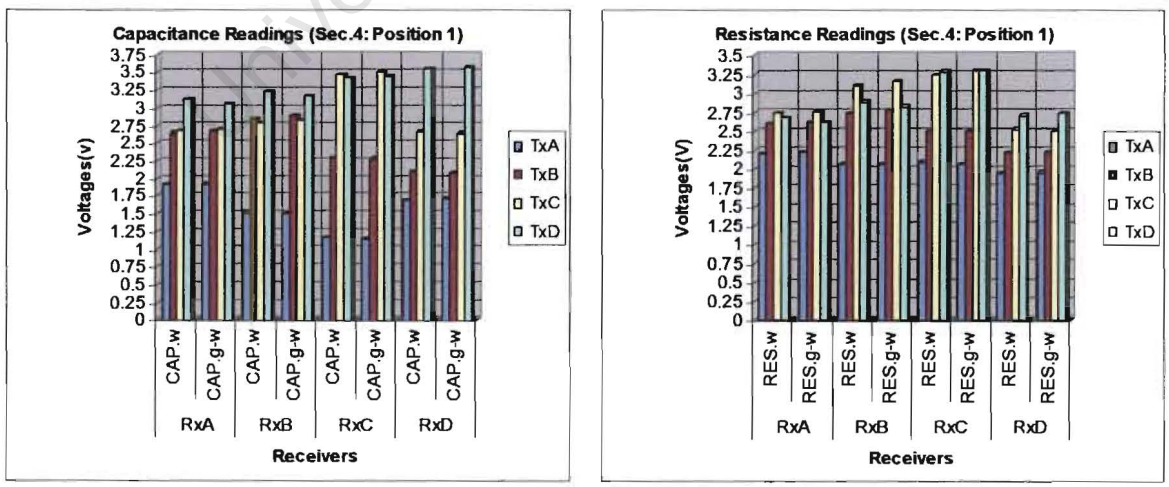

(a) (b)

Figure 6.44: DC voltages proportional to (a) the capacitance and (b) the resistance detected by the system. These values represent figure 6.43 (a) and were used for training the neural network.

Section 4 - Disturbance Source: big gravel-bubble in the centre of the rig.

1. Results

		Receivers							
		Electric Field Disturbance (V)							
		RxA		RxB		RxC		RxD	
		Cap.	Res.	Cap.	Res.	Cap.	Res.	Cap.	Res.
Transmitters	TxA	-0.00559	-0.01801	0.023495	0.025841	0.015464	0.02131	-0.00656	-0.01037
	TxB	-0.0293	-0.04008	-0.02843	-0.03265	0.018463	0.011541	0.016836	0.012058
	TxC	0.011187	0.002085	-0.04313	-0.05066	-0.03972	-0.05035	0.00809	0.003816
	TxD	0.018869	0.014803	0.015666	0.016327	-0.03698	-0.0412	-0.03205	-0.0355

(b)

(a)

Figure 6.45: (a) The neural network desired output for the electric field disturbance (in volts) shown in the table above. (b) Table containing 32 numbers showing the electric field disturbance (in volts) that was caused by the insertion of the big gravel-bubble in the vessel in the position illustrated in figure 6.45 (a).

2. Description

The disturbance detected by the system's capacitance and resistance transducers is very small but still sufficient for the system to detect. There is also a distinguishable difference between the air values and gravel values collected by the system at this position.

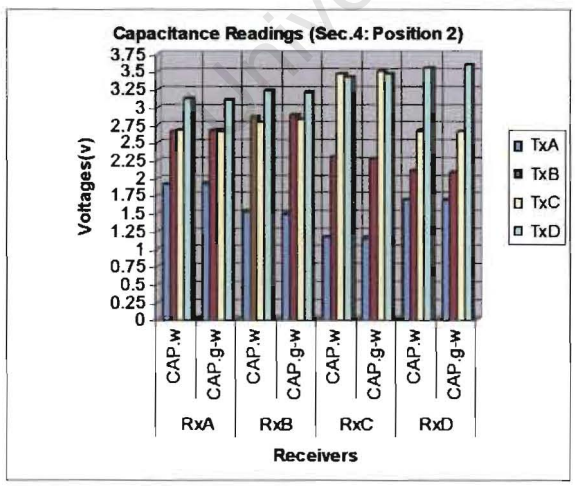

(a)

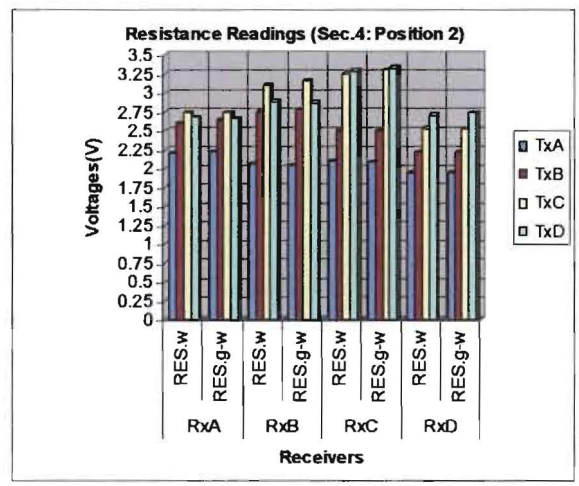

(b)

Figure 6.46: DC voltages proportional to (a) the capacitance and (b) the resistance detected by the system. These values represent figure 6.45 (a) and are used for training the neural network.

Section 4 - Disturbance Source: big gravel-bubble close to receiver RxD.

1. Results

		Receivers							
		Electric Field Disturbance (V)							
		RxA		RxB		RxC		RxD	
		Cap.	Res.	Cap.	Res.	Cap.	Res.	Cap.	Res.
Transmitters	TxA	-0.00692	-0.02075	0.022378	0.017903	0.030111	0.037232	-0.00671	-0.00001
	TxB	-0.02441	-0.03499	-0.02503	-0.0354	0.003052	-0.00834	0.028286	0.033572
	TxC	-0.01384	-0.02584	-0.04232	-0.05859	-0.04415	-0.059	0.016072	0.022582
	TxD	0.027469	0.024211	0.001625	-0.00468	-0.04944	-0.059	-0.04842	-0.04354

(b)

(a)

Figure 6.47: (a) The neural network desired output for the electric field disturbance (in volts) shown in the table above. (b) Table containing 32 numbers showing the electric field disturbance (in volts) that was caused by the insertion of the big gravel-bubble in the vessel in the position illustrated in figure 6.47 (a).

2. Description

The disturbance detected by the system's transducers is smaller in comparison to the one where the gravel-bubble is positioned in front of RxD (see position 8) even though the gravel-bubble was moved only 45mm away from the periphery wall.

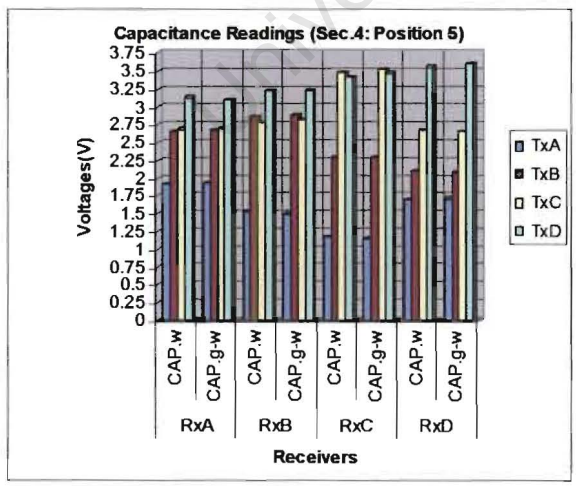

(a)

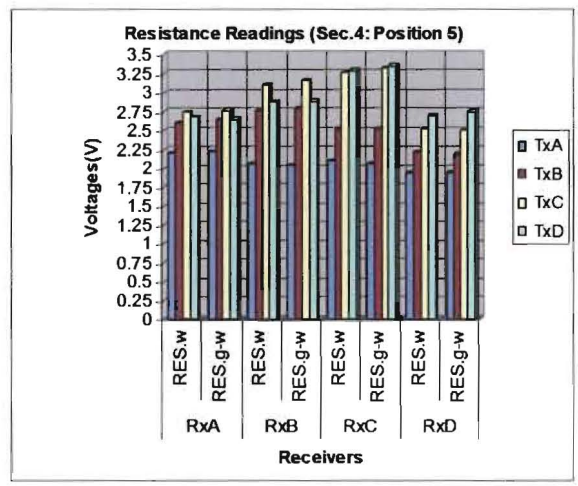

(b)

Figure 6.48: DC voltages proportional to (a) the capacitance and (b) the resistance detected by the system. These values represent figure 6.47 (a) and were used for training the neural network.

Section 4 - Disturbance Source: big gravel-bubble close to receiver RxA.

1. Results

		Receivers							
		Electric Field Disturbance (V)							
		RxA		RxB		RxC		RxD	
		Cap.	Res.	Cap.	Res.	Cap.	Res.	Cap.	Res.
Transmitters	TxA	0.001324	-0.01109	0.033664	0.038044	0.017091	0.018665	-0.01246	-0.01526
	TxB	-0.02685	-0.04008	-0.0323	-0.04364	0.014196	-0.00249	0.033726	0.01877
	TxC	0.016889	0.013684	-0.04069	-0.06287	-0.04155	-0.05971	-0.0149	-0.0265
	TxD	0.039825	0.043894	0.001018	-0.00218	-0.03189	-0.03998	-0.03326	-0.04242

(b)

(a)

Figure 6.49: (a) The neural network desired output for the electric field disturbance (in volts) shown in the table above. (b) Table containing 32 numbers showing the electric field disturbance (in volts) that was caused by the insertion of the big gravel-bubble in the vessel in the position illustrated in figure 6.49 (a).

2. Description

The disturbance detected by the system's transducers is smaller in comparison to the one where the gravel-bubble is positioned in front of RxA (see position 10) even though the gravel-bubble was moved only 45mm away from the periphery wall.

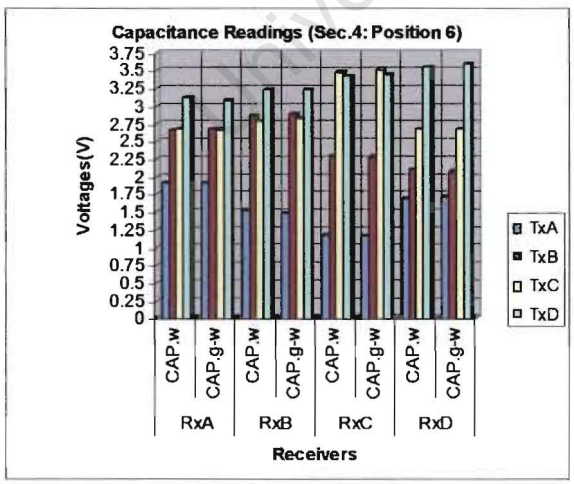

(a)

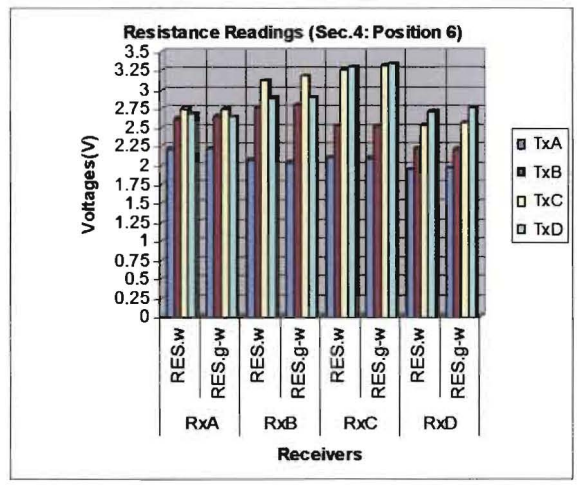

(b)

Figure 6.50: DC voltages proportional to (a) the capacitance and (b) the resistance detected by the system. These values represent figure 6.49 (a) and were used for training the neural network.

Section 4 - Disturbance Source: big gravel-bubble in front of receiver RxD.

1. Results

		Receivers							
		Electric Field Disturbance (V)							
		RxA		RxB		RxC		RxD	
		Cap.	Res.	Cap.	Res.	Cap.	Res.	Cap.	Res.
Transmitters	TxA	-0.03021	-0.065	-0.00397	-0.01688	0.013018	0.01002	-0.00768	0.194294
	TxB	-0.06917	-0.08769	-0.06312	-0.07558	-0.04328	-0.06404	0.018569	0.248769
	TxC	-0.06165	-0.08224	-0.08057	-0.09827	-0.0795	-0.10346	0.008597	0.274909
	TxD	-0.003	-0.00951	-0.04415	-0.04766	-0.09445	-0.10936	-0.03632	0.215354

(b)

(a)

Figure 6.51: (a) The neural network desired output for the electric field disturbance (in volts) shown in the table above. (b) Table containing 32 numbers showing the electric field disturbance (in volts) that was caused by the insertion of the big gravel-bubble in the vessel in the position illustrated in figure 6.51 (a).

2. Description

The disturbance detected by the system's capacitance and resistance transducer RxD is a noticeable one. There is also a distinguishable difference between the air values and gravel values collected by the system at this position.

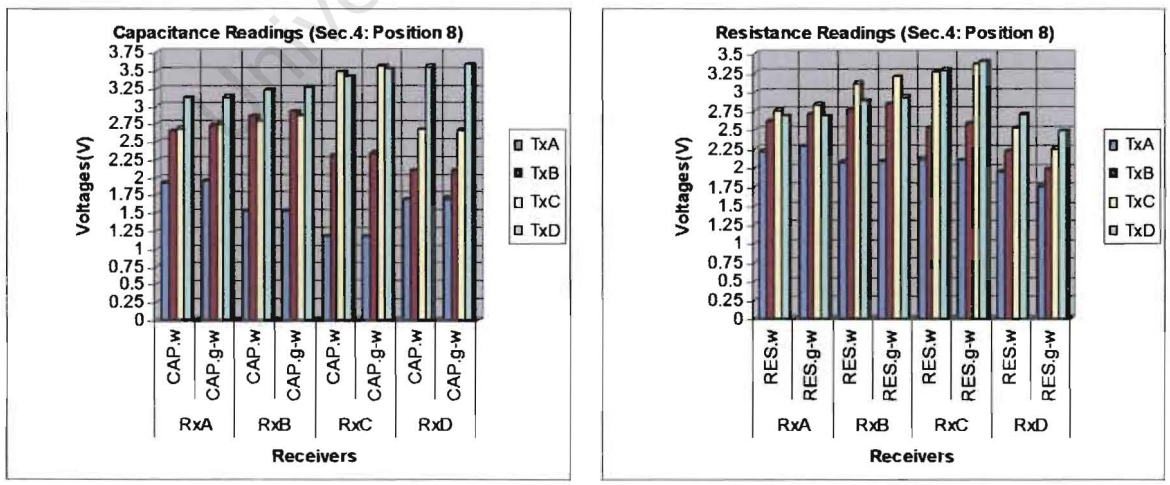

(a) (b)

Figure 6.52: DC voltages proportional to (a) the capacitance and (b) the resistance detected by the system. These values represent figure 6.51 (a) and were used for training the neural network.

Section 4 - Disturbance source: big gravel-bubble close to transmitter TxA.

1. Results

		Receivers							
		Electric Field Disturbance (V)							
		RxA		RxB		RxC		RxD	
		Cap.	Res.	Cap.	Res.	Cap.	Res.	Cap.	Res.
Transmitters	TxA	0.026853	0.031738	0.05778	0.078127	0.056152	0.088297	0.017497	0.035808
	TxB	-0.01139	-0.02442	-0.0061	-0.01465	0.016685	0.016683	0.050865	0.052493
	TxC	-0.02035	-0.02401	-0.05453	-0.07406	-0.05493	-0.06185	-0.02075	-0.01505
	TxD	0.013425	0.015872	-0.03743	-0.04516	-0.06388	-0.06673	-0.06836	-0.0651

(b)

(a)

Figure 6.53: (a) The neural network desired output for the electric field disturbance (in volts) shown in the table above.
(b) Table containing 32 numbers showing the electric field disturbance (in volts) that was caused by the insertion of the big gravel-bubble in the vessel in the position illustrated in figure 6.53 (a).

2. Description

The disturbance detected by the system's capacitance and resistance transducers is very small. There is sufficient difference between the air values and gravel values collected by the system at this position.

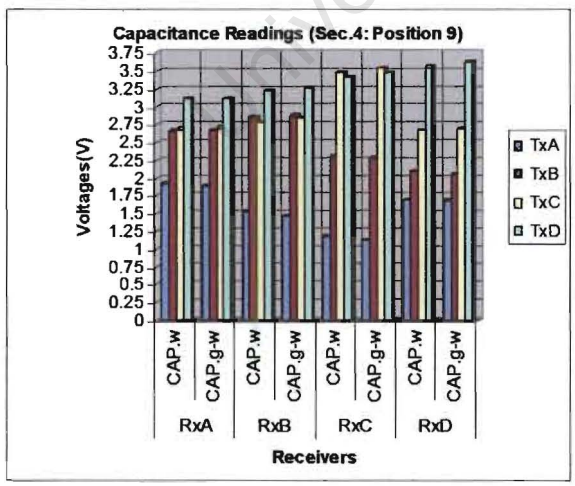

(a)

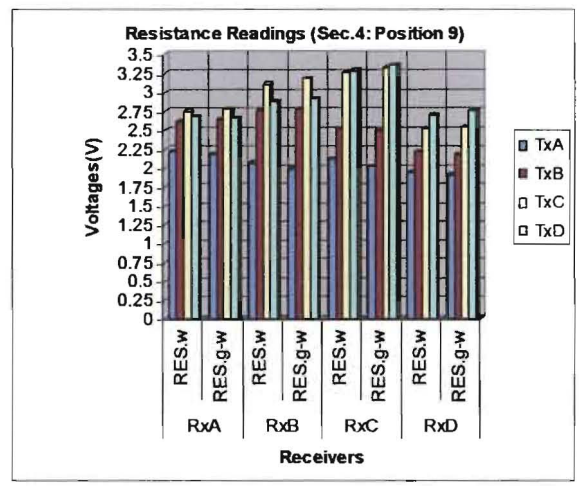

(b)

Figure 6.54: DC voltages proportional to (a) the capacitance and (b) the resistance detected by the system. These values represent figure 6.53 (a) and were used for training the neural network.

Section 4 - Disturbance source: big gravel-bubble in front of receiver RxA.

1. Results

		Receivers							
		Electric Field Disturbance (V)							
		RxA		RxB		RxC		RxD	
		Cap.	Res.	Cap.	Res.	Cap.	Res.	Cap.	Res.
Transmitters	TxA	-0.08616	0.778705	-0.05056	-0.09054	-0.0651	-0.11093	-0.09404	-0.14302
	TxB	-0.19369	0.934039	-0.17777	-0.20437	-0.13412	-0.15325	-0.10564	-0.12181
	TxC	-0.16703	1.00754	-0.20833	-0.23621	-0.2037	-0.22776	-0.18112	-0.19679
	TxD	-0.1858	1.034084	-0.22278	-0.20462	-0.2091	-0.22105	-0.19074	-0.21047

(b)

(a)

Figure 6.55: (a) The neural network desired output for the electric field disturbance (in volts) shown in the table above. (b) Table containing 32 numbers showing the electric field disturbance (in volts) that was caused by the insertion of the big gravel-bubble in the vessel in the position illustrated in figure 6.55 (a).

2. Description

The disturbance detected by the system's resistance transducer RxA is a noticeable one. There is also a distinguishable difference between the air values and gravel values collected by the system at this position.

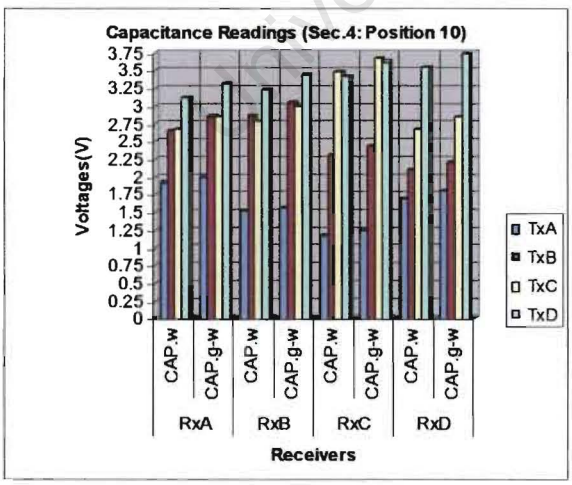

(a)

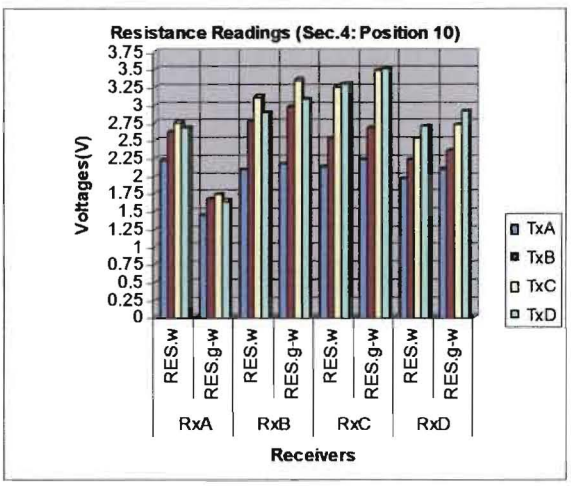

(b)

Figure 6.56: DC voltages proportional to (a) the capacitance and (b) the resistance detected by the system. These values represent figure 6.55 (a) and were used for training the neural network.

CHAPTER 7

7. PERFORMANCE OF EIT SYSTEM USING NEURAL NETWORKS

This chapter deals with the performance and the results of the different tests that were conducted on the final design. It is divided into two sections.

The first section is concerned with the system's performance by examining the performance measures, which are threshold error and volume fraction error predictions, obtained by performing image reconstruction of the rig's cross-section.

The second section is concerned with the system's performance by examining the volume fraction predictions obtained by training a neural network to predict the volume fractions of the different phases directly without having to first perform an image reconstruction.

The author would like to mention here that a comparison to an electrical impedance tomography (EIT) system employing frequency division multiplexing (FDM) using square-waves is also done in this chapter, since the same vessel (pipeline section) and electrode array were used for both systems.

Further, both systems employed the same air tube and gravel placement system and were tested with the same air-gravel-seawater phase configurations. Also, the same neural network topologies were used to perform the image reconstruction and volume fraction predictions for both systems and therefore. Therefore, any difference in the reconstruction and volume fraction predictions measured by the two systems independently is directly related to the square-waves or sine-waves transmitted through the measurement volume by the two different EIT systems.

7.1 Results using Neural Networks for Image Reconstruction

This section deals with the system's performance by examining the performance measures, threshold error and volume fraction error predictions, obtained by performing image reconstruction of the rig's cross-section.

7.1.1 Two-Phase Cross-Sectional Image Reconstruction

This section provides the results that were obtained by employing the neural network to perform two-phase image reconstruction, with the rig containing seawater and air-tubes or seawater and gravel-bubbles.

7.1.1.1 Seawater-Air Image Reconstruction

A number of experiments were performed using various neural network structures and training configurations. The network was trained using both gradient descent and Resilient back-propagation. Since, the neural network performance depends largely on the random initialization of the network's weights, five networks were trained and their results were averaged to give a more representative indication of the system's performance. Also, early stopping was employed, so that over-fitting would be prevented.

The best results were obtained using a single-layer feed-forward neural network, which was trained using gradient descent. This single-layer neural network was trained using training data points containing only seawater and air components. The network consisted of 32 input neurons fully connected to 88 output neurons, where each output neuron represents a pixel within the vessel cross-section.

The neural network reconstruction results are detailed in table 7.1 on the next page, which also presents the corresponding performance results of the electrical impedance tomography (EIT) system employing square-waves. The white cells indicate which of the compared cell entries showed better performance.

As can be seen the EIT system employing sine-waves outperforms the EIT system using square-waves on both, threshold error and volume fraction errors, performance measures.

PERFORMANCE MEASURE		IMPEDANCE TOMOGRAPHY SYSTEMS USING FREQUENCY DIVISION MULTIPLEXING	
		SQUARE-WAVE SYSTEM	SINE-WAVE SYSTEM
THRESHOLD ERROR (%)		9.149	7.879
VOLUME FRACTION ERROR (%)	WATER	5.041	3.876
	GRAVEL	0.00	0.00
	AIR	5.041	3.876
SUM VOLUME FRACTION ERROR (%)		10.082	7.752

Table 7.1: Comparison between the performances of two EIT systems for a two-phase air-seawater image reconstruction employing single-layer feed-forward neural networks using gradient descent.

The performance of the EIT system employing sine-waves is visually evident in figures 7.1, 7.2, 7.3, 7.4 and 7.5, where specific test cases for the single-layer feed-forward neural network using gradient descent are displayed. Each picture consisting of two cross-sectional images, with image on the right being the desired network output and image on the left being the network prediction.

These figures illustrate the reconstruction results for the 5 cases that the author took in to consideration when the training database was being generated. These test cases show the ability of the single-layer feed-forward neural network using gradient descent to generalize from single air tubes used for the training data set, to multiple air-tubes of different sizes or different shapes (e.g. a half round tube) in the test data set.

The results of these five cases for a two-phase air-seawater image reconstruction are illustrated in the following 5 pages.

TEST CASE 1

1. Results

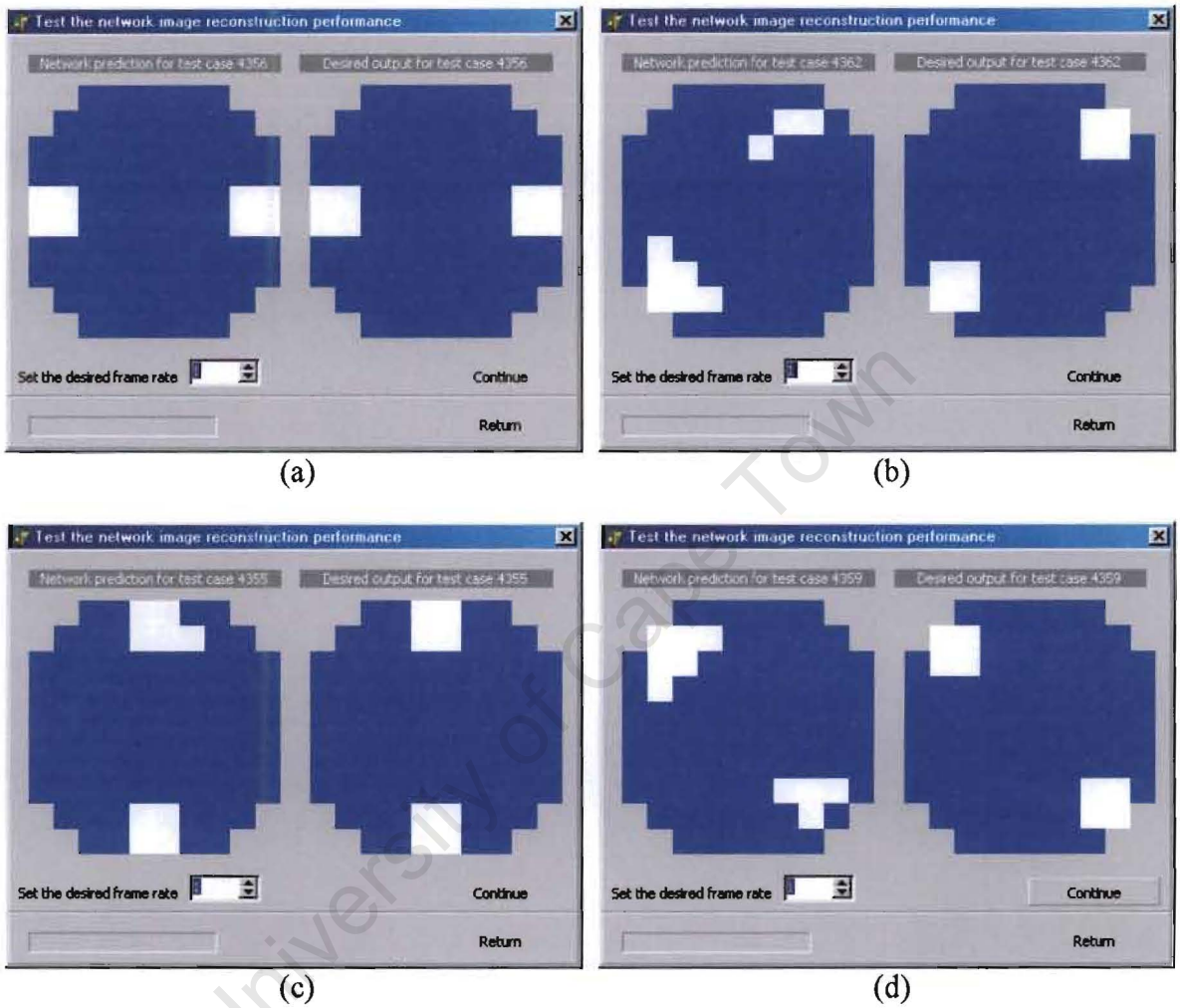

Figure 7.1: Test case 1 for a two-phase air-seawater image reconstruction employing a single-layer feed-forward neural network using gradient descent.

2. Description

Test case 1 involves two small air-tubes each having a diameter of 45mm. The air-tubes are placed directly opposite to each other and they are rotated around the periphery of the vessel. In picture (a) the two air-tubes are positioned in front of transmitters TxA and TxC, in picture (b) the air-tubes are placed in front of receivers RxA and RxC, in picture (c) the air-tubes are positioned in front of transmitters TxB and TxD, and in picture (d) the air-tubes are placed in front of receivers RxB and RxD.

TEST CASE 2

1. Results

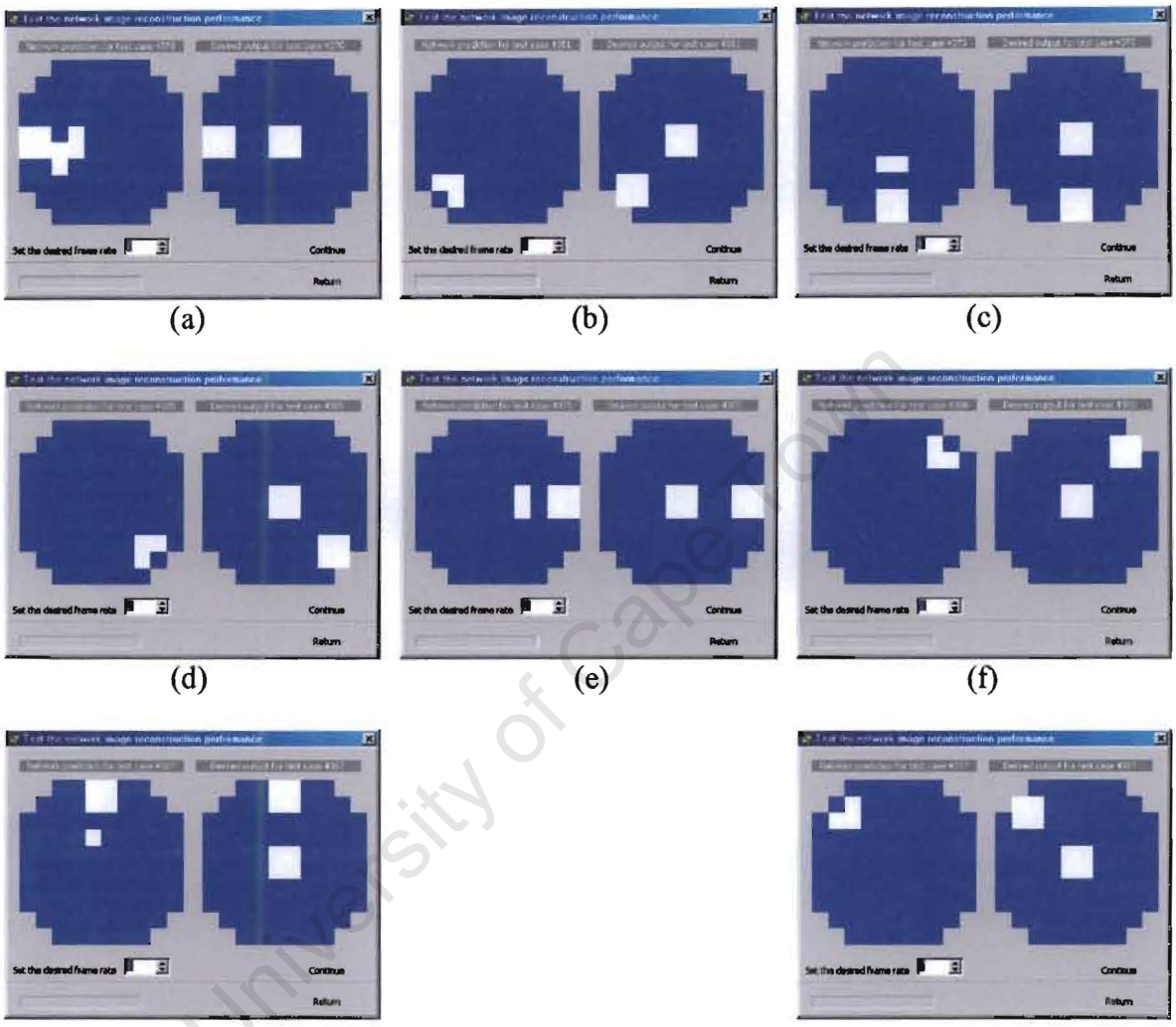

(a) (b) (c)

(d) (e) (f)

(g) (h)

Figure 7.2: Test case 2 for a two-phase air-seawater image reconstruction employing a single-layer feed-forward neural network using gradient descent.

2. Description

Test case 2 also involves two small air-tubes each having a diameter of 45mm. The one air-tube is placed in the centre of the vessel and the other one is rotated around the periphery of the vessel. In picture (a) it is placed in front of transmitter TxA, in (b) in front of receiver RxA, in (c) in front of transmitter TxB, in (d) in front of receivers RxB, in (e) in front of transmitter TxC, in (f) in front of receivers RxC and so on.

TEST CASE 3

1. Results

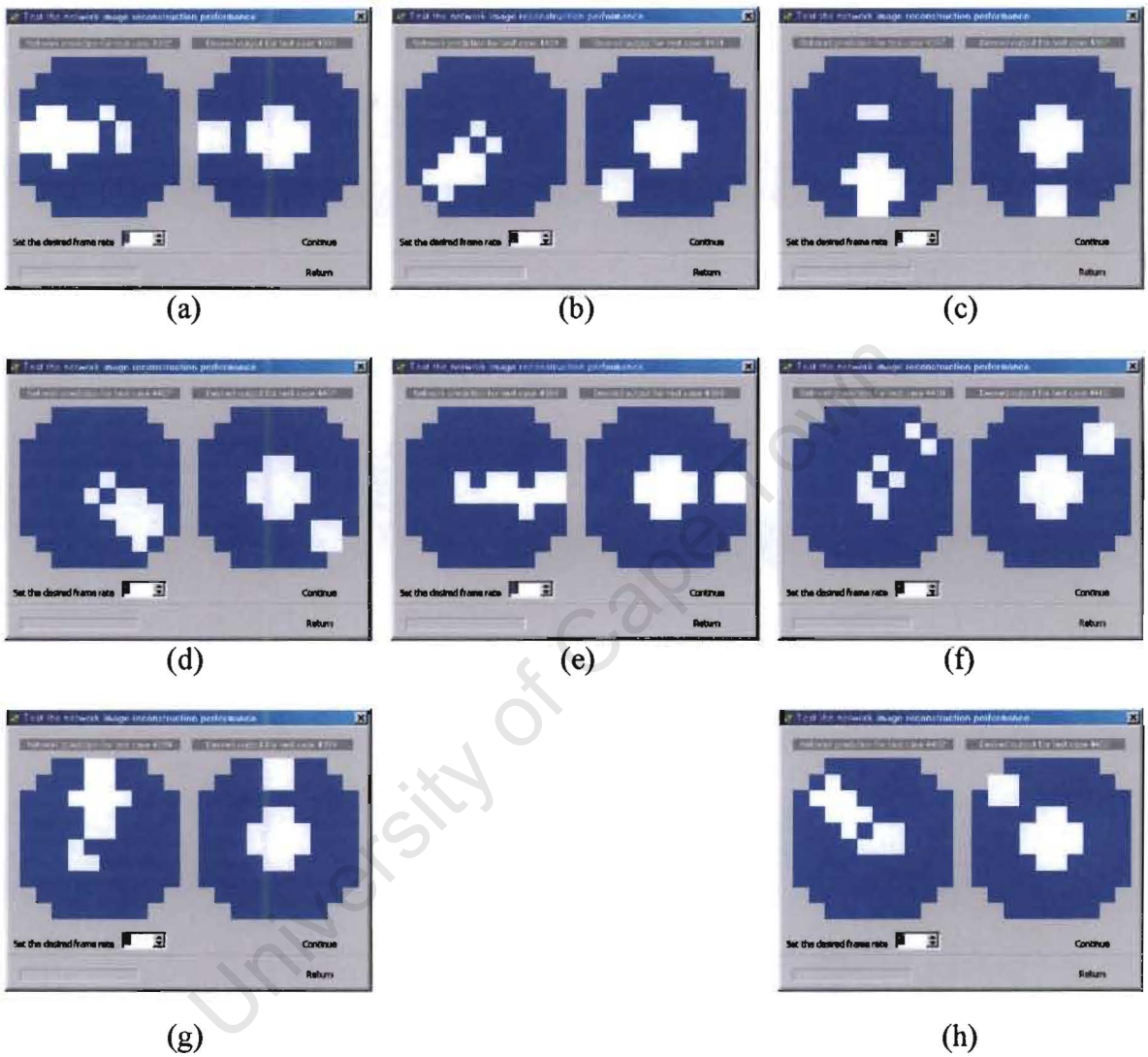

Figure 7.3: Test case 3 for a two-phase air-seawater image reconstruction employing a single-layer feed-forward neural network using gradient descent.

2. Description

Test case 3 involves one small air-tube (45mm) and one big air-tube (90mm). The big air-tube is placed in the centre of the rig and the small one is rotated around the periphery of the vessel. In picture (a) it is placed in front of transmitter TxA, in (b) in front of receiver RxA, in (c) in front of transmitter TxB, in (d) in front of receivers RxB, in (e) in front of transmitter TxC, in (f) in front of receivers RxC and so on.

TEST CASE 4

1. Results

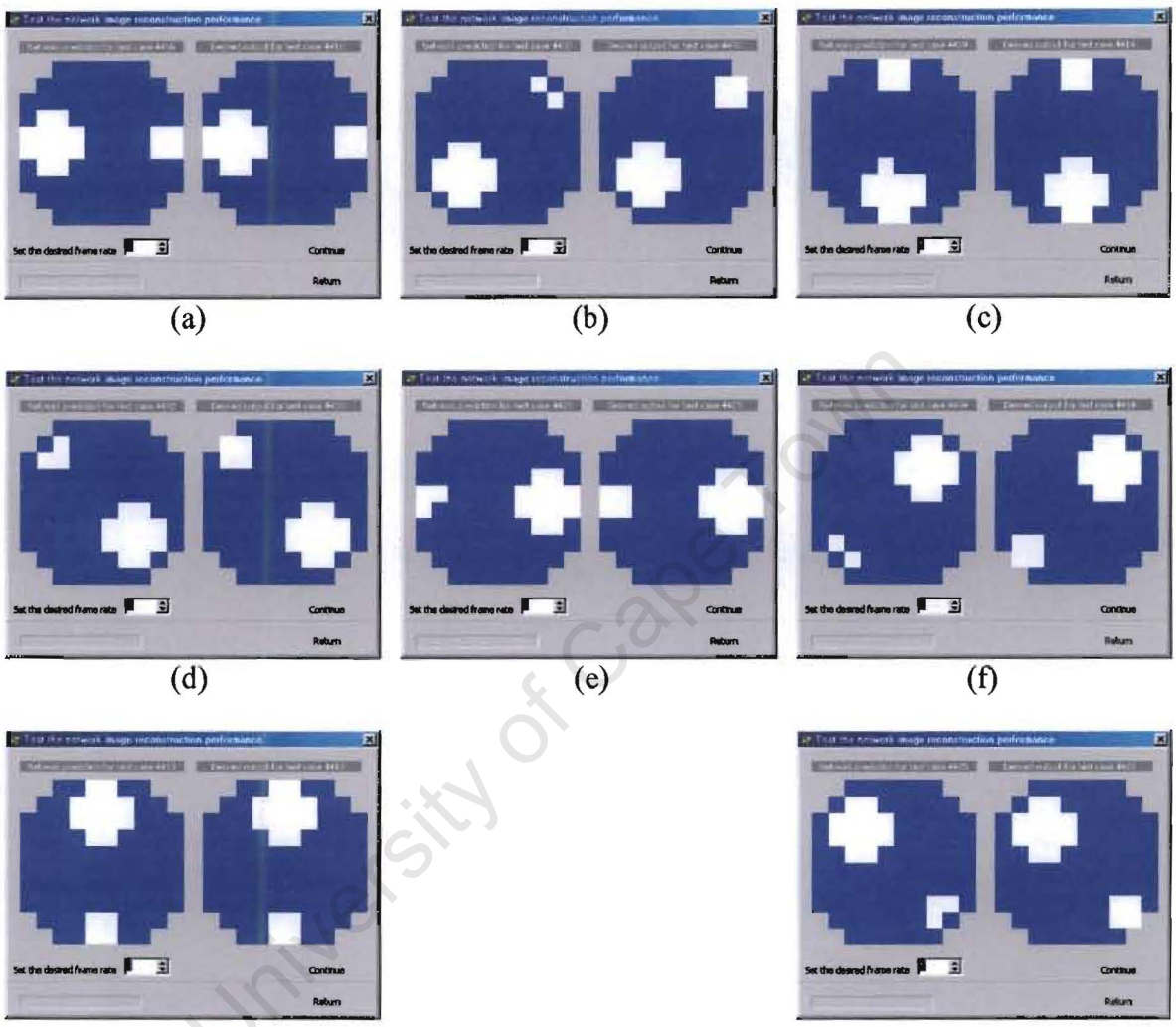

(a) (b) (c)

(d) (e) (f)

(g) (h)

Figure 7.4: Test case 4 for a two-phase air-seawater image reconstruction employing a single-layer feed-forward neural network using gradient descent.

2. Description

Test case 4 also involves one small air-tube and one big air-tube. The two air-tubes are positioned directly opposed to each other. The big air-tube is used as the reference tube and both of them are rotated around the rig. As the air-tubes are moved around the vessel, both are placed in front of transmitters or in front of receivers alternatively starting with the big tube positioned in front of TxA and the small tube in front of TxC

TEST CASE 5

1. Results

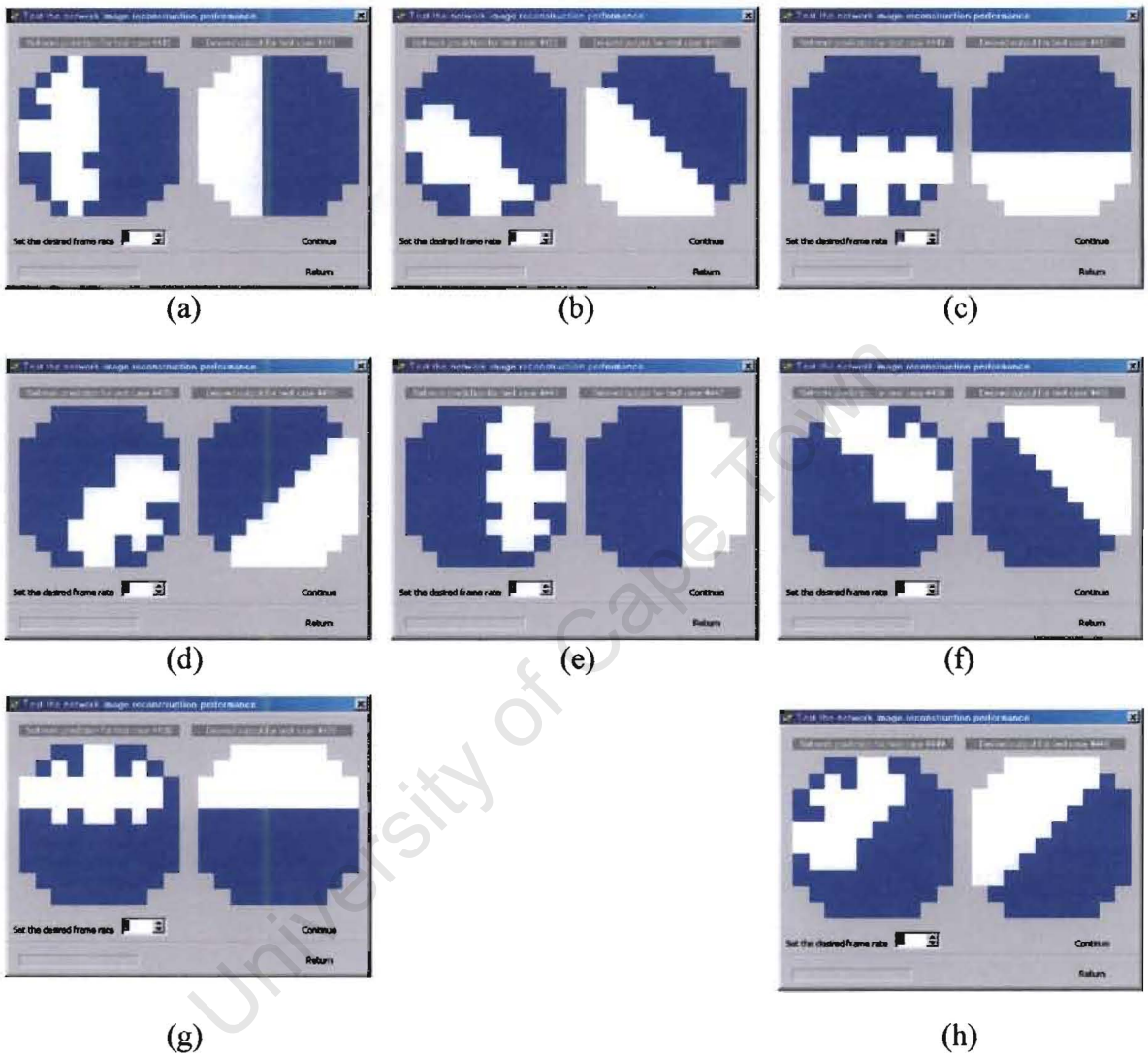

(a) (b) (c)

(d) (e) (f)

(g) (h)

Figure 7.5: Test case 5 for a two-phase air-seawater image reconstruction employing a single-layer feed-forward neural network using gradient descent.

2. Description

Test case 5 involves an air-tube that was not used in the training database. It is a half round tube, which almost covers half the rig's space. The air-tube is positioned flat against the vessel's inner wall and is also rotated anticlockwise around the vessel. It is initially placed in front of TxA (see figure 7.5 (a)) then in front of RxA (see figure 7.5 (b)) and so on until the entire cross-section of the vessel is covered.

7.1.1.2 Seawater-Gravel Image Reconstruction

After the completion of the tests, the results showed that the single-layer feed-forward neural network using gradient descent obtained the best results. As in the previous section, five networks were trained and their results were averaged to give a more representative indication of the system's performance. Also, early stopping was employed, so that over-fitting would be prevented.

This single-layer neural network was trained using the training data points containing only seawater and gravel components. The network consisted of 32 input neurons fully connected to 88 output neurons, where each output neuron representing a pixel within the vessel cross-section.

The neural network reconstruction results are detailed in table 7.2 below, which also presents the corresponding performance results of the electrical impedance tomography (EIT) system employing square-waves. The white cells indicate which of the compared cell entries obtained a better performance.

PERFORMANCE MEASURE		IMPEDANCE TOMOGRAPHY SYSTEMS USING FREQUENCY DIVISION MULTIPLEXING	
		SQUARE-WAVE SYSTEM	SINE-WAVE SYSTEM
THRESHOLD ERROR (%)		8.693	8.221
VOLUME FRACTION ERROR (%)	WATER	4.375	2.550
	GRAVEL	4.375	2.550
	AIR	0.00	0.00
SUM VOLUME FRACTION ERROR (%)		8.75	5.100

Table 7.2: Comparison between the performances of two EIT systems for a two-phase gravel-seawater image reconstruction employing single-layer feed-forward neural networks using gradient descent.

As can be seen the EIT system employing sine-waves outperforms the EIT system using square-waves on both, threshold error and volume fraction errors, performance measures.

The performance of the EIT system employing sine-waves is visually evident in figures 7.6, 7.7, 7.8, and 7.9, where specific test cases for the single-layer feed-forward neural network using gradient descent are displayed. Each picture consisting of two cross-sectional images, the image on the right being the desired network output and the image on the left being the network prediction.

Figures 7.6, 7.7, 7.8, and 7.9 illustrate the reconstruction results for the 4 cases that the author took in to consideration when the training database was being generated. These test cases show the ability of the single-layer feed-forward neural network using gradient descent to generalize from single gravel-bubbles used for the training data set to the multiple gravel-bubbles of different sizes in the test data set.

The results of these five cases for a two-phase air-seawater image reconstruction are illustrated in the following 4 pages.

TEST CASE 1

1. Results

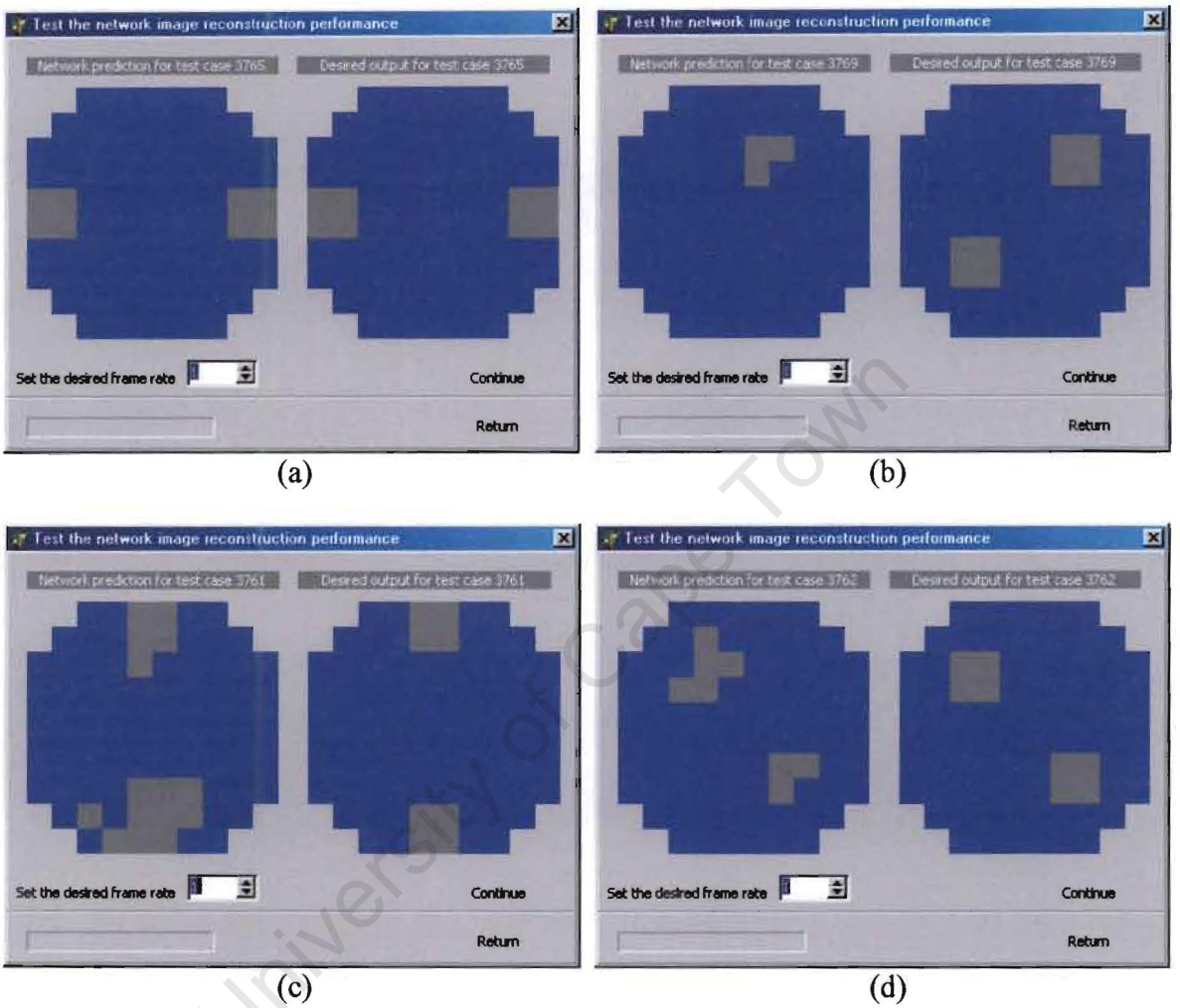

Figure 7.6: Test case 1 for a two-phase gravel-seawater image reconstruction employing a single-layer feed-forward neural network using gradient descent.

2. Description

Test case 1 involves two small gravel-bubbles each having a diameter of 45mm. The gravel-bubbles are placed directly opposite to each other. In picture (a) the two gravel-bubbles are positioned in front of transmitters TxA and TxC, in picture (b) the gravel-bubbles are placed in front of receivers RxA and RxC, in picture (c) the gravel-bubbles are positioned in front of transmitters TxB and TxD, and in picture (d) the gravel-bubbles are placed in front of receivers RxB and RxD.

TEST CASE 2

1. Results

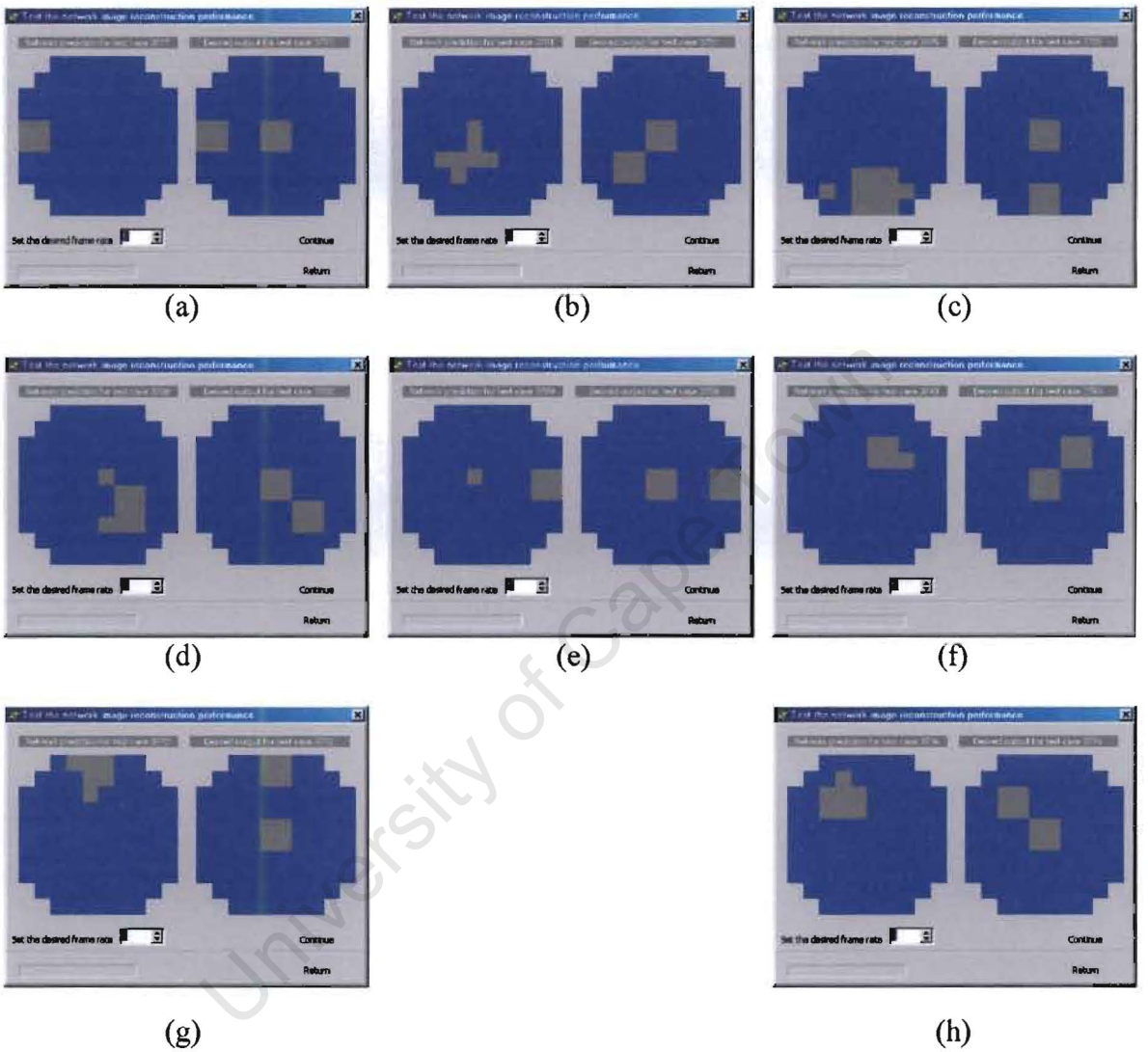

Figure 7.7: Test case 2 for a two-phase gravel-seawater image reconstruction employing a single-layer feed-forward neural network using gradient descent.

2. Description

Test case 2 also involves two small gravel-bubbles each having a diameter of 45mm. The one gravel-bubble is placed in the centre of the rig and the other one is rotated anticlockwise around the periphery of the vessel. In picture (a) it is placed in front of transmitter TxA, in (b) in front of receiver RxA, in (c) in front of transmitter TxB, in (d) in front of receivers RxB, in (e) in front of transmitter TxC and so on.

TEST CASE 3

1. Results

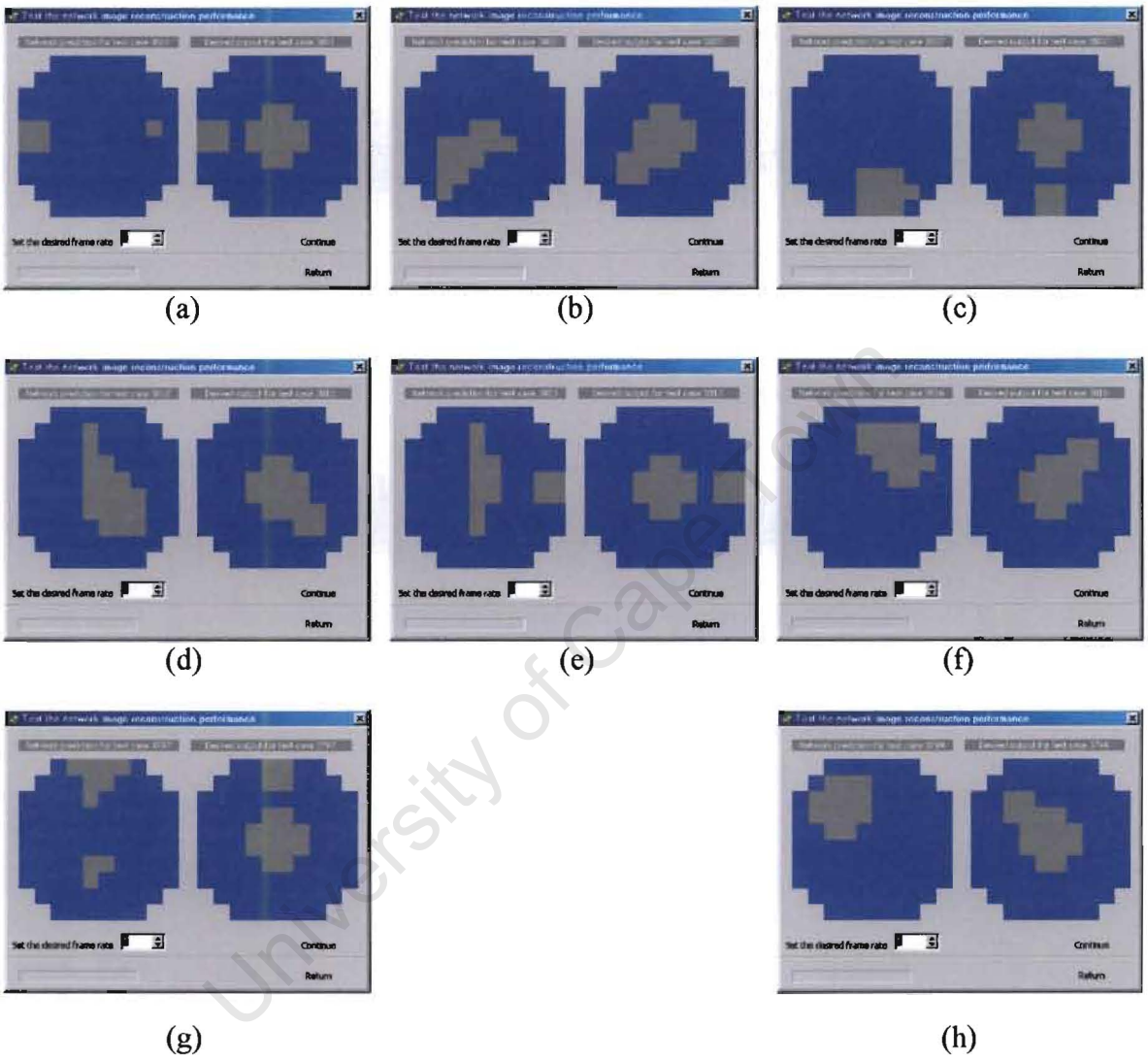

(a) (b) (c)

(d) (e) (f)

(g) (h)

Figure 7.8: Test case 3 for a two-phase gravel-seawater image reconstruction employing a single-layer feed-forward neural network using gradient descent.

2. Description

Test case 3 involves one small gravel-bubble (45mm) and one big gravel-bubble (90mm). The big gravel-bubble is placed in the centre of the vessel and the small one is rotated around the periphery of the vessel. In picture (a) it is placed in front of transmitter TxA, in (b) in front of receiver RxA, in (c) in front of transmitter TxB, in (d) in front of receivers RxB, in (e) in front of transmitter TxC, in (f) in front of receivers RxC and so on.

TEST CASE 4

1. Results

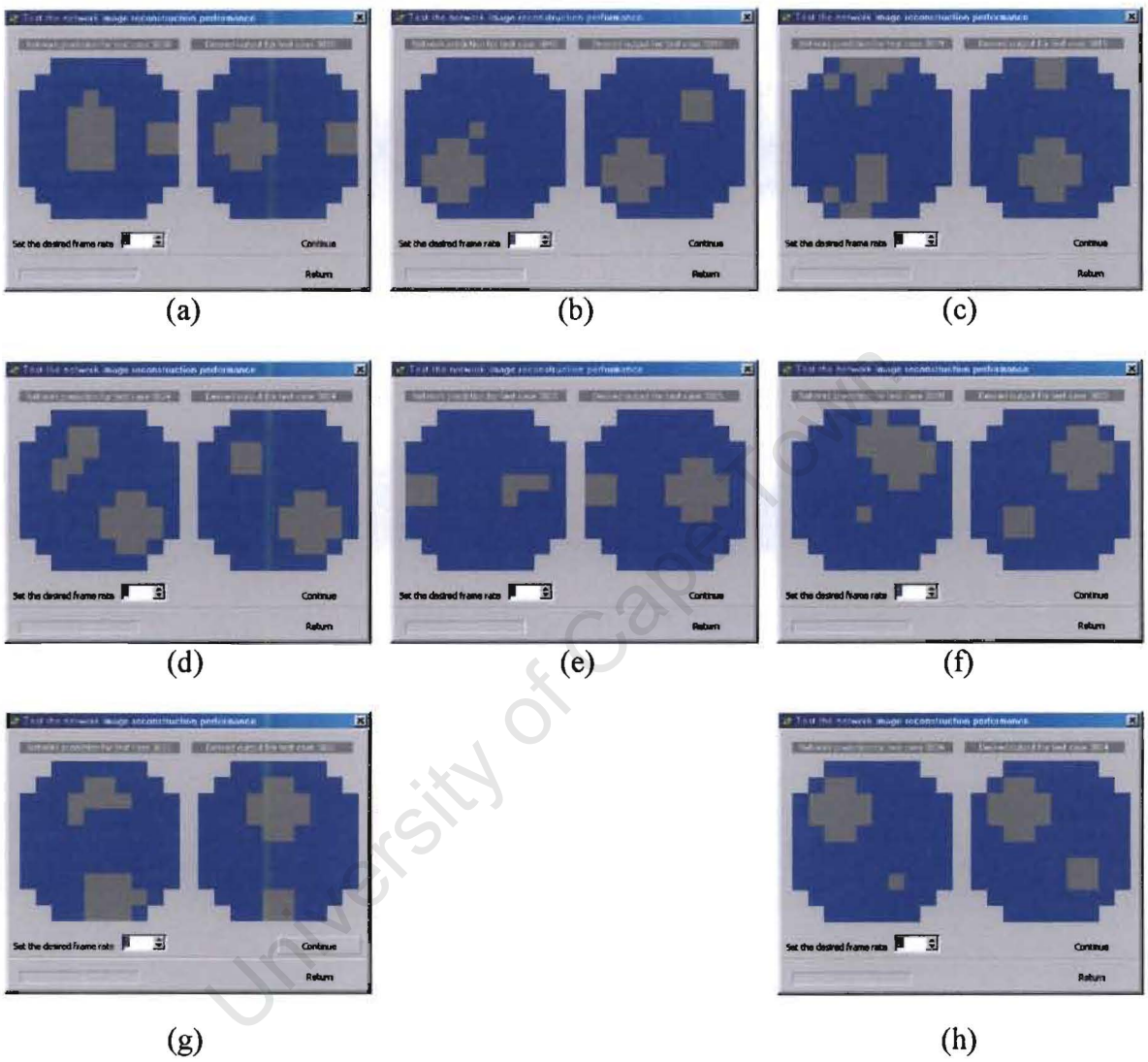

Figure 7.9: Test case 4 for a two-phase gravel-seawater image reconstruction employing a single-layer feed-forward neural network using gradient descent.

2. Description

Test case 4 also involves one small and one big gravel-bubble. The two gravel-bubbles are positioned directly opposed to each other. The big bubble is used as the reference tube and both are rotated anticlockwise around the vessel. As the gravel-bubbles moved around the vessel both of they are placed in front of transmitters or in front of receivers alternatively starting with the big bubble placed in front of TxA and the small in front of TxC.

7.1.2 Three-Phase Cross-Sectional Image Reconstruction

After the completion of the tests, the results showed that the single-layer feed-forward neural network using gradient descent obtained the best results (see table 7.3), even though Teague states in his Ph.D. thesis [53] that a single-layer feed-forward neural network using Resilient back-propagation was used to obtain his results (see table 7.4). As in the two-phase image reconstruction, here again five networks were trained and their results were averaged to give a more representative indication of the system's performance. Also, early stopping was employed, so that over-fitting would be prevented.

The single-layer neural networks were trained using the data points containing air, gravel and seawater components. The network consisted of 32 input neurons fully connected to 264 output neurons, where each output neuron representing a pixel within the vessel cross-section.

PERFORMANCE MEASURE		IMPEDANCE TOMOGRAPHY SYSTEMS USING FREQUENCY DIVISION MULTIPLEXING	
		SQUARE-WAVE SYSTEM	SINE-WAVE SYSTEM
THRESHOLD ERROR (%)		Not Available	11.652
VOLUME FRACTION ERROR (%)	WATER	Not Available	4.840
	GRAVEL	Not Available	5.545
	AIR	Not Available	2.902
SUM VOLUME FRACTION ERROR (%)		Not Available	13.287

Table 7.3: Comparison between the performances of two EIT systems for a three-phase air-gravel-seawater image reconstruction employing single-layer feed-forward neural networks using gradient descent.

The author's best neural network reconstruction results are detailed in table 7.3 above, and table 7.4 on the next page, presents a comparison between the results obtained by the author and the results obtained by the electrical impedance tomography (EIT) system employing square-waves, both employing single-layer feed-forward neural networks using

Resilient back-propagation. The white cells indicate which of the compared cell entries obtained a better performance.

PERFORMANCE MEASURE		IMPEDANCE TOMOGRAPHY SYSTEMS USING FREQUENCY DIVISION MULTIPLEXING	
		SQUARE-WAVE SYSTEM	SINE-WAVE SYSTEM
THRESHOLD ERROR (%)		12.879	12.368
VOLUME FRACTION ERROR (%)	WATER	5.621	4.416
	GRAVEL	5.303	5.496
	AIR	2.933	3.034
SUM VOLUME FRACTION ERROR (%)		13.857	12.946

Table 7.4: Comparison between the performances of two EIT systems for a three-phase air-gravel-seawater image reconstruction employing single-layer feed-forward neural networks using Resilient back-propagation.

As can be seen in Table 7.4 the EIT system employing sine-waves outperforms the EIT system using square-waves on both the threshold error and sum volume fraction error performance measures, although the square-wave system obtained better air and gravel volume fraction errors.

The performance of the EIT system employing sine-waves is visually evident in figures 7.10, 7.11, 7.12, 7.13, 7.14, 7.15, 7.16 and 7.17, where specific test cases for the single-layer feed-forward neural network using gradient descent are displayed. Each picture consisting of two cross-sectional images, the image on the right being the desired network output and the image on the left being the network prediction.

These figures illustrate the reconstruction results for the 8 cases that the author took in to consideration when the training database was being generated. These test cases show the ability of the single-layer feed-forward neural network using gradient descent to generalize from single air-tubes and gravel-bubbles used for the training data set to the combinations of multiple air-tubes and/or gravel-bubbles of different sizes in the test data set.

The results of these five cases for a three-phase air-gravel-seawater image reconstruction are illustrated in the following 8 pages.

TEST CASE 1

1. Results

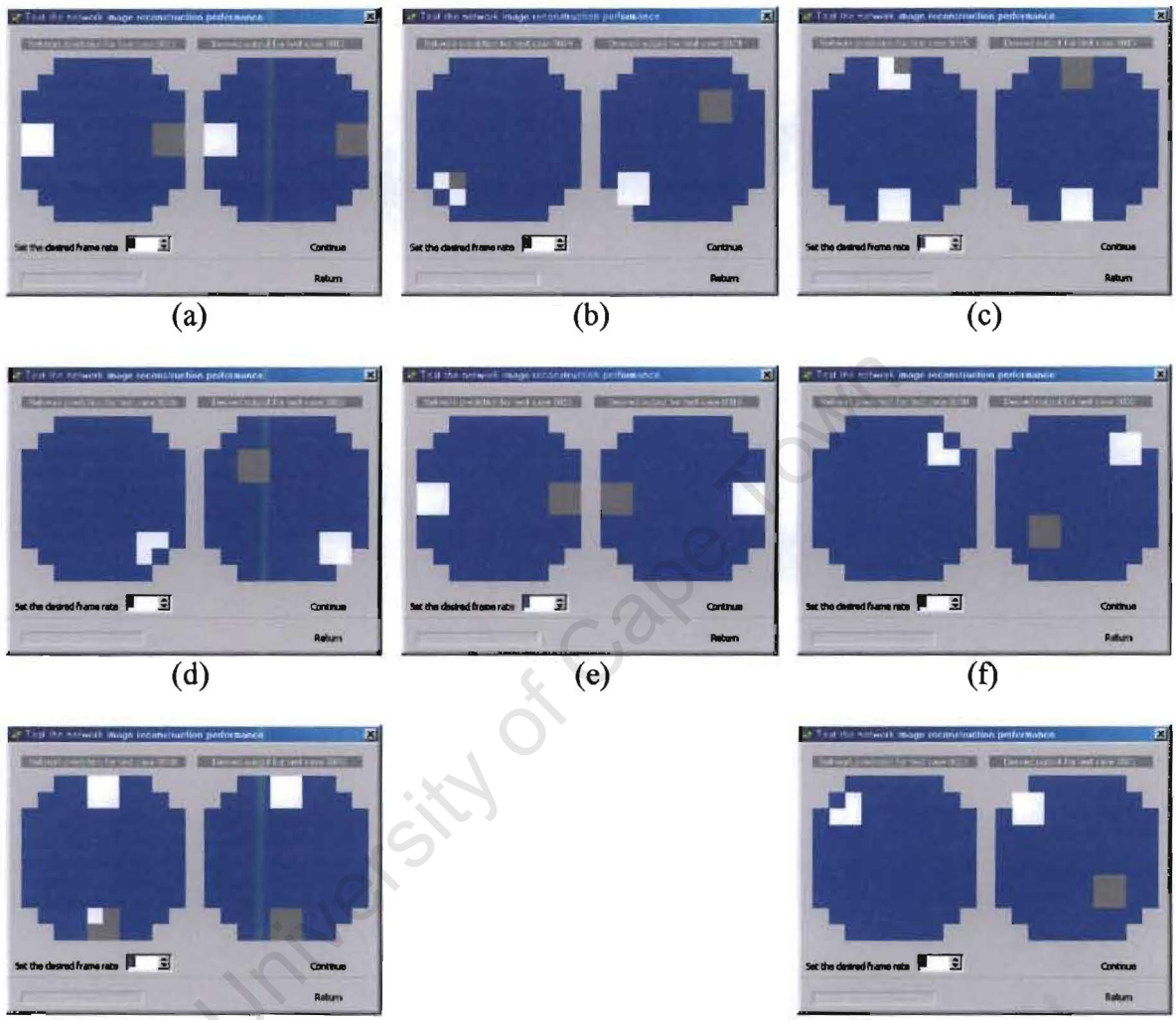

(a) (b) (c)

(d) (e) (f)

(g) (h)

Figure 7.10: Test case 1 for a three-phase air-gravel-seawater image reconstruction employing a single-layer feed-forward neural network using gradient descent.

2. Description

Test case 1 involves a small air-tube and a small gravel-bubble. The tube and bubble are placed directly opposite to each other. The air-tube is used as the reference phase and both are rotated anticlockwise around the vessel. As they are moved around the vessel both of they are placed in front of transmitters or in front of receivers alternatively starting with the air-tube positioned in front of TxA and the gravel-bubble in front of TxC.

TEST CASE 2

1. Results

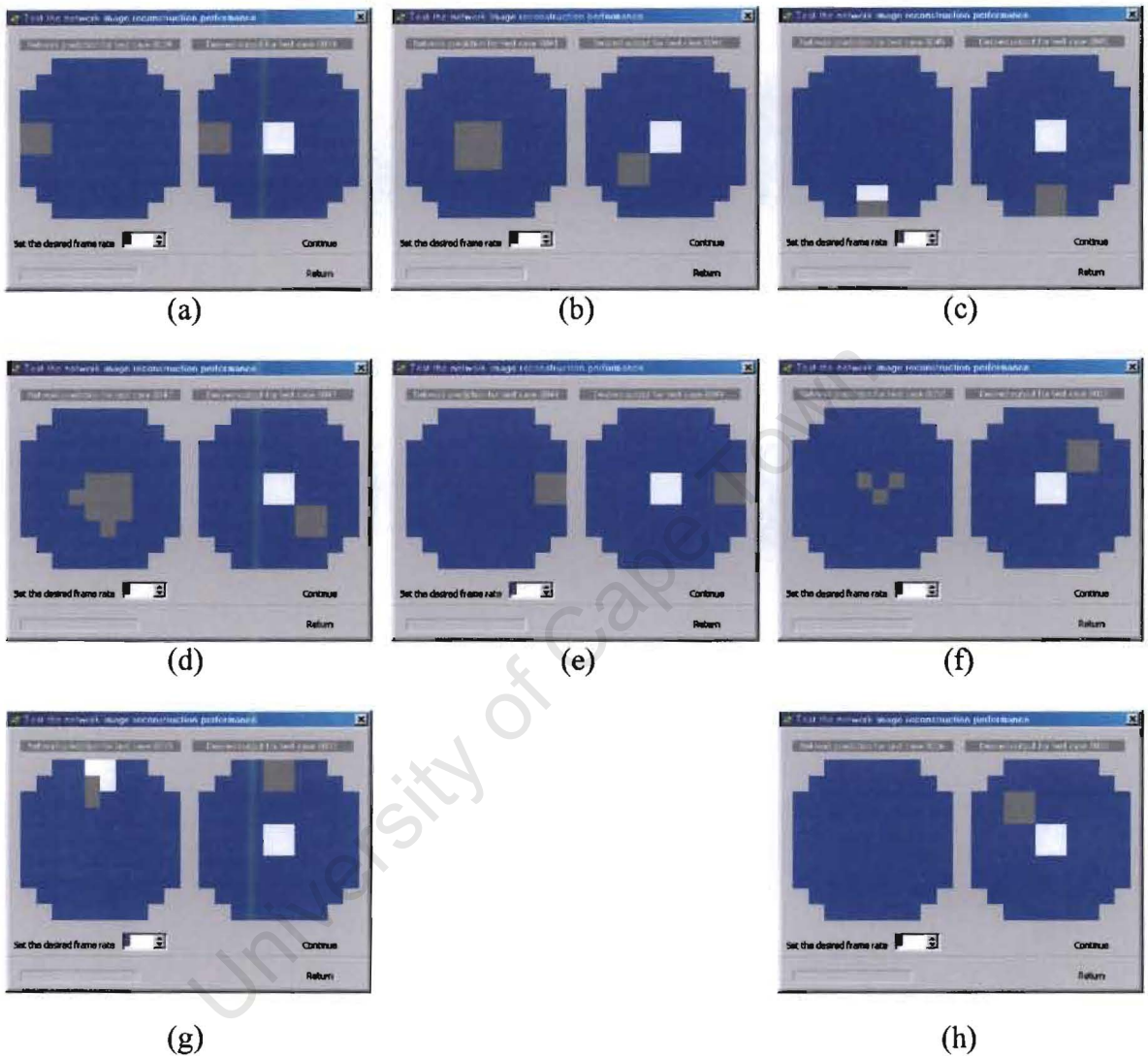

(a) (b) (c)

(d) (e) (f)

(g) (h)

Figure 7.11: Test case 2 for a three-phase air-gravel-seawater image reconstruction employing a single-layer feed-forward neural network using gradient descent.

2. Description

Test case 2 also involves a small air-tube and a small gravel-bubble each having a diameter of 45mm. The small air-tube is placed in the centre of the rig and the other one is rotated around the periphery of the vessel. In picture (a) it is placed in front of transmitter TxA, in (b) in front of receiver RxA, in (c) in front of transmitter TxB, in (d) in front of receivers RxB, in (e) in front of transmitter TxC, in (f) in front of receivers RxC and so on.

TEST CASE 3

1. Results

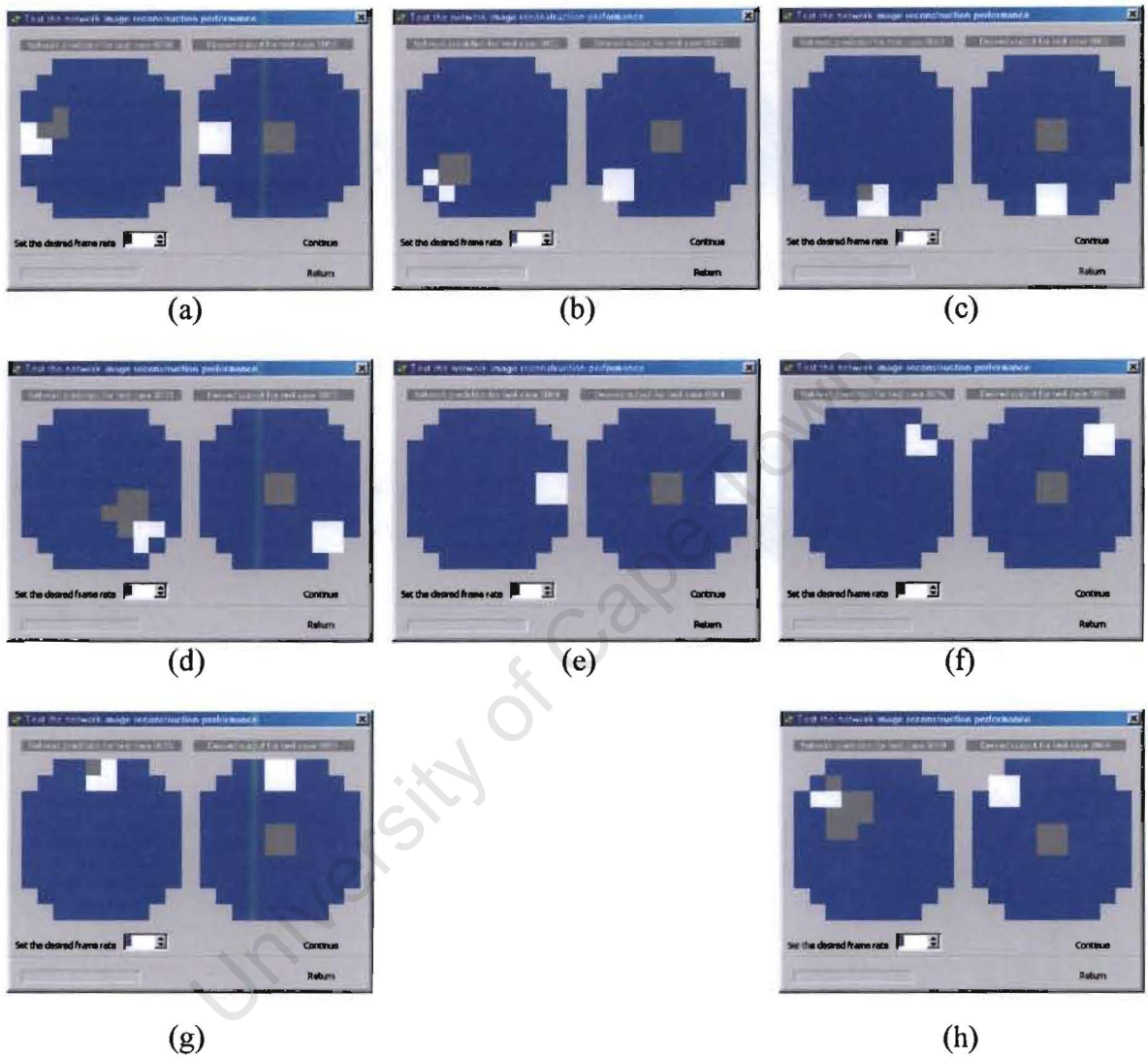

(a) (b) (c)

(d) (e) (f)

(g) (h)

Figure 7.12: Test case 3 for a three-phase air-gravel-seawater image reconstruction employing a single-layer feed-forward neural network using gradient descent.

2. Description

Test case 3 also involves a small air-tube and a small gravel-bubble each having a diameter of 45mm. In this case the small gravel-bubble is placed in the centre of the rig and the small air-tube is rotated around the periphery of the rig. In picture (a) the air-tube is placed in front of transmitter TxA, in (b) in front of receiver RxA, in (c) in front of transmitter TxB, in (d) in front of receivers RxB, in (e) in front of transmitter TxC and so on.

TEST CASE 4

1. Results

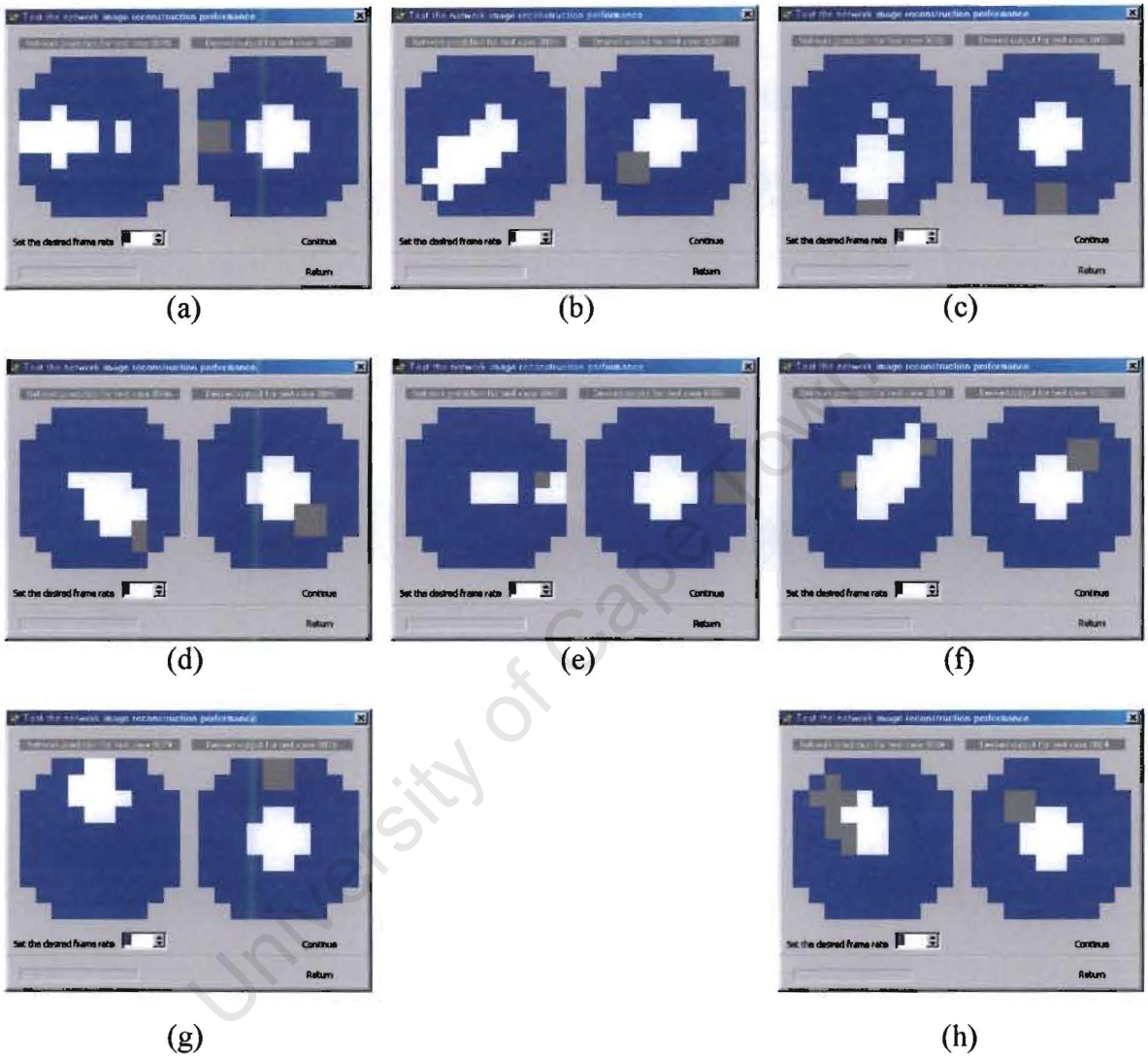

Figure 7.13: Test case 4 for a three-phase air-gravel-seawater image reconstruction employing a single-layer feed-forward neural network using gradient descent.

2. Description

Test case 4 involves one small gravel-bubble (45mm) and one big air-tube (90mm). The big air-tube is placed in the centre of the vessel and the small bubble is rotated around the periphery of the vessel. In picture (a) the gravel-bubble is placed in front of transmitter TxA, in (b) in front of receiver RxA, in (c) in front of transmitter TxB, in (d) in front of receivers RxB, in (e) in front of transmitter TxC, in (f) in front of receivers RxC and so on.

TEST CASE 5

1. Results

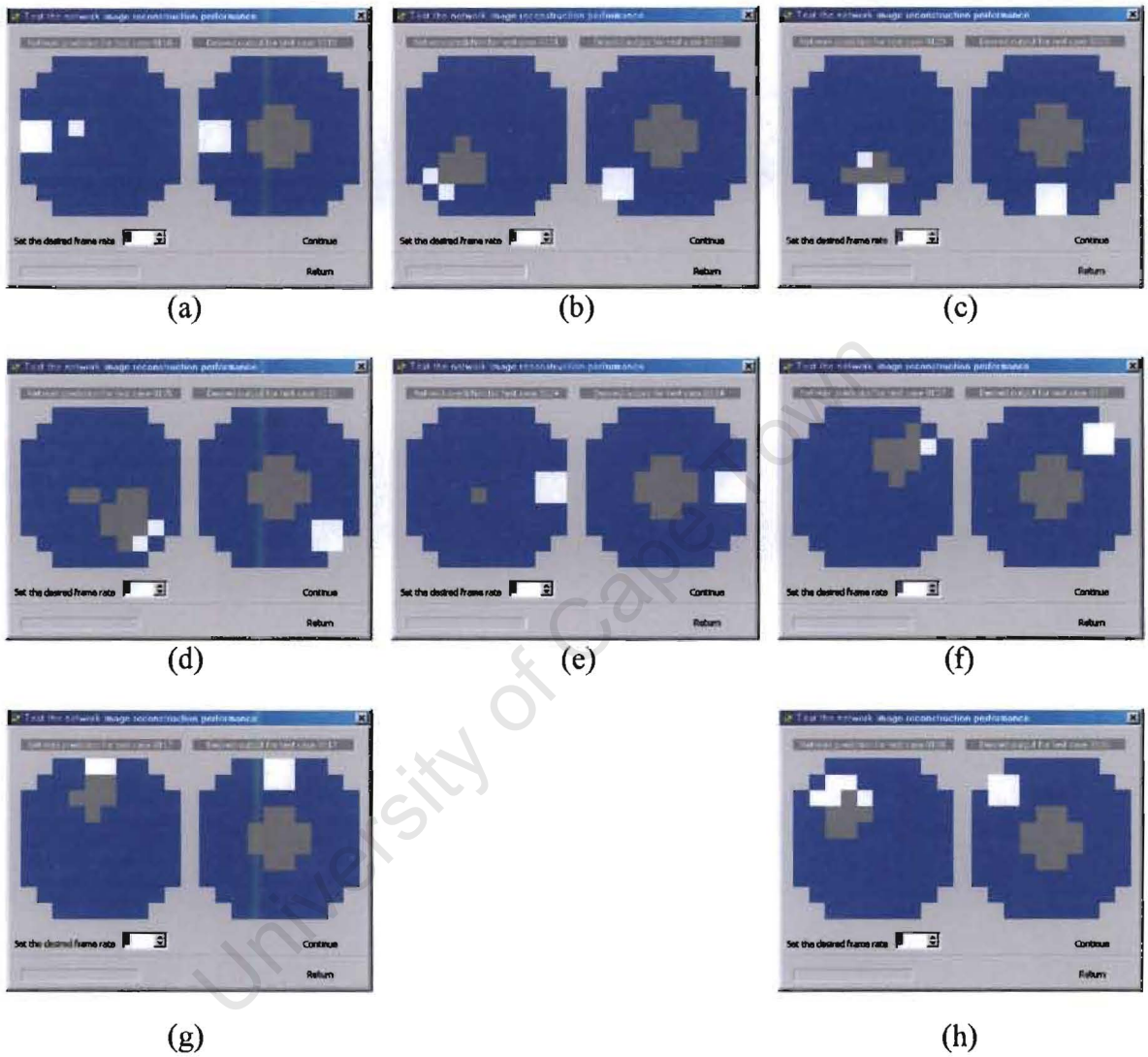

(a) (b) (c)

(d) (e) (f)

(g) (h)

Figure 7.14: Test case 5 for a three-phase air-gravel-seawater image reconstruction employing a single-layer feed-forward neural network using gradient descent.

2. Description

Test case 5 involves one small air-tube (45mm) and one big gravel-bubble (90mm). The big gravel-bubble is placed in the centre of the vessel and the small air-tube is rotated around the periphery of the rig. In picture (a) the air-tube is placed in front of transmitter TxA, in (b) in front of receiver RxA, in (c) in front of transmitter TxB, in (d) in front of receivers RxB, in (e) in front of transmitter TxC, in (f) in front of receivers RxC and so on.

TEST CASE 6

1. Results

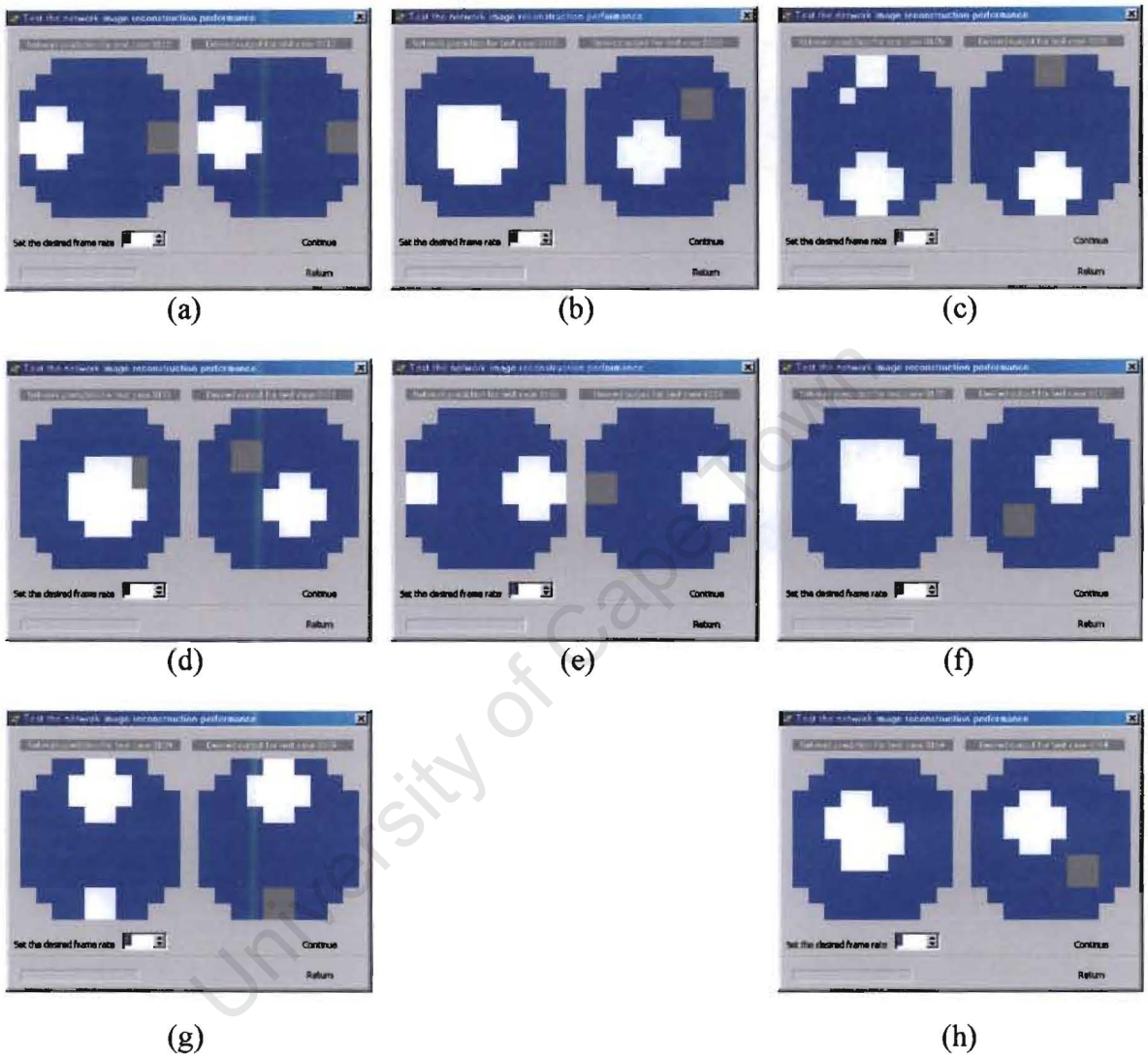

Figure 7.15: Test case 6 for a three-phase air-gravel-seawater image reconstruction employing a single-layer feed-forward neural network using gradient descent.

2. Description

Test case 6 involves a small gravel-bubble and a big air-tube. The tube and bubble are placed directly opposite to each other. The air-tube is used as the reference phase and both of them are rotated anticlockwise around the periphery of the vessel. As they move around the vessel both are placed in front of transmitters or receivers alternatively starting with the air-tube positioned in front of TxA and the gravel-bubble in front of TxC.

Test Case 7

1. Results

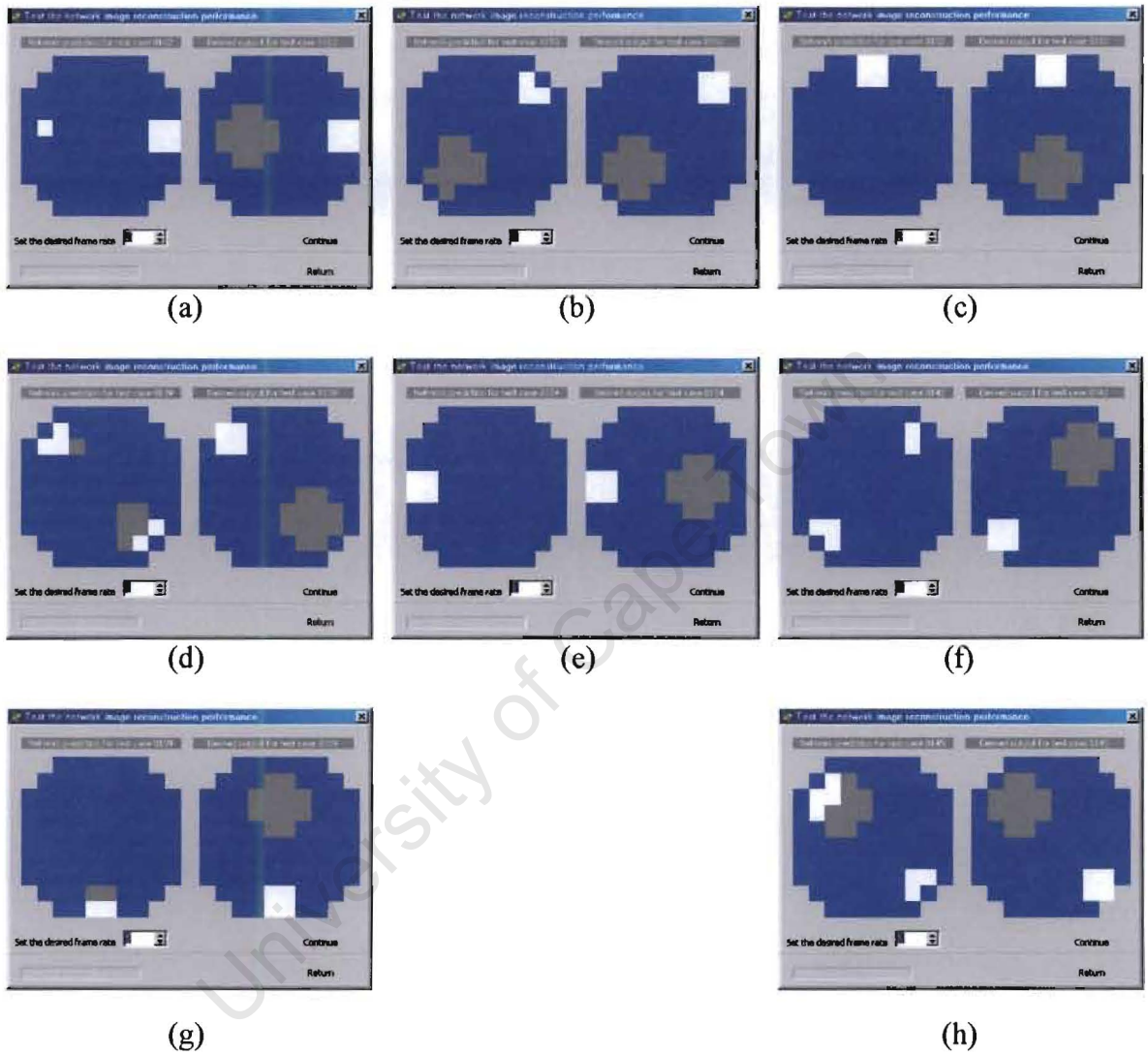

Figure 7.16: Test case 7 for a three-phase air-gravel-seawater image reconstruction employing a single-layer feed-forward neural network using gradient descent.

2. Description

Test case 7 involves a small air-tube and a big gravel-bubble. The tube and bubble are placed directly opposite to each other. The gravel-bubble is used as the reference phase and both of them are rotated anticlockwise around the vessel. As they are moved around the vessel both are placed in front of transmitters or receivers alternatively starting with the gravel-bubble positioned in front of TxA and the air-tube in front of TxC.

TEST CASE 8

1. Results

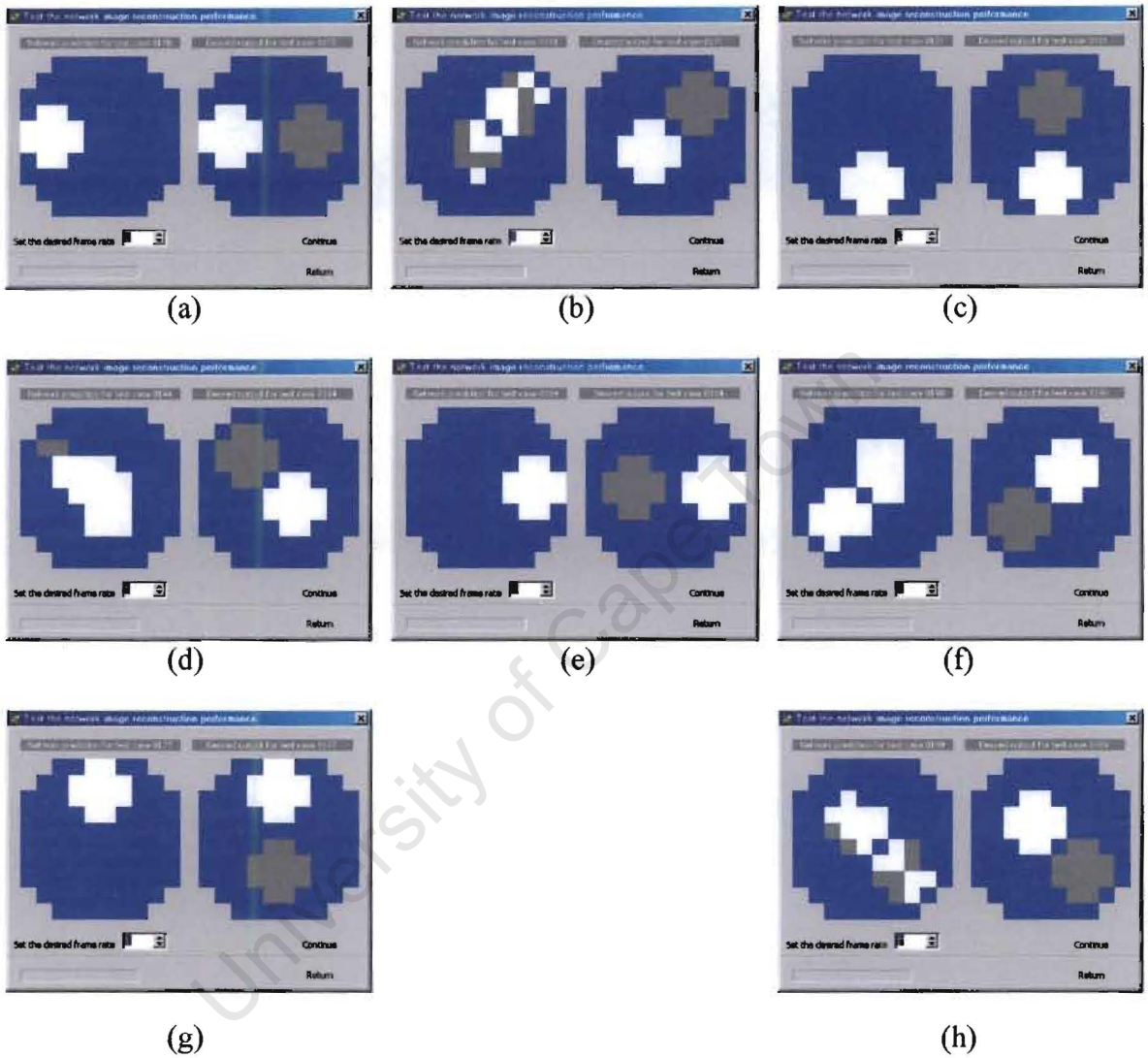

Figure 7.17: Test case 8 for a three-phase air-gravel-seawater image reconstruction employing a single-layer feed-forward neural network using gradient descent.

2. Description

Test case 8 involves a big air-tube and a big gravel-bubble. The tube and bubble are placed directly opposite to each other. The air-tube is used as the reference phase and both of them are rotated anticlockwise around the vessel. As they are moved around the vessel both are placed in front of transmitters or receivers alternatively starting with the air-tube positioned in front of TxA and the gravel-bubble in front of TxC.

7.2 Results using Neural Networks for Volume Fraction Predictions

This section deals with the system's performance by examining as a performance measure the volume fraction error predictions, obtained without performing image reconstruction of the rig's cross-section.

7.2.1 Two-Phase Cross-Sectional Image Reconstruction

This section provides the results that were obtained by employing the neural network to perform two-phase volume fraction predictions, with the rig containing seawater and air-tubes or seawater and gravel-bubbles.

7.2.1.1 Seawater-Air Image Reconstruction

A number of experiments testing various networks training configurations were done. The network was trained using both gradient descent and Resilient back-propagation. Since the neural network performance depends largely on the random initialization of the network's weights, five networks were trained and their results were averaged to give a more representative indication of the system's performance. Also, early stopping was employed, so that over-fitting would be prevented.

The best results were obtained using a single-layer feed-forward neural network, which was trained using gradient descent. This single-layer neural network was trained using the training data points containing only seawater and air components. The network consisted of 32 input neurons fully connected to 2 output neurons.

The neural network volume fraction prediction results are detailed in table 7.5 on the next page. The corresponding performance results of the electrical impedance tomography (EIT) system employing square-waves are not available.

As can be seen the volume fraction errors predicted by the neural networks directly without having to perform image reconstruction, outperform the ones predicted by the

neural networks that performed two-phase (air-seawater) image reconstruction.

PERFORMANCE MEASURE		IMPEDANCE TOMOGRAPHY SYSTEMS USING FREQUENCY DIVISION MULTIPLEXING	
		SQUARE-WAVE SYSTEM	SINE-WAVE SYSTEM
VOLUME FRACTION ERROR (%)	WATER	Not Available	3.692
	GRAVEL	Not Available	0.013
	AIR	Not Available	3.697
SUM VOLUME FRACTION ERROR (%)		Not Available	7.402

Table 7.5: The performances of the EIT system for a two-phase air-seawater volume Fraction prediction employing a single-layer feed-forward neural network using gradient descent.

7.2.1.2 Seawater-Gravel Image Reconstruction

After the completion of the tests, the results showed that a single-layer feed-forward neural network using gradient descent obtained good results. However, the results obtained by using a single-layer feed-forward neural network using Resilient back-propagation were equally good. As in the previous section for the seawater-air image reconstruction, here again five networks were trained and their results were averaged to give a more representative indication of the system's performance. Also, early stopping was employed, so that over-fitting would be prevented.

These single-layer neural networks were trained using the training data points containing only seawater and gravel components. The network consisted of 32 input neurons fully connected to 2 output neurons.

The neural network volume fraction prediction results are detailed in table 7.6 and 7.7 on the next page. The corresponding performance results of the electrical impedance tomography (EIT) system employing square-waves are not available.

PERFORMANCE MEASURE		IMPEDANCE TOMOGRAPHY SYSTEMS USING FREQUENCY DIVISION MULTIPLEXING	
		SQUARE-WAVE SYSTEM	SINE-WAVE SYSTEM
VOLUME FRACTION ERROR (%)	WATER	Not Available	1.064
	GRAVEL	Not Available	1.065
	AIR	Not Available	0.006
SUM VOLUME FRACTION ERROR (%)		Not Available	2.135

Table 7.6: The performances of the EIT system for a two-phase gravel-seawater volume fraction prediction using a single-layer feed-forward neural network employing gradient descent.

PERFORMANCE MEASURE		IMPEDANCE TOMOGRAPHY SYSTEMS USING FREQUENCY DIVISION MULTIPLEXING	
		SQUARE-WAVE SYSTEM	SINE-WAVE SYSTEM
VOLUME FRACTION ERROR(%)	WATER	Not Available	1.310
	GRAVEL	Not Available	1.310
	AIR	Not Available	0.00
SUM VOLUME FRACTION ERROR (%)		Not Available	2.620

Table 7.7: The performances of the EIT system for a two-phase gravel-seawater volume fraction prediction using a single-layer feed-forward neural network employing Resilient back-propagation.

As can be seen the volume fraction errors predicted by both neural networks directly without having to perform image reconstruction, once more outperform the ones predicted by the neural networks that performed two-phase (gravel-seawater) image reconstruction.

7.2.2 Three-Phase Cross-Sectional Image Reconstruction

After the completion of the tests, the results showed that the 45 layer feed-forward neural network using gradient descent obtained the best results (see table 7.9), even though Teague states in his Ph.D. thesis that a 25 layer feed-forward neural network using gradient descent was used to obtain his results (see table 7.8). As in the two-phase image reconstruction, again five networks were trained and their results were averaged to give a more representative indication of the system's performance. Also, early stopping was employed, so that over-fitting would be prevented.

This single-layer neural network was trained using the training data points containing air, gravel and seawater components. The network consisted of 32 input neurons fully connected to 2 output neurons.

The neural network reconstruction results are detailed in table 7.8 below, which also presents the corresponding performance results of the electrical impedance tomography (EIT) system employing square-waves. The white cells indicate which of the compared cell entries obtained a better performance. Table 7.9 on the next page, presents the best volume fraction predictions that were obtained by the author's system.

PERFORMANCE MEASURE		IMPEDANCE TOMOGRAPHY SYSTEMS USING FREQUENCY DIVISION MULTIPLEXING	
		SQUARE-WAVE SYSTEM	SINE-WAVE SYSTEM
VOLUME FRACTION ERROR (%)	WATER	4.799	3.825
	GRAVEL	4.713	4.539
	AIR	7.383	4.006
SUM VOLUME FRACTION ERROR (%)		16.895	12.370

Table 7.8: Comparison between the performances of two EIT systems for a three-phase air-gravel-seawater image reconstruction employing 25 layer feed-forward neural networks using gradient descent.

As can be seen the EIT system employing sine-waves once again outperforms the EIT system using square-waves in the volume fraction errors performance measure.

PERFORMANCE MEASURE		IMPEDANCE TOMOGRAPHY SYSTEMS USING FREQUENCY DIVISION MULTIPLEXING	
		SQUARE-WAVE SYSTEM	SINE-WAVE SYSTEM
VOLUME FRACTION ERROR (%)	WATER	Not Available	3.837
	GRAVEL	Not Available	4.340
	AIR	Not Available	3.779
SUM VOLUME FRACTION ERROR (%)		Not Available	11.956

Table 7.9: The performances of the EIT system for a three-phase air-gravel-seawater volume fraction prediction employing a 45 layer feed-forward neural network using gradient descent.

CHAPTER 8

8. CONCLUSIONS

Based on the results of this project, as well as the decisions taken during the designing period, the following conclusions are drawn.

- Errors that altered the performance, accuracy and stability, of the electrical impedance tomography (EIT) system using frequency division multiplexing (FDM) could be attributed to the following factors.
  - i) Inaccuracies introduced by the frequency generation modules of the system, causing the four sine-wave signals, used for synchronous detection of the signals relating to the capacitance paths formed in the vessel, not to be exactly 90^0 out of phase with their reference signals.
  - ii) Problems with the two electrode method employed by the EIT system to collect the resistance readings. As a result of the contact impedance (included in the measurements) formed between the resistance probes and the materials (air-gravel-seawater) being imaged, measurements were extremely sensitive to variations caused by the electrochemical reactions taking place within the vessel. Due to this, the resistance readings tended to drift over time.

- Even with the above mentioned weaknesses of the system, the readings (capacitance and resistance) were repeatable. As a result, it was possible to use the impedance tomography (EIT) system to perform two-phase (air-seawater or gravel-seawater) and three-phase (air-gravel-seawater) image reconstructions and volume fraction predictions.

- The multi-layer perceptron neural network was able to generalize for previously unseen combinations of the three phases (none of the data set combinations contained in the testing database were used in the training database), as well as for previously unseen air-tubes (half-round air-tube).

- Single-layer feed-forward neural networks using gradient descent obtained the best results for the threshold error and volume fraction error measures, while performing two-phase and three-phase image reconstruction. Single-layer feed-forward neural networks using gradient descent obtained the best volume fraction error results for a two-phase mixture. 45 layer feed-forward neural networks using gradient descent obtained the best volume fraction error results for a three-phase mixture, while no image reconstruction was performed.

- In general, better sum-of-error results were obtained when image reconstructions were not performed, and volume fractions were estimated directly.

- The electrical impedance tomography (EIT) system employing frequency division multiplexing (FDM) and injecting orthogonal frequency sine-waves in the measurement volume outperformed the EIT system employing FDM and injecting orthogonal frequency square-waves. This was true for both threshold error and volume fraction errors (comparison between the two systems was done whenever data was available), and with or without image reconstruction.

- An EIT system employing FDM and injecting orthogonal frequency sine-waves in the measurement volume should be used for future project developments, since the results obtained could be improved by taking into consideration all the designing electrode sensor information that was presented in Chapter 2. For example, attaining a better 2D electric field inside the area of interest and improving isolation between electrodes for minimum interference between the capacitance and resistance electrodes, as well as electromagnetic interference will improve the performance of the system.

CHAPTER 9

9. RECOMMENDATIONS

Based on the findings and conclusions of this project, the following recommendations are drawn.

- A new data collection protocol using frequency division multiplexing (FDM) and preferably employing a four-electrode adjacent pair measurement technique should be examined theoretically and practically. This will eliminate the problems associated with the two-electrode resistance measurement currently implemented by the EIT system.

- A new method of generating the sine-wave frequencies injected into the measurement volume should be investigated, so that the number of components used to make up the frequency generated modules could be reduced.

- An EIT system using frequency division multiplexing, injecting sine-waves in the rig and featuring a higher number of sensing electrodes should be used for future developments. That way cross-sectional reconstruction images with high resolution and better volume fraction predictions could be achieved.

- Dynamic flow situations, on line real-time data capture, as well as individual component velocities should be addressed using the above mentioned recommendations.

LIST OF REFERENCES

1. Q. Smit, "Material phase detection using capacitance tomography", MSc. Thesis, University of Cape Town, 2000
2. Q. Smit, J. Tapson and B.J.P. Mortimer, "Material phase detection system using capacitance tomography", Proc. IEEE-IMTC Conf., Baltimore, 2000
3. G. Teague, "Neural network reconstruction for electrical capacitance tomography system", BSc. Thesis, University of Cape Town, 2000
4. G. Teague, "Neural network reconstruction for tomography of a gravel-air-seawater mixture", Meas. Sci. Technol., Vol. **12** (2001), pp. 1102-1108
5. Z. Szczepanik and Z. Rucki, "Problems of the Data Acquisition Rate for Impedance Tomography", 2nd World Congress on Industrial Process Tomography, Hannover, 2001, pp. 511-516
6. N. Reinecke and D. Mewes, "Recent developments and industrial/research applications of capacitance tomography", Meas. Sci. Technol., Vol. **7** (1996), pp. 233-246
7. A. Arko, R.C. Waterfall, M.S. Beck, T. Dyakowski, P. Sutcliffe and M. Byars, "Development of Electrical Capacitance Tomography for Solids Mass Flow Measurement and Control of Pneumatic Conveying Systems", 1st World Congress on Industrial Process Tomography, Buxton, 1999, pp. 140-146
8. F.J. Dickin, B.S. Hoyle, A. Hunt, S.M. Huang, O. Ilyas, C. Lenn, R.C. Waterfall, R.A. Williams, C.G. Xie and M.S. Beck, "Tomographic imaging of industrial process equipment: techniques and applications", IEE Proc.-G, Vol. **139**, No. 1 (1992), pp. 72-81
9. X. Deng, F. Dong, L.J. Xu, X.P. Liu and L.A. Xu, "Measurement of the Gas Phase Velocity in Gas-Liquid Flows Using a Dual-Plane ERT System", 2nd World Congress on Industrial Process Tomography, Hannover, 2001, pp. 669-676
10. J. Chaouki, F. Larachi and M.P. Dudukovic, "Noninvasive Tomographic and Velocimetric Monitoring of Multiphase Flows", Ind. Eng. Chem. Res., Vol. **36** (1997), pp. 4476-4498

11. G.P. Lucas and N.D. Jin, "Measurement of the homogeneous velocity of inclined oil-in-water flows using a resistance cross correlation flow meter", Meas. Sci. Technol., Vol. **12** (2001), pp. 1529-1537
12. T. Dyakowski, "Process tomography applied to multi-phase flow measurement", Meas. Sci. Technol., Vol. **7** (1996), pp. 343-353
13. R.C. Waterfall, R. He, N.B. White and C.M. Beck, "Combustion imaging from electrical impedance measurements", Meas. Sci. Technol., Vol. **7** (1996), pp. 369-374
14. Ø. Isaksen, "A review of reconstruction techniques for capacitance tomography", Meas. Sci. Technol., Vol. **7** (1996), pp. 325-337
15. C.G. Xie, S.M. Huang, B.S. Hoyle, R. Thorn, C. Lenn, D. Snowden and M.S. Beck, "Electrical capacitance tomography for flow imaging: system model for development of image reconstruction algorithms and design of primary sensors", IEE Proc.-G, Vol. **139**, No. 1 (1992), pp. 89-98
16. W.Q. Yang and T.A. York, "New AC-based capacitance tomography system", IEE Proc.-Sci. Meas. Technol., Vol. **146**, No. 1 (1999), pp. 47-52
17. W.Q. Yang, A.L. Stott, M.S. Beck and C.G. Xie, "Development of capacitance tomographic imaging systems for oil pipeline measurements", Rev. Sci. Instrum., Vol. **66**, No. 8 (1995), pp. 4326-4332
18. W.Q. Yang, "Hardware design of electrical capacitance tomography systems", Meas. Sci. Technol., Vol. **7** (1996), pp. 225-232
19. N. Reinecke and D. Mewes, "Resolution enhancement for multi-electrode capacitance sensors", Proc. European Concerted Action on Process Tomography, Oporto, 1994, pp. 50-61
20. B.S. Hoyle, N.J. Bailey and A.Y. Nooralahiyan, "Performance of neural networks in capacitance-based tomographic process measurement systems", Measurement and Control, Vol. **28** (1995), pp. 109-112
21. C.G. Xie, A.L. Stott, A. Plaskowski and M.S. Beck, "Design of capacitance electrodes for concentration measurement of two-phase flow", Meas. Sci. Technol., Vol. **1** (1990), pp. 65-78
22. W.Q. Yang, "Calibration of capacitance tomography systems: a new method for setting system measurement range", Meas. Sci. Technol., Vol. **7** (1996), pp. 863-867

23. H. Xu, G. Yang and S. Wang, "Effect of Axial Guard Electrodes on Sensing Field of Capacitance Tomographic Sensor", 1st World Congress on Industrial Process Tomography, Buxton, 1999, pp. 348-352
24. Y. Ma, H. Wang, L.A. Xu and C. Jiang, "Simulation study of the electrode array used in an ERT system", Chemical Engineering Science, Vol. **52**, No. 13 (1997), pp. 2197-2203
25. Y. Ma, L.A. Xu and C. Jiang, "Experimental Study of the Guard Electrodes in an ERT System", 1st World Congr. on Industrial Process Tomography, Buxton, 1999, pp. 335-338
26. M. Wang, "Three-dimensional Effects in Electrical Impedance Tomography", 1st World Congress on Industrial Process Tomography, Buxton, 1999, pp. 410-415
27. W.Q. Yang, "Further developments in an ac-based capacitance tomography system", Rev. Sci. Instrum., Vol. **72**, No. 10 (2001), pp. 3902-3907
28. W.Q. Yang, "Advance in AC-based capacitance tomography system", 2nd World Congress on Industrial Process Tomography, Hannover, 2001, pp. 557-564
29. M. Byars, "Developments in Electrical Capacitance Tomography", 2nd World Congress on Industrial Process Tomography, Hannover, 2001, pp. 542-549
30. A.Y. Nooralahiyan and B.S. Hoyle, "Three-component tomographic flow imaging using artificial neural network reconstruction", Chemical Engineering Science, Vol. **52**, No. 13 (1997), pp. 2139-2148
31. A.Y. Nooralahiyan, B.S. Hoyle and N.J. Bailey, "Neural network for pattern association in electrical capacitance tomography", IEE Proc.-Circuits Devices Syst., Vol. **141**, No. 6 (1994), pp. 517-521
32. R. Thorn, G.A. Johansen and E.A. Hammer, "Three-Phase Flow Measurement in the Offshore Oil Industry Is There a Place for Process Tomography?", 1st World Congress on Industrial Process Tomography, Buxton, 1999, pp. 228-235
33. F. Dickin and M. Wang, "Electrical resistance tomography for process applications", Meas. Sci. Technol., Vol. 7 (1996), pp. 247-260
34. P.A.T. Pinheiro, W.W. Loh and F.J. Dickin, "Optimal sized electrodes for electrical resistance tomography", Electronics Letters, Vol. **34**, No. 1 (1998), pp. 69

35. M. Wang, F.J. Dickin and R.A. Williams, "Grouped-node technique as a means of handling large electrode surfaces in electrical impedance tomography", Physiol. Meas., Vol. **16** (1995)
36. W.W. Loh, F.J. Dickin, R.C. Waterfall and P.A.T. Pinheiro, "Alternative inter-plane data collection protocol for electrical resistance tomography in flow monitoring applications", Electronics Letters, Vol. **34**, No. 15 (1998), pp. 1487-1488
37. J.J. Cilliers, W. Xie, S.J. Neethling, E.W. Randall and A.J. Wilkinson, "Electrical resistance tomography using a bi-directional current pulse technique", Meas. Sci. Technol., Vol. **12** (2001), pp. 997-1001
38. F.J. Dickin, R.A. Williams and M.S. Beck, "Determination of composition and motion of multicomponent mixtures in process vessels using electrical impedance tomography – I. Principles and process engineering applications", Chemical Engineering Science, Vol. **48**, No. 10 (1993), pp. 1883-1897
39. M. Wang, F.J. Dickin and R.A. Williams, "Modelling and analysis of electrically conducting vessels and pipelines in electrical resistance process tomography", IEE Proc.-Sci. Meas. Technol., Vol. **42**, No. 4 (1995), pp. 313-320
40. E.L. Yuen, R. Mann, T.A. York and B.D. Grieve, "Electrical Resistance Tomography (ERT) Imaging of a Metal-Walled Solid-Liquid Filter', 2nd World Congress on Industrial Process Tomography, Hannover, 2001, pp. 183-190
41. W.W. Loh and F.J. Dickin, "Improved modified Newton-Raphson algorithm for electrical impedance tomography", Electronics Letters, Vol. **32**, No. 3 (1996), pp. 206-207
42. W.W. Loh, R.C. Waterfall, J. Cory and G.P. Lucas, "Using ERT for Multi-Phase Flow Monitoring", 1st World Congress on Industrial Process Tomography, Buxton, 1999, pp. 47-53
43. G.P. Lucas, J.C. Cory and R.C. Waterfall, "A six-electrode local probe for measuring solids velocity and volume fraction profiles in solids-water flows", Meas. Sci. Technol. Vol. **11** (2000), pp. 1498-1509
44. W.Q. Yang and K. Szuster, "A long-distance high-speed serial link for process tomography systems", Meas. Sci. Technol., Vol. 7 (1996), pp. 853-858

45. H.K.S. Lim and W.Q. Yang, "A Microcontroller-based High-speed Serial Link for Process Tomography Systems", 1st World Congress on Industrial Process Tomography, Buxton, 1999, pp. 377-382
46. T. Dyakowski, S.P. Luke, K.L. Ostrowski and R.A. Williams, "On-line monitoring of dense phase flow using real time dielectric imaging", Powder Technology, Vol. **104** (1999), pp. 287-295
47. D. Georgakopoulos, R.C, Waterfall and W.Q. Yang, "Towards the Development of a Multiple-Frequency ECT System", 2nd World Congress on Industrial Process Tomography, Hannover, 2001, pp. 550-556
48. P.J.W. Melsa, "Neural Networks: A Conceptual Overview", TRC-89-08, 1989, pp. 1-32
49. J.R. Greene, "EEE496S: Neural, Fuzzy and Evolving Systems", University of Cape Town, 1999.
50. A. Adler and R. Guardo, "A Neural Network Image Reconstruction Technique for Electrical Impedance Tomography", IEEE Trans. Med. Imag., Vol. **13**, No. 5 (1994), pp.594-560
51. T.D. Sun, R. Mudde, J.C. Schouten, B. Scarlett and C.M. van den Bleek, "Image Reconstruction of an Electrical Capacitance Tomography System Using an Artificial Neural Network", 1st World Congress on Industrial Process Tomography, Buxton, 1999, pp. 174-180
52. J.M. Saleh, B.S. Hoyle, F.J.Y. Podd and D.M. Spink, "Direct Flow Process Estimations From Tomographic Data Using Artificial Neural Systems", 2nd World Congress on Industrial Process Tomography, Hannover, 2001, pp. 751-758
53. G. Teague, "Mass flow measurement of multi-phase mixtures by means of tomographic techniques", Ph.D. Thesis, University of Cape Town, 2002
54. J.R. Greene, "EEE485F: Systematic Electronic Design Notes", University of Cape Town, 2000
55. E. Hervieu and Jr. P. Seleghim, "Direct Image of Two-Phase Flows by Electrical Impedance Measurements", 1st World Congress on Industrial Process Tomography, Buxton, 1999, pp. 62-69

56. S. Schrire, "EEE359W: Electronics, Components, Circuits and Modules Notes", University of Cape Town, 1999.
57. P. Horowitz and W. Hill, "The Art of Electronics", 2nd Edition, Cambridge University press, 1995
58. Eagle Technology, "User Manual for Dos and Windows", EDR Software developers kit for Eagle Technology Boards, 1999

APPENDIX A

MICROCONTROLLER PROGRAM CODES FOR AN 8-ELECTRODE FDM EIT SYSTEM

1. **Program Code Description:** Generating a 24.375kHz Sine-Wave using a 16.38MHz Crystal

```
INCLUDE REG84.H
; Initialization Routine.
        ; Select Page 1.
Init    BSF   STATUS,RP0
        ; Set PortA to Outputs.
        CLRF TRISA
        ; Set PortB to Outputs.
        CLRF TRISB
        ; Select Page 0.
        BCF   STATUS,RP0
        ; Clear PortA.
        CLRF PORTA
; 1st Component.
Start   MOVLW D'128'
        MOVWF PORTB
        BSF       PORTA,0
        MOVLW D'255'
        MOVWF PORTB
        BCF       PORTA,0
        NOP
        NOP
        NOP
        NOP
        NOP
        NOP
        NOP
        NOP
        NOP
        NOP
        NOP
        NOP
        NOP
        NOP
        NOP
        NOP
; 2nd Component.
        MOVLW D'192'
        MOVWF PORTB
        BSF       PORTA,0
        MOVLW D'192'
        NOP
        NOP
        NOP
        NOP
        NOP
        NOP
        NOP
        NOP
        NOP
        NOP
        NOP
        NOP
        NOP
        NOP
        NOP
        NOP
; 3rd Component.
        MOVLW D'255'
        MOVWF PORTB
        BSF       PORTA,0
        MOVLW D'128'
        MOVWF PORTB
        BCF       PORTA,0
        NOP
        NOP
        NOP
        NOP
        NOP
        NOP
        NOP
        NOP
        NOP
        NOP
        NOP
        NOP
        NOP
        NOP
        NOP
        NOP
; 4th Component.
        MOVLW D'192'
        MOVWF PORTB
        BSF       PORTA,0
        MOVLW D'64'
        MOVWF PORTB
        BCF       PORTA,0
        NOP
        NOP
        NOP
        NOP
        NOP
        NOP
        NOP
        NOP
        NOP
        NOP
        NOP
        NOP
        NOP
        NOP
        NOP
        NOP
; 5th Component.
        MOVLW D'128'
        MOVWF PORTB
        BSF       PORTA,0
        MOVLW D'0'
        MOVWF PORTB
        BCF       PORTA,0
        NOP
        NOP
        NOP
        NOP
        NOP
        NOP
        NOP
        NOP
        NOP
        NOP
        NOP
        NOP
        NOP
        NOP
        NOP
        NOP
; 6th Component.
        MOVLW D'64'
        MOVWF PORTB
        BSF       PORTA,0
        MOVLW D'64'
        MOVWF PORTB
```

```
        BCF     PORTA,0
        NOP
        NOP
        NOP
        NOP
        NOP
        NOP
        NOP
        NOP
        NOP
        NOP
        NOP
        NOP
        NOP
        NOP
; 7th Component.
        MOVLW D'0'
        MOVWF PORTB
        BSF     PORTA,0
        MOVLW D'128'
        MOVWF PORTB
        BCF     PORTA,0
        NOP
        NOP
        NOP
        NOP
        NOP
        NOP
        NOP
        NOP
        NOP
        NOP
        NOP
        NOP
; 8th Component.
        MOVLW D'64'
        MOVWF PORTB
        BSF     PORTA,0
        MOVLW D'192'
        MOVWF PORTB
        BCF     PORTA,0
        NOP
        NOP
        NOP
        NOP
        NOP
        NOP
        NOP
        NOP
        NOP
        NOP
        NOP
        NOP
        GOTO    Start

        END
```

2. Program Code Description: Generating a 37.5kHz Sine wave using a 12MHz Crystal.

```
INCLUDE REG84.H
; Initialization Routine.
        ; Select Page 1.
Init    BSF   STATUS,RP0
        ; Set PortA to Outputs.
        CLRF TRISA
        ; Set PortB to Outputs.
        CLRF TRISB
        ; Select Page 0.
        BCF   STATUS,RP0
        ; Clear PortA.
        CLRF PORTA
; 1st Component.
Start   MOVLW D'128'
        MOVWF PORTB
        BSF     PORTA,0
        MOVLW D'255'
        MOVWF PORTB
        BCF     PORTA,0
        NOP
        NOP
        NOP
        NOP
; 2nd Component.
        MOVLW D'192'
        MOVWF PORTB
        BSF     PORTA,0
        MOVLW D'192'
        MOVWF PORTB
        BCF     PORTA,0
        NOP
        NOP
        NOP
        NOP
; 3rd Component.
        MOVLW D'255'
        MOVWF PORTB
        BSF     PORTA,0
        MOVLW D'128'
        MOVWF PORTB
        BCF     PORTA,0
        NOP
        NOP
        NOP
        NOP
; 4th Component.
        MOVLW D'192'
        MOVWF PORTB
        BSF     PORTA,0
        MOVLW D'64'
        MOVWF PORTB
        BCF     PORTA,0
        NOP
        NOP
        NOP
        NOP
; 5th Component.
        MOVLW D'128'
        MOVWF PORTB
        BSF     PORTA,0
        MOVLW D'0'
        MOVWF PORTB
        BCF     PORTA,0
        NOP
        NOP
        NOP
        NOP
; 6th Component.
        MOVLW D'64'
        MOVWF PORTB
        BSF     PORTA,0
        MOVLW D'64'
        MOVWF PORTB
        BCF     PORTA,0
        NOP
        NOP
        NOP
        NOP
; 7th Component.
        MOVLW D'0'
        MOVWF PORTB
        BSF     PORTA,0
        MOVLW D'128'
        MOVWF PORTB
        BCF     PORTA,0
        NOP
        NOP
        NOP
        NOP
; 8th Component.
        MOVLW D'64'
        MOVWF PORTB
        BSF     PORTA,0
```

```
        MOVLW D'192'
        MOVWF PORTB
        BCF   PORTA,0
        NOP
        NOP
        GOTO  Start

        END
```

3. Program Code Description: Generating a 39.375kHz Sine wave using a 16.38MHz Crystal.

```
INCLUDE REG84.H
; Initialization Routine.
        ; Select Page 1.
Init    BSF   STATUS,RP0
        ; Set PortA to Outputs.
        CLRF TRISA
        ; Set PortB to Outputs.
        CLRF TRISB
        ; Select Page 0.
        BCF   STATUS,RP0
        ; Clear PortA.
        CLRF PORTA
; 1st Component.
Start   MOVLW D'128'
        MOVWF PORTB
        BSF   PORTA,0
        MOVLW D'255'
        MOVWF PORTB
        BCF   PORTA,0
        NOP
        NOP
        NOP
        NOP
        NOP
        NOP
        NOP
; 2nd Component.
        MOVLW D'192'
        MOVWF PORTB
        BSF   PORTA,0
        MOVLW D'192'
        MOVWF PORTB
        BCF   PORTA,0
        NOP
        NOP
        NOP
        NOP
        NOP
        NOP
        NOP
; 3rd Component.
        MOVLW D'255'
        MOVWF PORTB
        BSF   PORTA,0
        MOVLW D'128'
        MOVWF PORTB
        BCF   PORTA,0
        NOP
        NOP
        NOP
        NOP
        NOP
        NOP
        NOP
; 4th Component.
        MOVLW D'192'
        MOVWF PORTB
        BSF   PORTA,0
        MOVLW D'64'
        MOVWF PORTB
        BCF   PORTA,0
        NOP
        NOP
        NOP
        NOP
        NOP
        NOP
        NOP
; 5th Component.
        MOVLW D'128'
        MOVWF PORTB
        BSF   PORTA,0
        MOVLW D'0'
        MOVWF PORTB
        BCF   PORTA,0
        NOP
        NOP
        NOP
        NOP
        NOP
        NOP
        NOP
; 6th Component.
        MOVLW D'64'
        MOVWF PORTB
        BSF   PORTA,0
        MOVLW D'64'
        MOVWF PORTB
        BCF   PORTA,0
        NOP
        NOP
        NOP
        NOP
        NOP
        NOP
        NOP
; 7th Component.
        MOVLW D'0'
        MOVWF PORTB
        BSF   PORTA,0
        MOVLW D'128'
        MOVWF PORTB
        BCF   PORTA,0
        NOP
        NOP
        NOP
        NOP
        NOP
        NOP
        NOP
; 8th Component.
        MOVLW D'64'
        MOVWF PORTB
        BSF   PORTA,0
        MOVLW D'192'
        MOVWF PORTB
        BCF   PORTA,0
        NOP
        NOP
        NOP
        NOP
        NOP
        GOTO  Start

        END
```

4. Program Code Description: Generating a 46.875kHz Sine wave using a 12MHz Crystal.

```
INCLUDE REG84.H
; Initialization Routine.
        ; Select Page 1.
Init    BSF   STATUS,RP0
        ; Set PortA to Outputs.
        CLRF TRISA
        ; Set PortB to Outputs.
        CLRF TRISB
        ; Select Page 0.
        BCF   STATUS,RP0
        ; Clear PortA.
        CLRF PORTA
; 1st Component.
Start   MOVLW D'128'
        MOVWF PORTB
        BSF     PORTA,0
        MOVLW D'255'
        MOVWF PORTB
        BCF     PORTA,0
        NOP
        NOP
; 2nd Component.
        MOVLW D'192'
        MOVWF PORTB
        BSF     PORTA,0
        MOVLW D'192'
        MOVWF PORTB
        BCF     PORTA,0
        NOP
        NOP
; 3rd Component.
        MOVLW D'255'
        MOVWF PORTB
        BSF     PORTA,0
        MOVLW D'128'
        MOVWF PORTB
        BCF     PORTA,0
        NOP
        NOP
; 4th Component.
        MOVLW D'192'
        MOVWF PORTB
        BSF     PORTA,0
        MOVLW D'64'
        MOVWF PORTB
        BCF     PORTA,0
        NOP
        NOP
; 5th Component.
        MOVLW D'128'
        MOVWF PORTB
        BSF     PORTA,0
        MOVLW D'0'
        MOVWF PORTB
        BCF     PORTA,0
        NOP
        NOP
; 6th Component.
        MOVLW D'64'
        MOVWF PORTB
        BSF     PORTA,0
        MOVLW D'64'
        MOVWF PORTB
        BCF     PORTA,0
        NOP
        NOP
; 7th Component.
        MOVLW D'0'
        MOVWF PORTB
        BSF     PORTA,0
        MOVLW D'128'
        MOVWF PORTB
        BCF     PORTA,0
        NOP
        NOP
; 8th Component.
        MOVLW D'64'
        MOVWF PORTB
        BSF     PORTA,0
        MOVLW D'192'
        MOVWF PORTB
        BCF     PORTA,0
        GOTO    Start

        END
```

APPENDIX B

PBIL OPTIMISATION ALGORITHM

The following application performs PBIL to determine the set of optimal frequencies for an 8-electrode FDM EIT system. The program uses all the standard crystal frequencies and all division factors that can be programmed in the PIC16F84A to determine a set of possible frequencies between 15kHz and 78.125kHz.

```
unit pbilform;

interface

uses
  Windows, Messages, SysUtils, Classes, Graphics,
  Controls, Forms, Dialogs, StdCtrls, Math, ComCtrls, Spin;

type
  TPBILMain = class(TForm)
    LoadFreqs: TButton;
    Label1: TLabel;
    Label2: TLabel;
    MaxGenerations: TSpinEdit;
    NumTrials: TSpinEdit;
    PBILStart: TButton;
    PBILProgress: TProgressBar;
    Freq1: TLabel;
    Freq2: TLabel;
    Freq3: TLabel;
    Freq4: TLabel;
    Freq5: TLabel;
    Freq6: TLabel;
    Freq7: TLabel;
    Freq8: TLabel;
    Label3: TLabel;
    BestFreqFit: TLabel;
    MultiSearchPBIL: TButton;
    Label4: TLabel;
    NumIterations: TSpinEdit;
    Label5: TLabel;
    CurIterCaption: TLabel;
    Label6: TLabel;
    OverBestFreqFit: TLabel;
    OverFreq5: TLabel;
    OverFreq6: TLabel;
    OverFreq7: TLabel;
    OverFreq8: TLabel;
    OverFreq1: TLabel;
    OverFreq2: TLabel;
    OverFreq3: TLabel;
    OverFreq4: TLabel;
    SaveMultiRecord: TSaveDialog;
    ShowResults: TListBox;
    procedure LoadFreqsClick(Sender: TObject);
    proeedure FormShow(Sender: TObject);
     procedure PBILStartClick(Sender: TObject);
    procedure MultiSearchPBILClick(Sender: TObject);
private
{ Private declarations }
    xtal : array[1..23] of double; //standard crystal frequencies
    AvailFreq : array[1..1288] of double; //available frequencies
    ReevFreq : array[1..2000] of double; //received frequencies
    MultOutFreqs : array[1..20000] of double; //multiplier output
                                              frequencies
    resrecord : array[1..9,1..100] of double; //record of results
    ntrials : integer;
    maxgen : integer;
    besteverfit : double;
    besteverreal : array[1..8] of double;
    function MultOut(inputs:array of double):double;
  public
    { Public declarations }
  end;

var
  PBILMain: TPBILMain;
implementation
{$R *.DFM}

procedure QSort(var X : array of double; Lbound, Ubound : Integer);
{ Quick sort in ascending order - Adapted from Borland's BP7 demo }
  procedure Sort(L, R : Integer);
  var
    I, J : integer;
    U, V : extended;
  begin
    I := L;
    J := R;
    U := X[(L + R) div 2];
    repeat
      while X[I] < U do I := I + 1;
      while U < X[J] do J := J - 1;
      if I <= J then
        begin
          V := X[I]; X[I] := X[J]; X[J] := V;
          I := I + 1; J := J - 1;
        end;
    until I > J;
    if L < J then Sort(L, J);
    if I < R then Sort(I, R);
  end;
begin
  Sort(Lbound, Ubound);
end;

//-------------Frequency Simulation Procedures-------------//
//Generate a list of all available transmitter frequencies
procedure TPBILMain.LoadFreqsClick(Sender: TObject);
var
  i,j,k, Nops: integer;
  TempFreq : array[1..1288] of double;
  begin
  i:= 1;
  Nops:= 0;
  while i<=1288 do
  begin
    for j:= 1 to 23 do
    begin
    for j:= 1 to 23 do
    begin
      TempFreq[i]:= 1/(8*(Nops+8)*(4/xtal[j]));
      Inc(i);
    end;
    Inc(Nops);
  end;
  i:= 1;
  j:= 1;
  while i<= 1288 do
```

```
 begin
  if ((TempFreq[i]>= 15e3) and (TempFreq[i]<= 80e3)) then
  begin
   AvailFreq[j]:= TempFreq[i];
   Inc(j);
  end;
  Inc(i);
 end;

 QSort(AvailFreq,0,j-2);

 k:= 1;
 for i:= 1 to j-1 do
  if (AvailFreq[i] <> AvailFreq[i+1]) then
  begin
   TempFreq[k]:= AvailFreq[i];
   inc(k);
  end;

 for i:= k to 1288 do
  TempFreq[i]:= 0;

 for i:= 1 to 1288 do
  AvailFreq[i]:= TempFreq[i];

 for i:= 1 to k-1 do
  ShowResults.Items.Add(inttostr(i)+' '+floattostr(AvailFreq[i]));
end;

//Setup array of all standard crystal frequencies.
procedure TPBILMain.FormShow(Sender: TObject);
begin
 xtal[1] := 1e6;
 xtal[2] := 1.6384e6;
 xtal[3] := 1.8432e6;
 xtal[4] := 2e6;
 xtal[5] := 2.4576e6;
 xtal[6] := 3e6;
 xtal[7] := 3.2768e6;
 xtal[8] := 3.579545e6;
 xtal[9] := 3.6864e6;
 xtal[10] := 4e6;
 xtal[11] := 4.43361e6;
 xtal[12] := 5e6;
 xtal[13] := 5.068e6;
 xtal[14] := 6e6;
 xtal[15] := 6.144e6;
 xtal[16] := 8e6;
 xtal[17] := 8.867238e6;
 xtal[18] := 10e6;
 xtal[19] := 11.0592e6;
 xtal[20] := 12e6;
 xtal[21] := 16e6;
 xtal[22] := 16.38e6;
 xtal[23] := 20e6;
end;

{Calculate the minimum frequency component of the LPF outputs
by simulating the mixing in the synchronous detectors. }
function TPBILMain.MultOut(inputs:array of double):double;
var a,b,c,d,e,f: integer;
   RefFreq: double;
   RefHarm: array [1..4] of double;
   diffrec: array [0..7] of double;
   TempStore: array [1..1000] of double;
begin
//Sort out my input frequencies (from the smallest to the biggest).
 Qsort(inputs,0,7);

//Check if there are any duplicates and triplicates.
 for a:= 0 to 6 do
   for c:= a+1 to 7 do
    if ((inputs[a]= inputs[c]) Or (2*inputs[a]= inputs[c])
                    Or (3*inputs[a]= inputs[c])) then
    begin
     MultOut := 0;
     exit;
    end;

//Noise from ground planes on the SG-Boards.
 RecvFreq[1]:= 0;

//Fundamental frequencies and their 2nd and 3rd harmonics.
 b:= 2;
 for c:= 1 to 3 do
  for a:= 0 to 7 do
  begin
   RecvFreq[b]:= inputs[a]*c;
   inc(b);
  end;

//Frequencies occurred due to a chemical reaction in the sea water.
 for a:= 0 to 6 do
  for c:= a+1 to 7 do
  begin
   RecvFreq[b]:= inputs[c]-inputs[a];
   Inc(b);

   for e:=0 to 7 do
   begin
    RecvFreq[b]:= Abs(inputs[e]-(inputs[c]-inputs[a]));
    Inc(b);
    RecvFreq[b]:= inputs[e]+(inputs[c]-inputs[a]);
    Inc(b);
   end;

RecvFreq[b]:= inputs[c]+inputs[a];
   Inc(b);
   for e:=0 to 7 do
   begin
    RecvFreq[b]:= Abs(inputs[e]-(inputs[c]+inputs[a]));
    Inc(b);
    RecvFreq[b]:= inputs[e]+(inputs[c]+inputs[a]);
    Inc(b);
   end;
  end;
//Sort out my input frequencies (from the smallest to the biggest).
 QSort(RecvFreq,0,b-2);
//Get reed off frequencies that are the same.
 for c:= 1 to 1000 do
  TempStore[c]:= 0;
   c:= 1;
 for a:= 1 to 980 do
 begin
  if RecvFreq[a]<> RecvFreq[a+1] then
  begin
   TempStore[c]:= RecvFreq[a];
   Inc(c);
  end;
 end;

 for a:= 1 to 2000 do
  RecvFreq[a]:= 0;
 for a:= 1 to c-1 do
  RecvFreq[a]:= TempStore[a];

//Get reed off frequencies above 100kHz.
 e:= 1;
 for a:= 1 to c-1 do
 begin
  if (RecvFreq[a]> 150e3) then
  begin
   RecvFreq[a] := 0;
   if (e = 1) then
    e:= a;
  end;
 end;
 if e= 1 then
  e:= c;

//Generate Reference frequencies.
 for a := 0 to 7 do
 begin
  RefFreq := inputs[a];
  RefHarm[1] := 0;

  c := 1;
  for b:= 2 to 4 do
```

```
  begin
    RefHarm[b] := RefFreq*c;
    Inc(c);
  end;

  d := 1;
  for c := 1 to 4 do
    for b := 1 to (c - 1) do
    begin
      MultOutFreqs[d] := RefHarm[c]+RecvFreq[b];
      Inc(d);
      MultOutFreqs[d] := Abs(RefHarm[c]-RecvFreq[b]);

      Inc(d);
    end;

  Qsort(MultOutFreqs,0,d-2);
  diffrec[a] := MultOutFreqs[6];
 end;

//Sort out my input frequencies (from the smallest to the biggest).
 Qsort(diffrec,0,7);

//Send the smallest back.
 MultOut := diffrec[0];
end;

{Perform PBIL to determine optimal set of transmitter
frequencies for an 8-electrode FDM EIT system.}
procedure TPBILMain.PBILStartClick(Sender: TObject);
var nvars, prec, g, trial, i,j,k : integer;
   bestfit, fit : real;
   bw : array[1..8] of integer;
   PV : array[1..64] of real;
   R : array[1..8] of integer;
   bestreal : array[1..8] of double;
   trialsol : array[1..64] of short;
   bestsol : array[1..64] of short;
   besteversol : array[1..64] of short;
   inputs : array[1..8] of double;
begin
     PBILStart.Caption:= 'Busy Sampling';
     PBILStart.Refresh;
     Randomize;  //initialize random number generator
     ntrials := NumTrials.Value;
     maxgen := MaxGenerations.Value;
     PBILProgress.Position := 0;
     PBILProgress.Max := maxgen + 1;
     nvars := 8;  //number of variables
     prec := 8;  //8-bit precision
     besteverfit := -1;  //record best results

     //Calculate the bit weight.
     for g := 0 to prec-1 do
          bw[g+1] := floor(power(2,g));
     //Initialize the probability vector.
     for g := 1 to prec*nvars do
          PV[g] := 0.5;

     for g := 1 to maxgen do
     begin
          PBILProgress.StepIt;
          bestfit := -1;
          for trial := 1 to ntrials do

          begin
               //Generate random trial solution.
               for i:= 1 to (prec*nvars) do
                    trialsol[i] := short(PV[i] > Random);

               //Convert the sequence of bits into integer values.
               k := 1;
               for i:= 1 to nvars do

               begin
                    R[i] := 0;
                    for j := 1 to prec do
                    begin
                         R[i] := R[i]+trialsol[k]*bw[j];
                         inc(k);
                    end;
               end;

               //Use these 8 integer values as index values in
                 //in the array
               for i := 1 to nvars do
                    inputs[i] := AvailFreq[R[i]+1];
               //Test current set of frequencies
               fit := MultOut(inputs);
                 //If the performance is the best do far for this
                 //generation then update the record.
               if fit > bestfit then
               begin
                    bestfit := fit;
                    for i:= 1 to (nvars*prec)do
                    begin
                      bestsol[i] := trialsol[i];
                      if (i<=nvars) then
                        bestreal[i] := inputs[i];
                    end;
               end;
          end;
           //Using the best solution, adjust the probability vector
           //towards the best solution.
          for i:=1 to (prec*nvars) do
          begin
               PV[i] := 0.9*PV[i]+0.1*bestsol[i];
               PV[i] := PV[i]-0.005*(PV[i]-0.5);
          end;
           //Keep record of the best overall results.
          if bestfit > besteverfit then
          begin
               besteverfit := bestfit;
               for i:= 1 to (nvars*pree)do
               begin
                 besteversol[i] := bestsol[i];
                 if (i<=nvars) then
                   besteverreal[i] := bestreal[i];
               end;
             BestFreqFit.Caption:=floattostrf(besteverfit,ffFixed,15,4);
               Qsort(besteverreal,0,7);
               Freq1.Caption:=floattostrf(besteverreal[1],ffFixed,15,4);
               Freq2.Caption:=floattostrf(besteverreal[2],ffFixed,15,4);
               Freq3.Caption:=floattostrf(besteverreal[3],ffFixed,15,4);
               Freq4.Caption:=floattostrf(besteverreal[4],ffFixed,15,4);
               Freq5.Caption:=floattostrf(besteverreal[5],ffFixed,15,4);
               Freq6.Caption:=floattostrf(besteverreal[6],ffFixed,15,4);
               Freq7.Caption:=floattostrf(besteverreal[7],ffFixed,15,4);
               Freq8.Caption:=floattostrf(besteverreal[8],ffFixed,15,4);
          end;
          Update;
     end;
     PBILStart.Caption:= 'Perform PBIL';
     PBILStart.Refresh;
end;

{Since PBIL is inherently random in nature, the first result achieved is
not necessarily the best. Therefore, the process should by repeated
multiple times and the best results then used. This search simply
implements multiple PBIL searches keeping track of the best results.}
procedure TPBILMain.MultiSearchPBILClick(Sender: TObject);
var currentiter, i : integer;
   overbestfreq : double;
   multirecord : textfile;
   filestring : string;
begin
     LoadFreqsClick(Sender);
     overbestfreq := -1;
     for currentiter := 1 to NumIterations.Value do
     begin

          CurIterCaption.Caption := inttostr(currentiter);
          PBILStartClick(Sender);
          if besteverfit > overbestfreq then
          begin
               overbestfreq := besteverfit;
               OverFreq1.Caption := Freq1.Caption;
               OverFreq2.Caption := Freq2.Caption;
               OverFreq3.Caption := Freq3.Caption;
               OverFreq4.Caption := Freq4.Caption;
               OverFreq5.Caption := Freq5.Caption;
               OverFreq6.Caption := Freq6.Caption;
               OverFreq7.Caption := Freq7.Caption;
               OverFreq8.Caption := Freq8.Caption;
```

```
            OverBestFreqFit.Caption := BestFreqFit.Caption;
        end;

        resreeord[1,currentiter] := besteverfit;
        for i := 2 to 9 do
          resrecord[i,currentiter] := besteverreal[i-1];


        filestring := 'c:\multi'+inttostr(eurrentiter)+'.txt';
        AssignFile(multirecord,filestring);
        ReWrite(multirecord);
        WriteLn(multirecord,'Best fit: '+floattostr(resrecord[1,currentiter]));
        WriteLn(multirecord,'Frequeneies for best fit:');
        for i := 2 to 9 do
            WriteLn(multirecord,floattostr(resrecord[i,currentiter]));
        CloseFile(multirecord);

    end;

    if SaveMultiRecord.Execute then
    begin
      AssignFile(multirecord,SaveMultiRecord.FileName);
      ReWrite(multirecord);
      for currentiter := 1 to NumIterations.Value do
      begin
        WriteLn(multirecord,'Best fit: +floattostr(resrecord[1,currentiter]));
        WriteLn(multirecord,'Frequencies for best fit:');
        for i := 2 to 9 do
            WriteLn(multirecord,floattostr(resrecord[i,currentiter]));
        WriteLn(multirecord,' ');
      end;
      CloseFile(multirecord);
    end;
end;

end.
```

APPENDIX C

CIRCUIT DIAGRAMS FOR AN 8-ELECTRODE FDM EIT SYSTEM

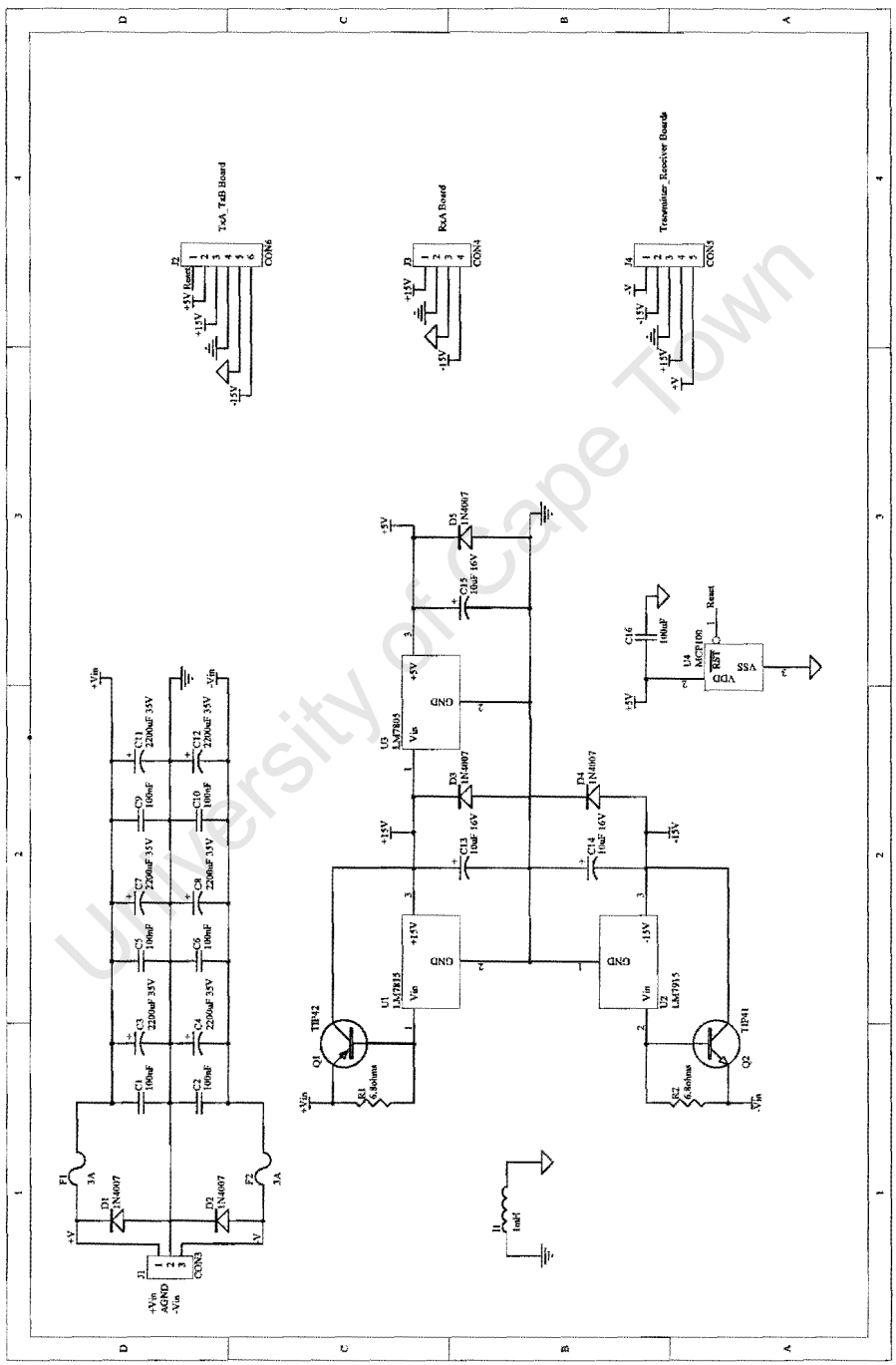

CIRCUIT DIAGRAM OF THE POWER SUPPLY UNIT USED BY THE FREQUENCY GENERATION AND SYNCHRONOUS DETECTION BOARDS

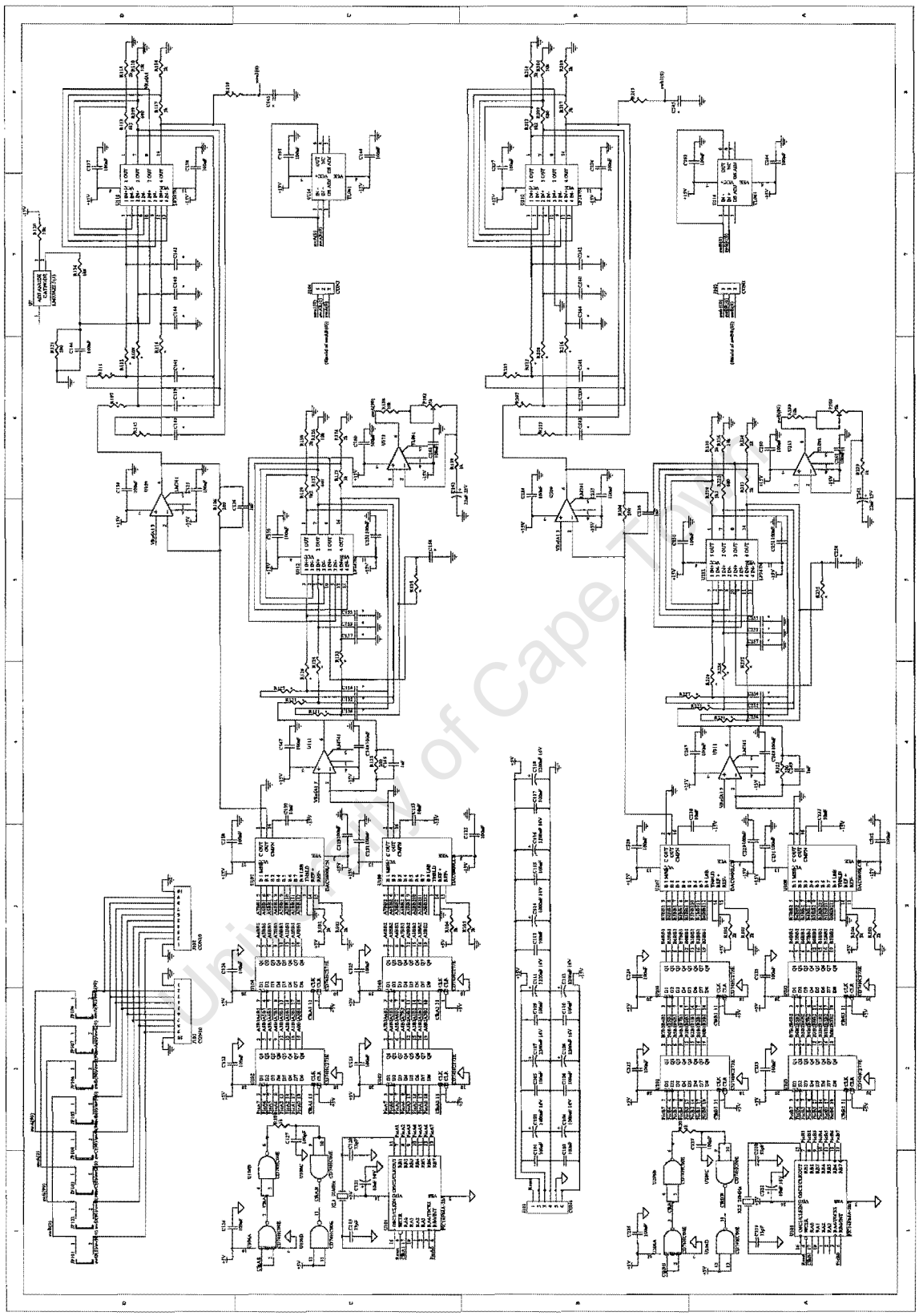

CIRCUIT DIAGRAM OF THE FREQUENCY GENERATION BOARDS

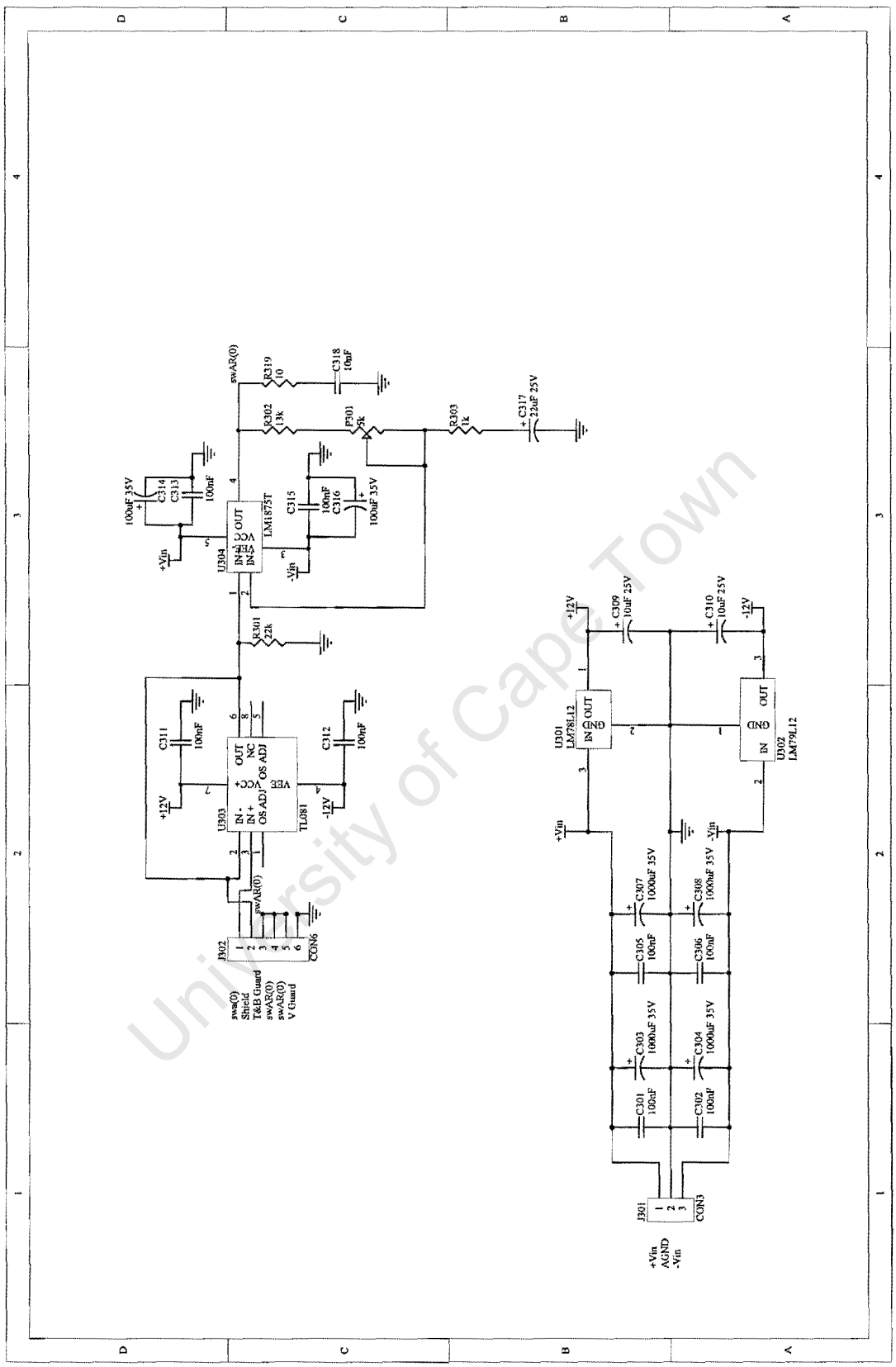

CIRCUIT DIAGRAM OF THE TRANSMITTER BOARDS

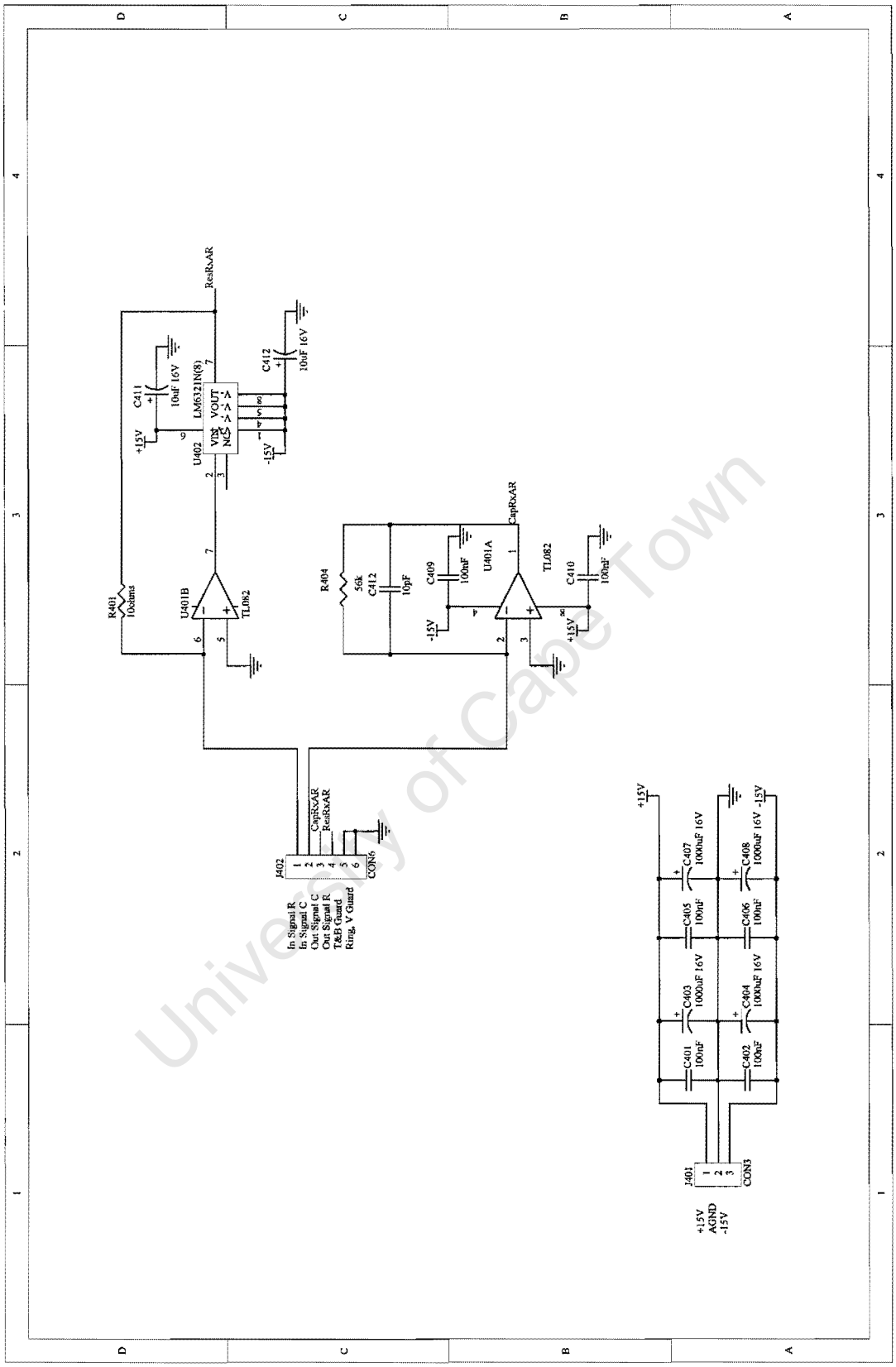

CIRCUIT DIAGRAM OF THE RECEIVER BOARDS

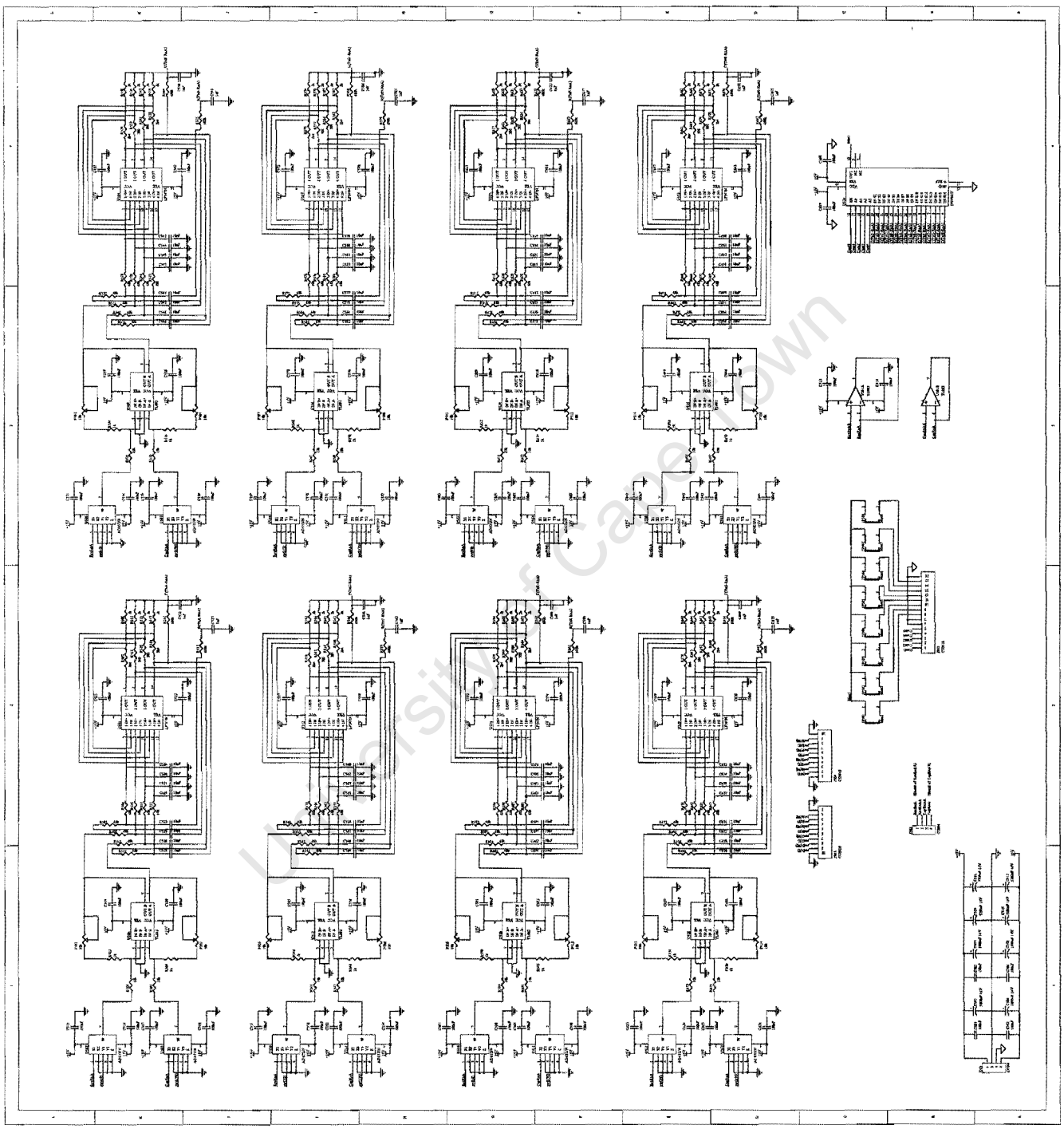

CIRCUIT DIAGRAM OF THE SYNCHRONOUS DETECTION BOARDS

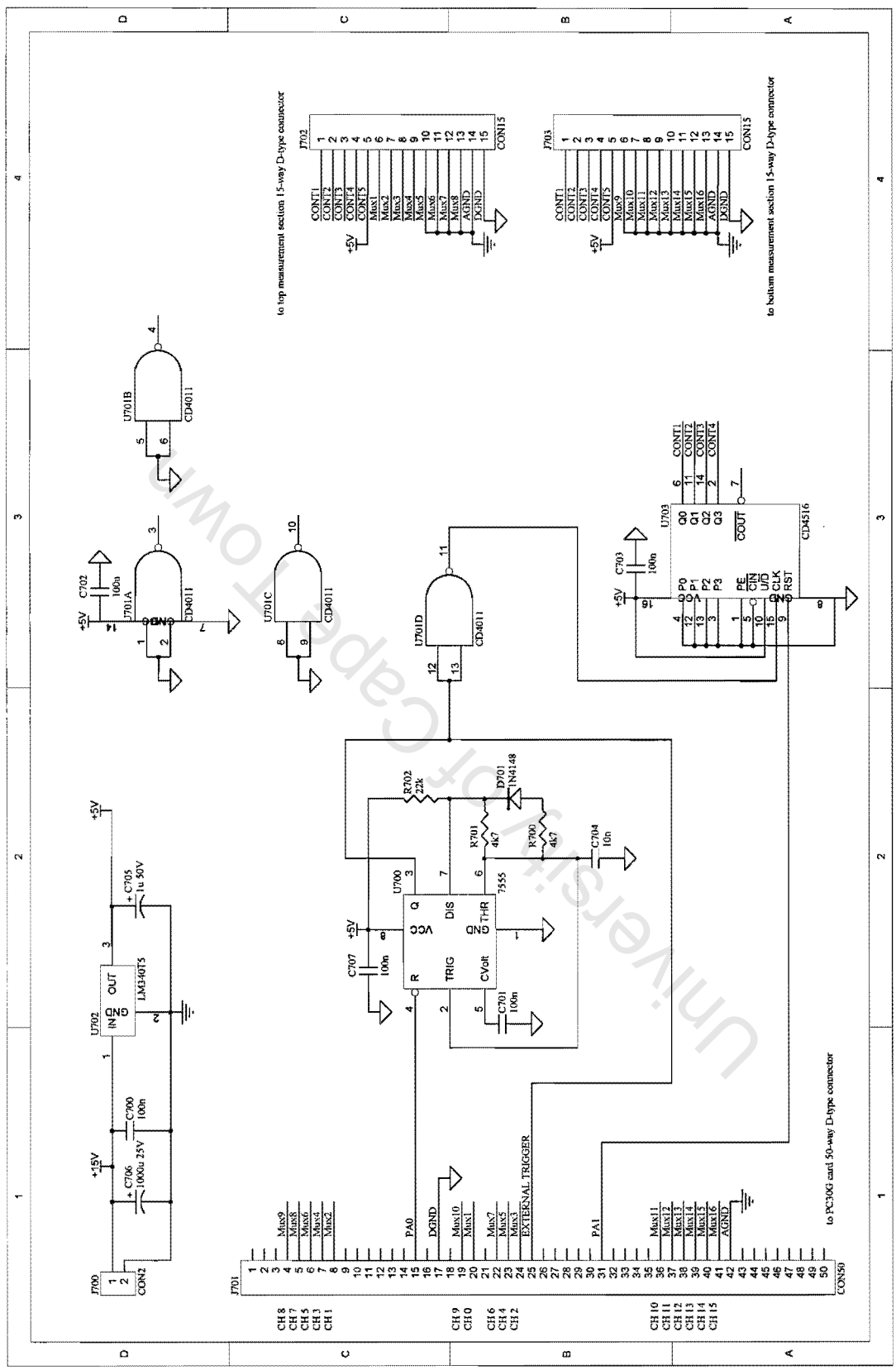

CIRCUIT DIAGRAM OF THE SAMPLE CONTROLLER BOARD